

## AN ABSTRACT OF THE THESIS OF

Beate Leitner for the degree of Doctor of Philosophy in Geophysics presented on June 14, 1999. Title: Plate Boundary Deformation of the Pacific Plate: Two Case Studies.

1) Crustal Structure of the Northwestern Vizcaino Block and Gorda Escarpment, Offshore Northern California, and Implications for Postsubduction Deformation of a Paleoacretionary Margin. 2) A Focused Look at the Alpine Fault, New Zealand: Seismicity, Focal Mechanisms and Stress Observations.

*Redacted for Privacy*

Abstract approved: \_\_\_\_\_

John L. Nábelek

Two examples of Pacific rim plate boundary deformation are presented. In the first part of the thesis crustal models are derived for the northwestern part of the Vizcaino block in California using marine seismic and gravity data collected by the Mendocino Triple Junction Seismic Experiment. A northwest-southeast trending kink in the Moho is imaged and interpreted to have formed under compression by reactivation of preexisting thrust faults in the paleoacretionary prism at the seaward margin of the Vizcaino block. The study suggests that the deformation resulted from mainly north-south compression between the Pacific-Juan de Fuca plates across the Mendocino transform fault and predates late Pliocene Pacific-North America plate convergence.

In the second part, 195 earthquakes recorded during the duration of the Southern Alps Passive Seismic Experiment (SAPSE) are analysed. Precise earthquake locations and focal mechanisms provide unprecedented detail of the seismotectonics in the central South Island. The short term (6 month) SAPSE seismicity is compared with long term (8 years) seismicity recorded by the New Zealand National Seismic network and the Lake Pukaki network. The seismicity rate of the Alpine fault is low, but comparable to locked sections of the San Andreas fault, with large earthquakes expected. Changes of the depth of the seismogenic zone, generally uniform at about 10-12 km, occur only localised over distances smaller than 30 km, suggesting that thermal perturbations must be of similar

scale. This implies that the thermal effects of the uplift of the Southern Alps do not change the seismogenic depth significantly and are not in accordance with most of the present thermal models. Both the Hope and Porters Pass fault zones are seismically active and deformation is accommodated near the fault zones and in the adjacent crust. North of Mt Cook, a triangular shaped region along the Alpine fault is characterised by absence of earthquakes. We interpret this as the result of the plate boundary shift from the Alpine fault to the Hope and Porters Pass fault zones. The study region shows distributed deformation in a 60-100 km wide zone on NNE-SSW trending thrust faults and strike-slip mechanisms on transfer faults.

©Copyright by Beate Leitner

June 14, 1999

All Rights Reserved

Plate Boundary Deformation of the Pacific Plate. Two Case Studies. 1) Crustal Structure of the Northwestern Vizcaino Block and Gorda Escarpment, Offshore Northern California, and Implications for Postsubduction Deformation of a Paleoaccretionary Margin. 2) A Focused Look at the Alpine Fault, New Zealand: Seismicity, Focal Mechanisms and Stress Observations.

by

Beate Leitner

A THESIS

submitted to

Oregon State University

in partial fulfillment of  
the requirements for the  
degree of

Doctor of Philosophy

Completed June 14, 1999  
Commencement June 2000

Doctor of Philosophy thesis of Beate Leitner presented on June 14, 1999

APPROVED:

*Redacted for Privacy*

---

Major Professor, representing Geophysics

*Redacted for Privacy*

---

Dean of the College of Oceanic and Atmospheric Sciences

*Redacted for Privacy*

---

Dean of Graduate School

I understand that my thesis will become part of the permanent collection of Oregon State University libraries. My signature below authorizes release of my thesis to any reader upon request.

*Redacted for Privacy*

---

Beate Leitner, Author

## Acknowledgements

I would like to thank my committee members: John Chen, Donna Eberhart-Phillips, Barbara Gartner, John Nábelek, Anne Tréhu, David Rogge, and Robert Yeats. All of you provided support well beyond the normal job description.

My supervisor, John Nábelek, introduced me to seismology both in the field and at the research desk. Thanks, for your support throughout this study. Our crisis coffee talks were much appreciated. Anne Tréhu supervised the research on the Vizcaino block, introducing me to the world of large-scale seismic experiments and the integration of geophysical and geological observations, which are essential parts of this thesis. Donna Eberhart-Phillips gave me the opportunity to come to Dunedin and work on the Alpine fault project. Thank you for such a great working environment and your support throughout this thesis. Robert Yeats gave me important feedback and support, during the last 6 month.

The research for this thesis was carried out at Oregon State University, Corvallis, Oregon; at Otago University, Dunedin, New Zealand; at the Institute of Geological and Nuclear Sciences in Dunedin and in Lower Hutt, New Zealand; and at GeoSphere, Lower Hutt, New Zealand. I would like to express my thanks to all faculty members, research scientists, technicians, computer support people, fellow students and colleagues, who helped in numerous ways.

I gained tremendously from discussions with Grant Caldwell, Richard Norris, Peter Koons, Chris Pearson, Kelvin Berryman, John Beavan, Russell Robinson, and Terry Webb.

This work would not have been possible without unique data. Thanks to all organizers and participants of the Mendocino Triple Junction Seismic Experiment, the Southern Alps Passive Seismic Experiment and the South Island Geophysical Transect.

I would like to thank Glenn Thrasher and Mac Beggs at GeoSphere. Your support, trust and humour is very much appreciated. What a great place to work.

Thanks to the Institute of Geological and Nuclear Sciences and Dick Beetham in particular, who graciously gave me access to their facilities during the last crucial months, while I was employed with GeoSphere.

Thanks to Jochen Braunmiller for all scientific advice, a great working relationship, and the great friend you are. Thanks to Leonore Hoke and Weerachai Siripunvaraporn, who helped with reviews and printing in almost real time.

Last but not least, thanks to my parents and my sister. Without your love, interest, and support across the continents, it would not have been worthwhile. Thanks to Vince, who was always there for me.

## CONTRIBUTION OF AUTHORS

Chapter 2 is published in the Journal of Geophysical Research, V 103, pages 23795-23812, October 1998 under the title:

Crustal structure of the northwestern Vizcaino block and Gorda Escarpment, offshore northern California, and implications for postsubduction deformation of a paleoaccretionary margin.

Authors: B. Leitner, A. M. Tréhu and N. J. Godfrey

Dr. Anne Tréhu was my supervisor for this research project. She provided guidance with the data processing, interpretation and the writing of the manuscript. Seismic reflection line 4 and 5 were processed and interpreted by her. Dr. Nicola Godfrey contributed with discussions and reviewed the interpretation. A companion paper, published by Godfrey et al. (in the same issue of the Journal of Geophysical Research) is closely related in content and the interpretation in both papers benefited from our discussions.

Chapter 3 is in preparation for the Journal of Geophysical Research under the title:

A focused look at the Alpine fault, New Zealand: Seismicity, focal mechanisms and stress observations.

Authors: B. Leitner, D. Eberhart-Phillips, H. Anderson and J. N. Nábelek

Dr. Donna Eberhart-Phillips supervised this research project. She provided guidance with the data processing, interpretation and writing of the manuscript. Dr. Helen Anderson shared with me her deep insight of New Zealand tectonics and reviewed the manuscript. Dr. John Nabelek assisted in the interpretation and discussion of the theoretical part of the manuscript.

The manuscript is submitted for internal review at the Institute of Geological and Nuclear Sciences, Wellington, New Zealand. The submission of the manuscript is expected in a few months, following incorporation of comments by the reviewers, co-authors and thesis committee members.

## TABLE OF CONTENTS

1. Introduction .....	1
2. Crustal Structure of the Northwestern Vizcaino Block and Gorda Escarpment, Offshore Northern California, and Implications for Postsubduction Deformation of a Paleoaccretionary Margin .....	6
2.1 Abstract .....	7
2.2 Introduction .....	7
2.2.1 Vizcaino Block.....	8
2.2.2 Gorda Escarpment.....	10
2.2.3 Plate Tectonic History.....	11
2.3 Data Acquisition, Processing, and Modeling .....	15
2.3.1 Modeling the Large-Aperture Seismic Data .....	16
2.3.1.1 Line 3S .....	22
2.3.1.2 Line 4.....	25
2.3.1.3 Line 5.....	26
2.3.1.4 Velocities.....	30
2.3.2 Modeling the Gravity Data.....	32
2.3.2.1 Line 3S .....	33
2.3.2.2 Line 4.....	37
2.3.2.3 Line 5.....	38
2.4 Discussion .....	39
2.5 Tectonic Implications.....	41
2.6 Conclusions .....	47
2.7 Acknowledgments.....	48
2.8 References .....	49
3. A Focused Look at the Alpine Fault, New Zealand: Seismicity, Focal Mechanisms and Stress Observations .....	58
3.1 Abstract .....	59
3.2 Introduction.....	60
3.3 Overview .....	62
3.3.1 Seismicity.....	64
3.3.2 Alpine Fault.....	64
3.3.3 Transition Zones.....	67

## TABLE OF CONTENTS (continued)

3.4	Data and Earthquake Locations.....	68
3.4.1	Southern Alps Passive Seismic Experiment.....	68
3.4.2	Joint Hypocenter Determination .....	72
3.4.3	New Zealand National Seismic Network.....	79
3.4.4	Lake Pukaki Network.....	79
3.4.5	1997 Mt Cook Earthquake and Aftershocks .....	80
3.5	Focal Mechanisms.....	80
3.5.1	Amplitude Ratio and First Motion Method.....	81
3.5.2	Moment Tensor Inversion.....	93
3.5.3	Technique Comparison .....	93
3.6	Stress Observations .....	97
3.7	Results .....	99
3.7.1	Depth of Seismicity .....	101
3.7.2	Alpine Fault.....	106
3.7.3	Northern Transition Zone.....	109
3.7.4	From Mt Cook to Haast.....	114
3.7.5	Southern Transition Zone.....	117
3.8	Conclusions .....	119
3.9	Acknowledgements.....	121
3.10	References .....	122
4.	Summary .....	133
	Bibliography.....	136

## LIST OF FIGURES

<u>Figure</u>	<u>Page</u>
1.1 Pacific plate boundary with study regions indicated by grey boxes .....	2
1.2 Mendocino Triple Junction Seismic Experiment overview (Figure from [Trehu et al., 1995]) .....	3
1.3 Southern Alps Passive Seismic Experiment (SAPSE) and South Island Geophysical Transect experiment (SIGHT) overviews (Figure courtesy of David Okaya) .....	5
2.1 Map of the Mendocino triple junction region.. .....	9
2.2 Cartoon of the plate boundary evolution (adapted from Bohannon and Parsons [1995] at 30, 20, 10, and 0 Ma) highlighting the important phases in Vizcaino block history since the Oligocene .....	12
2.3 Processed record sections (see text for details) of ocean bottom instruments recording (a) and (b) line 3S, (c) line 4 and (d)-(i) line 5 MCS air gun shots .....	17
2.4 (a) Velocity model of line 3S. (b) Velocity model of Line 4. (c) Velocity model of line 5. ....	21
2.5 Bathymetry from ship data and top of basement from depth migrated MCS data .....	23
2.6 Blow up of MCS data for lines 4 and 5 at their intersection and DSDP Site 173 .....	28
2.7 Amplitude plots of (top) synthetic and (bottom) observed record sections of OBH 17 .....	29
2.8 Velocity-depth profiles of lines 3S, 4, and 5 of the velocity models shown in Figure 2.4 (a)-(c) .....	31
2.9 Observed (circles) and calculated (solid line) free air and Bouguer anomalies and density models for lines 3S, 4, and 5 .....	34
2.10 (a) Three-dimensional cartoon of the crustal structure in the northwestern part of the Vizcaino block. (b) Sketch of line 3S, which is a cross section of the Vizcaino block. ....	42

## LIST OF FIGURES (continued)

<u>Figure</u>	<u>Page</u>
2.11 Migrated seismic reflection profile collected by the USGS in 1977 [McCulloch, 1987a; Godfrey, 1997, Godfrey et al., 1998] .....	44
2.12 Factors influencing the likelihood of compressional deformation in the Vizcaino block.....	46
3.1 Earthquakes and focal mechanisms derived from body waveform modeling plotted in lower hemisphere projection [Harvard CMT catalogue; Anderson et al., 1993; Doser and Webb, submitted] for $M_w >$ 5.4 in the South Island .....	61
3.2 Overview of geology and geologic site locations. ....	63
3.3 South Island seismicity maps .....	69
3.4 P-velocity models discussed in text .....	74
3.5 a) Histograms showing magnitude and depth of earthquakes recorded with SAPSE. b) Location of SAPSE earthquakes relocated by Joint Hypocenter inversion using P and S wave picks of the short period and broadband stations .....	75
3.6 a) Synthetic (dashed line) and observed (solid line) seismograms for 960124.174426 .....	82
3.7 Example earthquake 960328.164027 shows robustness of method by similarity of the calculated focal mechanisms using a) all available observations b) 3/4 c) 3/3 first motion/amplitude ratio observations.....	85
3.8 Examples of first motion and amplitude ratio method for earthquakes with A-D quality (quality criteria are summarised in Table 3.4) .....	87
3.9 Stereonet projection of P and T axes .....	91
3.10 a) Focal mechanisms derived by moment tensor inversion are shown in the top row. Mechanisms from first motion and amplitude ratio method are given in the second row, where available. b) and c) Observed and synthetic seismograms for mechanism derived by waveform inversion. b) Cass main shock. c) Largest Cass aftershock .....	94

## LIST OF FIGURES (continued)

Figure	Page
3.11 Stereonet projection of the 80% confidence regions for the three principal stress axes of the best fitting stress tensor which fits A and C quality focal mechanisms .....	98
3.12 Maps showing quality locations of SAPSE (black), Pukaki (grey) and NZNSN (open circles) earthquakes.....	100
3.13 Seismicity along 3 cross sections shown in Figure 3.5 projected orthogonal to the Alpine fault .....	102
3.14 Alpine fault seismicity and focal mechanisms .....	107
3.15 Seismicity with $M_b > 2.5$ in Southern California between 1990-1997 .....	108
3.16 Seismicity and focal mechanisms from the Hope fault to Mt Cook. ....	110
3.17 Seismicity and focal mechanisms from Mt Cook to Jackson Bay .....	115
3.18 Seismicity and focal mechanisms south of Jackson Bay .....	118
3.19 a) Sketch map summarising the different tectonic regions in the study area .....	120

## LIST OF TABLES

<u>Table</u>	<u>Page</u>
2.1 RMS Values of Velocity Models Based on <i>Pg</i> Arrivals (Figure 2.4a-2.4c) and Gravity Models (Figure 2.9) .....	22
2.2 Velocity-Density Conversion References .....	33
2.3 Geometry of Lines and Apparent and True Dips of Moho Kink .....	39
3.1 Station Corrections .....	73
3.2 Location Error of Refraction Shots .....	78
3.3 Depth Quality of SAPSE and Mt Cook Earthquakes.....	78
3.4 Quality of Focal Mechanisms .....	86
3.5 Focal Mechanisms of A and C Quality Events.....	89

## **Dedication**

*I dedicate this thesis to Vince, Sarah and Brian.  
Your unwavering support and love gave me the  
strength to finish this degree.*

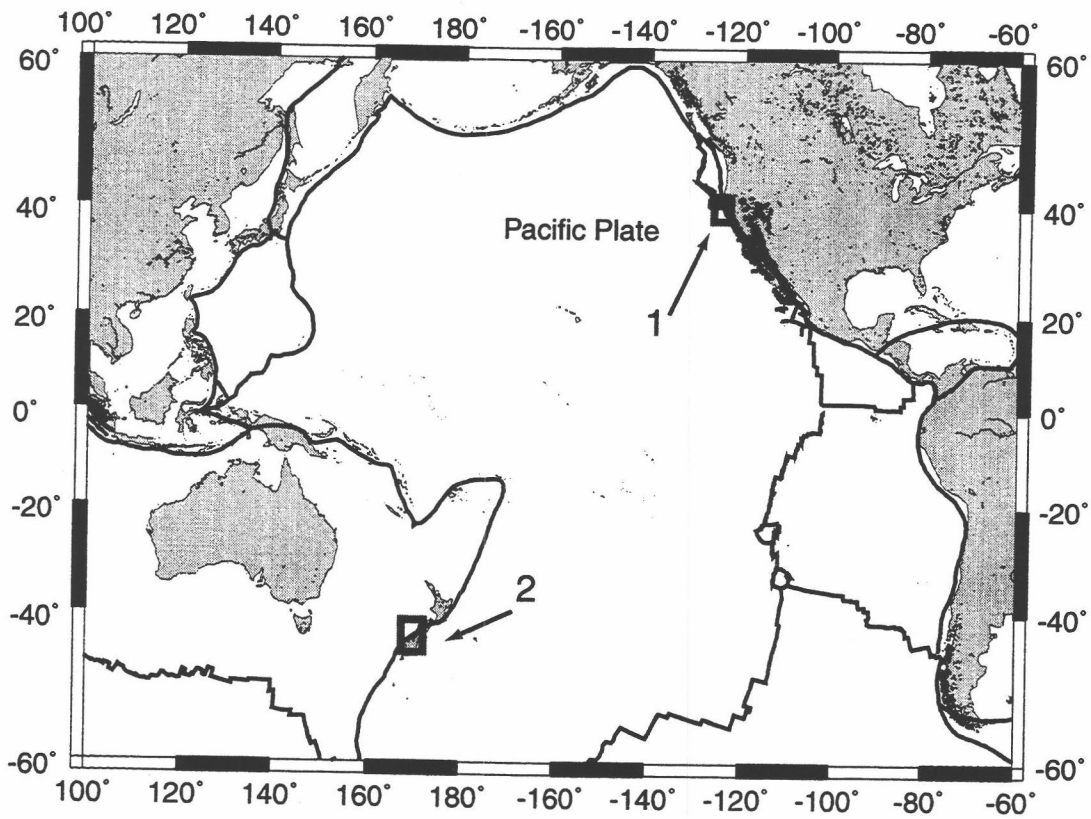
## **Plate Boundary Deformation of the Pacific Plate. Two Case Studies:**

- 1) Crustal Structure of the Northwestern Vizcaino Block and Gorda Escarpment, Offshore Northern California, and Implications for Postsubduction Deformation of a Paleoaccretionary Margin.**
- 2) A Focused Look at the Alpine Fault, New Zealand: Seismicity, Focal Mechanisms and Stress Observations.**

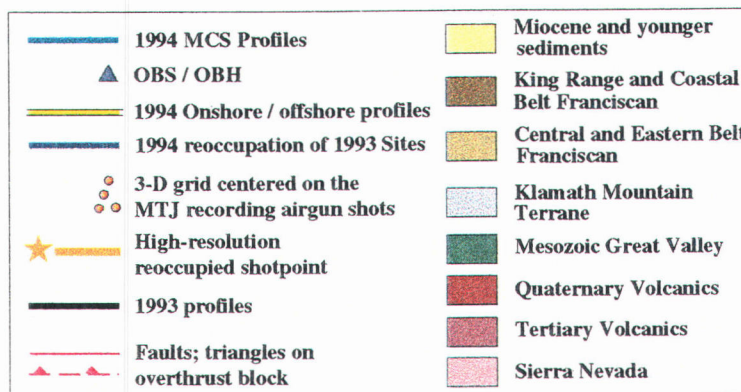
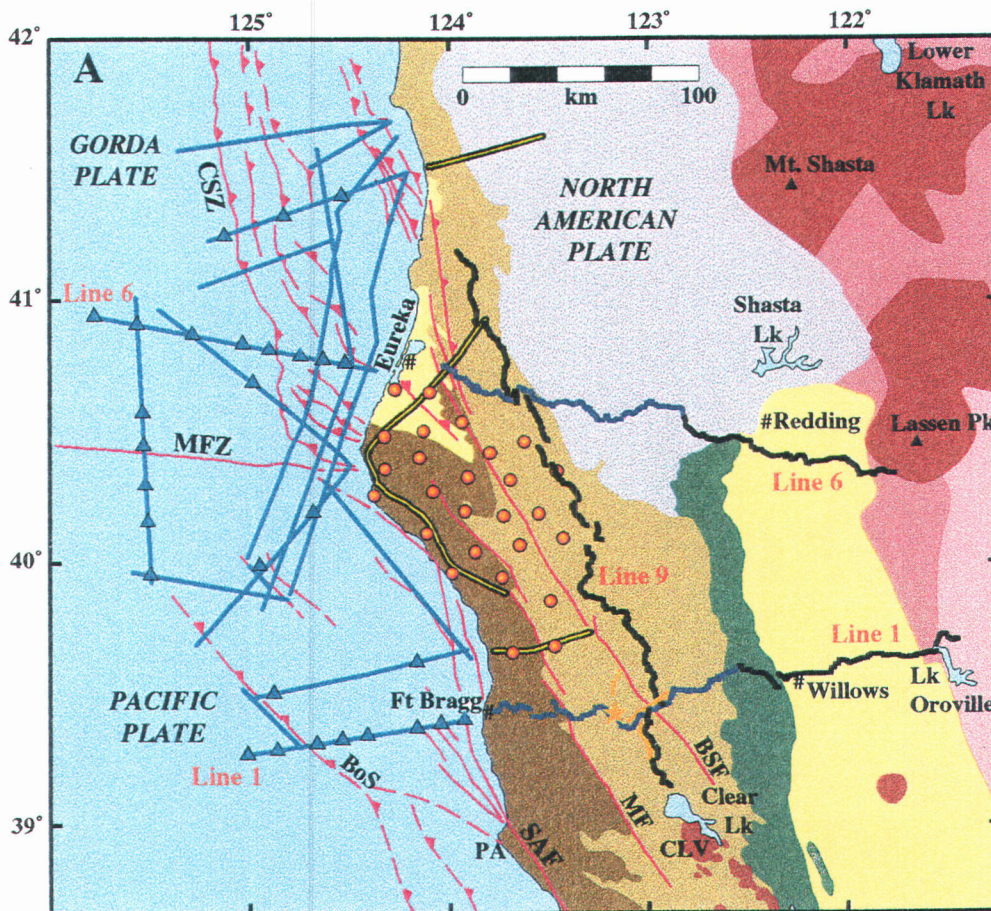
### **1. Introduction**

Plate tectonics has revolutionised earth sciences and has been extremely successful in explaining the large-scale motion of the lithosphere. In the ocean basins plate tectonics is relatively simple and applies down to a 10 km scale. However, within continents and between continental and oceanic plates, boundaries behave as broad deformation zones, which can vary greatly from place to place. This thesis presents two examples of plate deformation zones at the Pacific plate boundary: one in New Zealand and the second one in northern California (Figure 1.1). In both cases data were utilised from large scale multi-institutional geophysical experiments involving several disciplines: e.g. magnetotellurics, GPS, active seismic data acquisition onshore and offshore, recording of local, regional and teleseismic earthquakes, and potential field data. The experiments provide new unique high quality data covering an area several 100 km wide across the active plate boundary in the South Island of New Zealand and the Mendocino Triple Junction region in California. It will be shown in this thesis that the synergy of multi-geophysical data provides a powerful tool to improve our understanding of deformation in plate boundary zones.

In the second chapter, large-aperture seismic and gravity data collected over the northwestern part of the Vizcaino block during the 1993/1994 Mendocino Triple Junction Seismic Experiment (Figure 1.2) are presented. The crustal structure of the Vizcaino block and the Gorda Escarpment at its northern boundary preserves the plate boundary processes since the Oligocene. The geological evolution of this plate margin is not well



**Figure 1.1** Pacific plate boundary with study regions indicated by grey boxes. Arrow 1 points to the Vizcaino block, southwest of the Mendocino Triple Junction in northern California. Arrow 2 marks the Alpine fault region in the South Island of New Zealand.



**Figure 1.2** Mendocino Triple Junction Seismic Experiment overview (Figure from [Trehu et al., 1995]). Locations of the 1993 and 1994 seismic experiments overlay on a simplified geologic map of northern California. MTF, Mendocino transform fault; CSZ, Cascadia subduction zone; SAF, San Andreas fault; MF, Maacama fault; PA, Point Arena; BoS, Base of slope; BSF, Bartlett Spring fault; CLV, Clear Lake volcanics.

northwestern margin of the Vizcaino block, and provide new evidence for significant deformation of the paleoaccretionary margin in this region. Similar deformation has been observed on transects across the paleoaccretionary margin in central and southern California [e.g. *Tréhu*, 1991; *Meltzer and Levander*, 1991; *Howie et al.*, 1993; *Holbrook et al.*, 1996; *Miller et al.*, 1992, 1996]. In this study both the Moho dip and trend are imaged by the data. It will be shown that reconstruction of the relative plate motion at the Vizcaino block and the tectonic evolution of the Vizcaino block can be used to deduce the cause of deformation and constrain it in time.

In the third chapter new earthquake locations and focal mechanisms are presented along the Alpine fault which forms the Pacific-Australian plate boundary in the central South Island of New Zealand. The plate boundary was the target of the South Island Geophysical Transect (SIGHT) and the Southern Alps Passive Seismic Experiment (SAPSE) in 1995/1996 (Figure 1.3). Earthquakes in the central South Island are, with few exceptions, smaller than magnitude 4, and consequently their depth and mechanisms are not resolved routinely by the present permanent national seismic network.

Two hundred earthquakes in a 150 x 400 km wide zone along the Alpine fault are analysed with the goal to get focal mechanisms and to put limits on the seismogenic depth. To validate our observations over an 8-year period, we compare the 6 months of SAPSE seismicity with the seismicity recorded by the New Zealand National Seismic network and the Lake Pukaki network. A first-motion and amplitude technique is utilized to derive the focal mechanisms for the  $M_L$  2-4.2 earthquakes. The study shows the usefulness of this method applied to a regional network of short period and broadband seismic stations. Moment tensors of the 5 largest earthquakes provide an independent mean of comparison of the first motion and amplitude ratio method. The study investigates the possibility, that geologically observed changes in the character along the Alpine fault are reflected in the seismicity. New results from ongoing studies of the SIGHT and SAPSE experiments are integrated in the interpretation, and correlation between changes of the seismogenic depth and thermal models are explored.

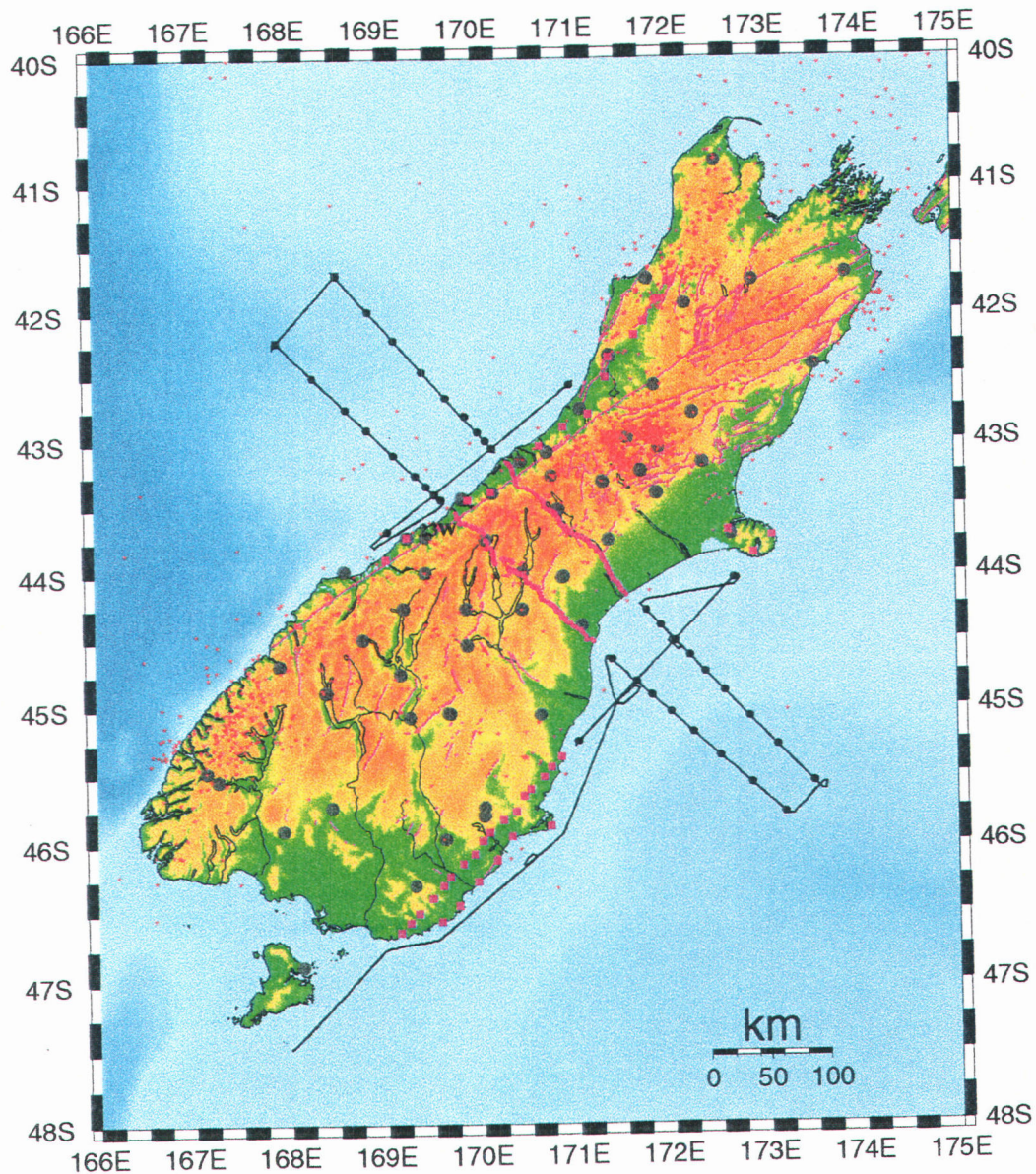


**Figure 1.3** Southern Alps Passive Seismic Experiment (SAPSE) and South Island Geophysical Transect experiment (SIGHT) overviews (Figure courtesy of David Okaya). Pink dots are earthquakes recorded during the SAPSE deployment. Black lines mark the R/V *Ewing* ship tracks along which seismic and potential field data were collected; black dots are locations of ocean bottom instruments; purple diamonds mark onshore seismic recorders, grey circles are SAPSE seismometers and New Zealand National Seismic Network (NZNSN) station locations.

## **Chapter 2**

# **Crustal Structure of the Northwestern Vizcaino Block and Gorda Escarpment, Offshore Northern California, and Implications for Postsubduction Deformation of a Paleoaccretionary Margin**

Beate Leitner, Anne M. Tréhu, and Nicola J. Godfrey

Published in the *Journal of Geophysical Research*,  
Volume 103, pages 23795-23812, October 1998.

Copyright by the American Geophysical Union

## 2.1 Abstract

The Vizcaino block is an anomalously shallow region of the western U.S. continental margin located southwest of the Mendocino triple junction. It originated as part of the accretionary prism of the North America plate and was transferred to the Pacific plate in the Miocene as the Pacific-North America plate boundary migrated ~130 km eastward, forming the Gorda Escarpment at its northern boundary. We present hybrid crustal models for the northwestern part of the Vizcaino block derived from marine seismic and gravity data. The velocity and density structure of the northwestern Vizcaino block are compatible with paleoaccretionary complex material similar to San Simeon/Patton terrane overlying oceanic crust or a mafic layer. The most significant result of our modeling is an abrupt increase in Moho dip from  $\sim 5^\circ$  to  $\sim 20\text{-}30^\circ$  beneath the western edge of the Oconostota ridge along the northwestern margin of the Vizcaino block. This Moho dip is steeper than observed anywhere along the Cascadia subduction zone, indicating postsubduction deformation. We suggest that the paleotrench was deformed by compression, which reactivated preexisting thrust faults in the upper crust and thickened the crust within this apparent weak zone. At least part of the deformation predates late Pliocene Pacific-North America plate convergence and may result mainly from north-south compression between the Pacific-Juan de Fuca plates across the Mendocino transform fault. North-south compression continues today and may dynamically support the uplifted northern margin of the Vizcaino block, although the primary locus of deformation shifted to the relatively weak Gorda plate sometime prior to 3 Ma.

## 2.2 Introduction

The active Cascadia margin north of the Mendocino triple junction has a shallow-dipping Moho and base to the accretionary prism. In contrast, results from several transects across the paleoaccretionary prism making up the California margin show steeply dipping lower crust and Moho segments [e.g., *Tréhu, 1991; Meltzer and*

*Levander, 1991; Howie et al., 1993; Holbrook et al., 1996; Miller et al., 1992, 1996*], indicating postsubduction deformation. Marine seismic and gravity data from the Mendocino Triple Junction Seismic Experiment [*Tréhu et al., 1995*] allow further investigation of the tectonic process causing this deformation in the northwestern Vizcaino block. The hybrid velocity and density crustal models derived in this study image the lower crustal deformation along strike and address the question of why deformation is focused along the seaward part of the accretionary wedge. Resolution of the Moho dip and its trend is better in this study than in many of the earlier studies because of the range of strikes along which this feature has been sampled.

### 2.2.1 Vizcaino Block

The Vizcaino block forms an unusually wide, triangular-shaped, shallow region on the continental margin (Figure 2.1a) offshore northern California whose tectonic history and basement structure has been the subject of considerable speculation. It is bounded by the Mendocino transform fault to the north, the San Andreas fault zone to the east, and the Navarro discontinuity to the southwest, and it approximately follows the continental slope and change of trend in magnetic anomalies at its western margin (for a summary, see *McCulloch [1987a, b, 1989]*). Its western margin is characterized by a buried basement high, known as the Oconostota ridge, which is approximately parallel to topographic contours.

Vizcaino block basement is juxtaposed against the onshore King Range terrane (middle Miocene [*McLaughlin et al., 1982*]) and coastal Franciscan belt (Cretaceous to Eocene accretionary complex [*Blake and Jones, 1981*]) along the San Andreas fault, and abuts against the Salinian terrane (Cretaceous plutonic terrane [*Mattinson, 1978*]) and Franciscan or San Simeon terranes (Cretaceous-Oligocene accretionary complex [*McLaughlin et al., 1994*]) at the Navarro discontinuity. The Vizcaino block is presently part of the Pacific plate and is migrating northward relative to the North America plate along the present-day San Andreas transform fault system [*Atwater, 1970, 1989*]. At present, much of the transform motion in the San Andreas fault system appears to be

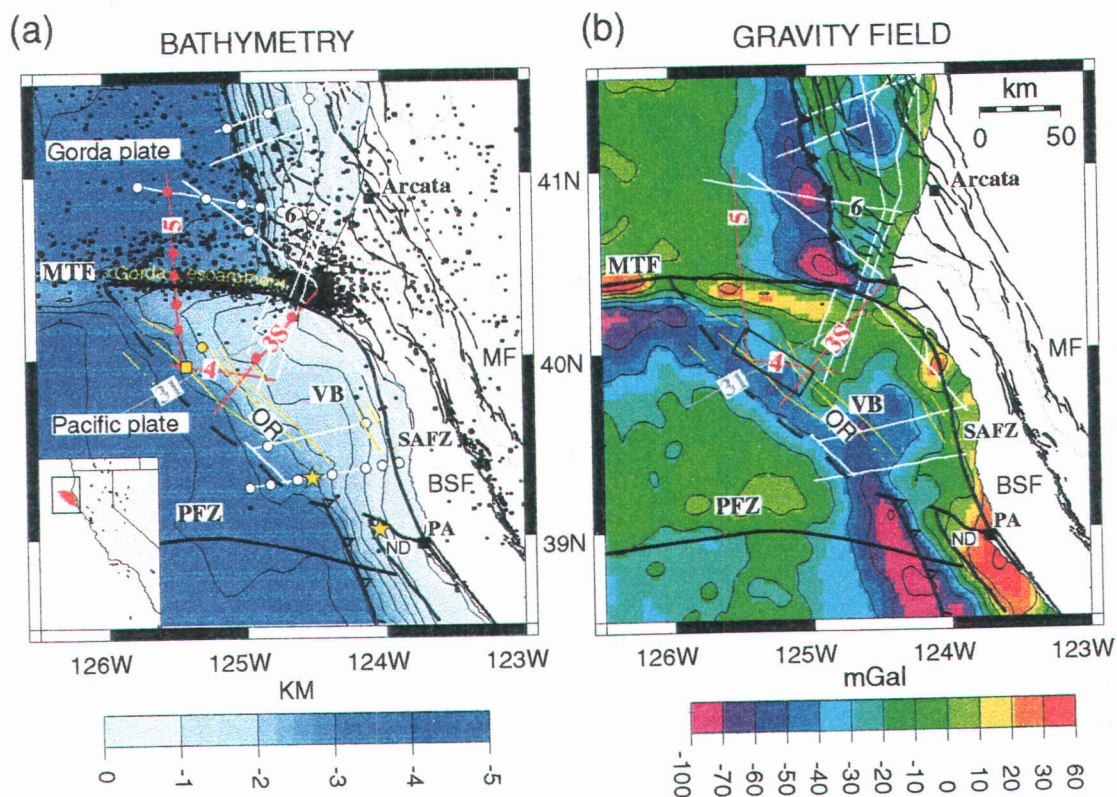


**Figure 2.1** Map of the Mendocino triple junction region. Red (data presented in this paper) and white lines mark the R/V *Ewing* ship tracks along which seismic and gravity data were collected during the 1994 Mendocino triple junction seismic experiment. Gray line is a seismic reflection line of 1977 vintage shown in Figure 2.11. SAFZ, San Andreas fault zone; MTF, Mendocino transform fault; ND, Navarro discontinuity; PFZ, Pioneer fracture zone; VB, Vizcaino block, OR, Oconostota ridge, PA, Point Arena; BSF, Bartlett Spring fault; MF, Maacama fault. Faults to the east of the SAFZ and the Cascadia trench are from *Castillo and Ellsworth* [1993]. The western margin of the Vizcaino block is shown as a dashed line [after *McCulloch*, 1987a]. Open triangles mark the approximate location of the paleotrench south of the ND; solid triangles mark the position of the Cascadia trench. (a) Bathymetry (National Geophysical Data Center CD-Rom release 1.0, Geophysics of North America). Basement sample locations shown as yellow stars [McCulloch, 1987a] and basement ridges after *Godfrey* [1997] shown as yellow lines. DSDP Site 173 is marked by a yellow square, ODP Site 1022 is marked by a yellow circle. Solid dots are earthquakes with  $M > 3$  (northern California earthquake data center, 1970-1996). The inset locates the map region and Vizcaino block in California. (b) Global marine gravity data [Sandwell and Smith, 1997]. The solid box marks the region of the Moho kink discussed in this study.

taken up in the Coast Range east of the San Andreas fault along the Maacama and Bartlett Springs faults [Castillo and Ellsworth, 1993]. Seismicity in the offshore region, an indication of present-day tectonic deformation, is concentrated along the Mendocino transform fault and within a triangular region in the southeast corner of the Gorda plate adjacent to the Vizcaino block (Figure 2.1a). The Vizcaino block therefore appears to represent a rigid part of the Pacific plate. The Vizcaino block basement is believed to have formed in an accretionary prism. This conclusion is supported by lithologic basement samples from four localities in the western part of the Vizcaino block [McCulloch, 1987a; McLaughlin et al., 1994], a deep reflection interpreted to be the top of the subducted plate beneath the western margin [McCulloch, 1987a; Henstock et al., 1996, 1997; Godfrey, 1997], and multiple basement ridges throughout the western part of the Vizcaino block (Figure 2.1a; yellow lines) that have been interpreted as blind thrusts similar to those observed in accretionary complexes [Godfrey, 1997]. The satellite-derived free-air gravity anomaly data over the western margin show a gravity low (Figure 2.1b), typical for a subduction zone trench. This low, however, is less prominent than the observed gravity low along the Cascadia trench north of the Mendocino transform fault or the paleotrench south of the Vizcaino block in central California (Figure 2.1b). One objective of this project was to determine whether this is entirely due to differences in the accretionary prism geometry or if structural deviations from a typical paleotrench boundary are required in the underlying crust.

### 2.2.2 Gorda Escarpment

The morphology of the Mendocino transform fault changes at about 126°W. East of 126°W, the Mendocino transform fault is at the base of the Gorda Escarpment, a steep, north facing escarpment where the Vizcaino block is elevated up to 1.5 km above the Gorda plate seafloor (2.1a). This topographic step is opposite to what is predicted from the age difference between the Pacific (old) and Gorda (young) plates. West of 126°W, the seafloor of the Pacific plate is, on average, 1 km deeper than the adjacent Gorda seafloor, consistent with the age and density contrast between the two plates

[*Engebretson et al.*, 1985], and the transform is immediately north of a 5-15 km-wide ridge known as the Mendocino Ridge. Basalt cobbles dredged from the ridge and submersible observations indicate that the Mendocino Ridge was once above sea level [*Krause et al.*, 1964; *Duncan et al.*, 1994] and has since subsided. Ages of rock samples from the Mendocino Ridge west of 126°W range between 7 and 22 Ma, indicating that Gorda plate material was obducted onto the Pacific plate [*Duncan et al.*, 1994]. In contrast, the only dated sample from the Gorda Escarpment is Cretaceous [*Fisk et al.*, 1993]. These observations suggest that the evolution of the Gorda Escarpment is connected with the development of the Vizcaino block and may have an uplift and subsidence history that is different from that of the Mendocino Ridge west of 126°W. A second objective of this study was to determine whether the basement ridge along the Gorda Escarpment is gravitationally compensated by a crustal root.

### 2.2.3 Plate Tectonic History

The present-day structure of the Vizcaino block and Gorda Escarpment is the integrated result of plate boundary processes since the Oligocene. Numerous workers have reconstructed the plate boundary evolution in time and space based on offshore magnetic anomalies, fault offsets in California, and other geologic constraints [e.g., *Atwater*, 1970; *Graham and Dickinson*, 1978; *Engebretson et al.*, 1985; *Atwater and Severinghaus*, 1989; *Drake et al.*, 1989; *Sedlock and Hamilton*, 1991; *Fernandez and Hey*, 1991; *Lonsdale*, 1991; *Wilson*, 1993; *McLaughlin et al.*, 1994; *Nicholson et al.*, 1994; *Bohannon and Parsons*, 1995; *McCrorry et al.*, 1995]. The four important stages of plate boundary evolution in the history of the Vizcaino block are subduction, extension, transfer to the Pacific plate, and Pacific plate motion (Figure 2.2). The Farallon plate subducted beneath the North American continent until about 27-25 Ma (Figure 2.2a), when the Pacific-Farallon ridge reached the trench. Spreading and subduction of the ridge beneath the accretionary prism may have continued until 20-16 Ma [*Severinghaus and Atwater*, 1990; *Bohannon and Parsons*, 1995; *McLaughlin et al.*, 1996] (Figure 2.2b).

**Figure 2.2** Cartoon of the plate boundary evolution (adapted from *Bohannon and Parsons [1995]* at 30, 20, 10, and 0 Ma) highlighting the important phases in Vizcaino block history since the Oligocene. Locations of the cross sections are indicated by the solid line on the map view. Ages in Ma are upper and lower bounds for the given processes. MFZ, Mendocino fracture zone; PFZ, Pioneer fracture zone; JDFF, Juan de Fuca plate; NAP, North America plate; PP, Pacific plate. (a) Subduction phase; subduction of the Farallon plate beneath the North-American continent until the ridge collided with the trench about 27-25 Ma. The Vizcaino block is part of the accretionary wedge at the western margin of the North America plate north of the Mendocino fracture zone. (b) Extensional phase; following ridge collision about 27-25 Ma, the Pacific plate and the Pacific-Farallon ridge likely continued subduction and ridge spreading [*McLaughlin et al., 1996*] until about 20-16 Ma. The ridge possibly continued to move eastward and could have caused relative high heat flow, magmatic underplating and the formation of the Point Arena basin in its wake. (c) Transfer phase; offshore transform initiated 20-18 Ma possibly on a detachment surface beneath the accretionary wedge (dashed line in cross section) and connected the Mendocino fracture zone with the northward extension of the Pacific-Farallon ridge system to the south by initiating the San Andreas-Pilarcitos fault system [after *McLaughlin et al., 1996*]. The detachment region beneath the accretionary wedge marked in gray grows eastward with time. At about 12-10 Ma, the San Andreas fault is the master fault and the Vizcaino block is now part of the Pacific plate. (d) Pacific plate phase; the Vizcaino block moves with the Pacific plate along the San Andreas fault system. About 3.5 Ma, near Point Arena, the San Andreas fault changed its trend to a more northerly direction responding to a clockwise change of Pacific-North America relative plate motion.

### Vizcaino Block History

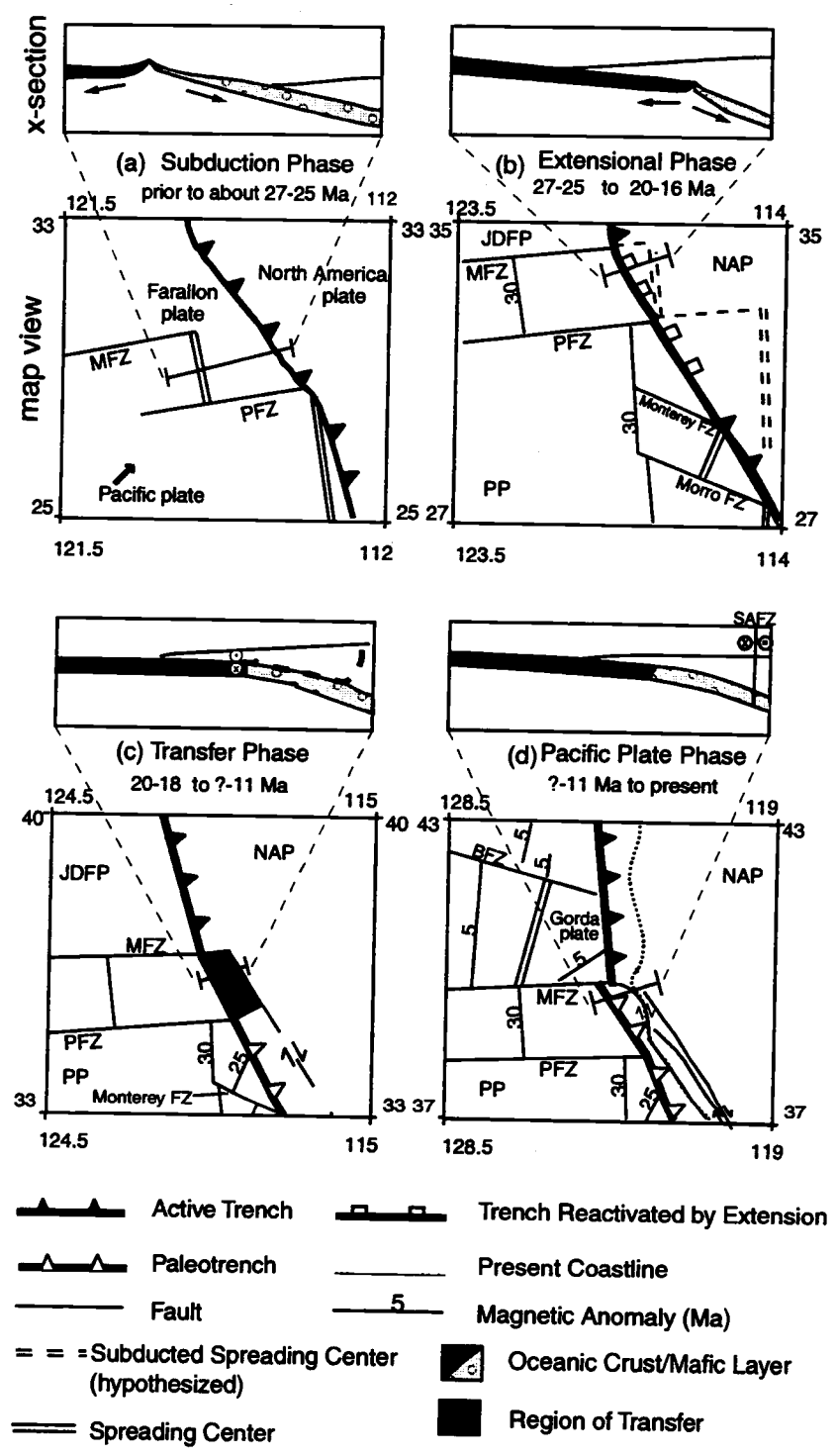


Figure 2.2

Between 20 and 12 Ma, there was a change from oblique subduction to transform motion on the San Andreas fault system. The evolution of transform motion in time and space during this period is poorly constrained. *McCrorry et al.* [1995] speculated that between 20 and 16 Ma, transform motion initiated along a subsurface detachment at the slab-accretionary complex interface and that this low-angle transform boundary propagated eastward and upward (Figure 2.2c) forming the Gorda Escarpment in its wake. It remains uncertain if the eastward migration of the plate boundary was a continuous process through time or occurred in distinct steps [e.g., *Dickinson and Snyder*, 1979; *McCulloch*, 1987b; *Drake et al.*, 1989; *Griscom and Jachens*, 1989; *Sedlock and Hamilton*, 1991; *Smith et al.*, 1993; *McLaughlin et al.*, 1994, 1996].

About 12-10 Ma the primary locus of transform motion apparently shifted to the Pilarcitos/San Andreas fault system [*McLaughlin et al.*, 1996]. *Griscom and Jachens* [1989] propose that an offshore transform fault west of the present-day San Andreas fault zone was active until about 5 Ma. The apparent absence of strike-slip type deformation in seismic reflection data from the 6-10 Ma Delgada fan [*Drake et al.*, 1989] and underlying late Miocene sediments that overlie the Vizcaino block [*Hoskins and Griffiths*, 1971; *McCulloch*, 1987a; *Drake et al.*, 1989; *Godfrey*, 1997; *Ondrus*, 1997], however, has been used to argue against this interpretation. *Godfrey et al.* [1998] present evidence that the present-day Mendocino triple junction may have been at its present location relative to the Mendocino transform fault significantly earlier than 11 Ma.

The uplift of both the Mendocino Ridge and Gorda Escarpment may have been a result of compressional stresses across the transform caused by changes in relative plate motion, [e.g., *Riddihough*, 1984; *Wilson et al.*, 1984; *Duncan and Clague*, 1985; *Cox and Engebretson*, 1985; *Wilson*, 1988, 1993] and by differences in thermal and viscoelastic properties of the adjacent oceanic lithospheres [*Bonatti*, 1978]. The latter are partly controlled by the age difference between the plates, which changed polarity at about 12 Ma [*Engebretson et al.*, 1985]. North-south compression increased considerably after the inception of the Blanco transform (about 6 Ma) and continues to the present-day [*Wilson*, 1993]. Part or all of the present-day north-south compression is absorbed by the Gorda plate, where the curvature of magnetic patterns and shorter magnetic anomalies on

the east side versus the west side of the Gorda ridge indicate internal deformation [e.g. *Silver, 1971; Riddihough, 1980; Wilson, 1986, 1989; Stoddard, 1987; Denlinger, 1992*]. The difference in morphology of the Gorda Escarpment from that of the Mendocino Ridge west of  $126^\circ$ , both exposed to the same tectonic forces, suggests that it is strongly affected by the crustal structure of the Vizcaino block.

### 2.3 Data Acquisition, Processing, and Modeling

We present large-aperture seismic and gravity data collected over the northwestern part of the Vizcaino block, the Gorda Escarpment, and the Gorda plate during the 1994 phase of the Mendocino Triple Junction Seismic Experiment [*Tréhu et al., 1995*]. The R/V *Ewing* recorded multichannel seismic (MCS), potential field and bathymetric data along 14 profiles. Results from three of these profiles are presented in this study (Figure 2.1a). Four ocean bottom seismographs (OBS) and four ocean bottom hydrophones (OBH), deployed from the R/V *Wecoma*, recorded shots from the R/V *Ewing* tuned air gun array along lines 3S, 4, and 5 (Figure 2.1a, marked in red). We construct hybrid crustal models using the MCS data to constrain sediment thickness along the profiles, the large-aperture data to constrain the P wave velocity and thickness of the crust where permitted by the ray coverage, and gravity data to extend constraints on the geometry of the lower crust and Moho. Details of MCS processing and interpretation are discussed elsewhere [*Godfrey, 1997; Godfrey et al., 1998; T. Henstock, personal communication, 1997; A. S. Meltzer, personal communication, 1997*]. Magnetic field data are not discussed in this paper since the magnetic field variation over the Vizcaino block is small along lines 3S, 4, and 5 south of the Mendocino transform fault. The magnetic field of the Gorda Escarpment where crossed by line 5 is well modeled assuming an average susceptibility of oceanic crust. Directly north of the Mendocino Ridge, magnetic lineations from the Gorda crust trend obliquely to line 5, and two-dimensional (2-D) modeling is not valid.

### 2.3.1 Modeling the Large-Aperture Seismic Data

Large-aperture data coverage is best on line 5, along which 6 instruments recorded data (Figure 2.1a). At the intersection of lines 4 and 5, OBH 24 recorded air gun shots from both lines. On line 3S only 2 of 3 instruments deployed recorded data. Air gun shots on lines 3S, 4, and the middle section of line 5 were shot at 20 s intervals (about 50 m) to optimize the MCS data. This resulted in bands of previous shot noise (PSN) that interfere with crustal arrivals in the OBH/OBS record sections (Figure 2.3). Shot spacing at both ends of line 5 was 50 s (about 130 m), which is preferable for large-aperture data when seafloor depths are greater than 1000 m [Christeson *et al.*, 1996]. Although the signal-to-noise ratio on the OBHs was generally higher than on the OBSs, the OBHs were more strongly affected by PSN (Figure 2.3). PSN could be reduced, but not eliminated, by applying an F-k filter to the data after shifting the data to align traces along the previous shot instant [Christeson *et al.*, 1996].

After applying a time domain band-pass filter (4-30 Hz), gain amplification as a function of range and a  $6.5 \text{ kms}^{-1}$  reduction velocity to the OBHs/OBSs data, and after adding 2 adjacent traces when data were shot at a 20 s interval, travel-time picks were digitized from the record sections. A strong multiple (marked m, Figure 2.3) arriving with a time delay equal to the two-way travel time (twtt) through the water column above the instrument is apparent on all instruments. The amplitude of this arrival is often stronger than the first arrival, and it was used to verify and extend the range of first-arrival picks.

A starting model for 2-D inversion of travel times [Zelt and Smith, 1992] for line 3S utilized basement depths taken directly from a depth-migrated reflection profile [Henstock *et al.*, 1996]. The starting models for lines 4 and 5 were constructed from bathymetric and time-migrated MCS data. For lines 4 and 5, seafloor to basement travel times were converted to depth assuming a constant velocity gradient of  $0.7 \text{ kms}^{-1} \text{ km}^{-1}$  and a constant velocity of  $1.8 \text{ kms}^{-1}$  at the top of the sediment layer. This velocity gradient is an average of the velocity gradients obtained from 1-D travel time modeling of near-offset data for the line 5 instruments. In addition, the velocity model at the

**Figure 2.3** Processed record sections (see text for details) of ocean bottom instruments recording (a) and (b) line 3S, (c) line 4 and (d)-(i) line 5 MCS air gun shots. Shot spacing for line 5 instruments is indicated at top. PSN, previous shot noise; m, water multiple; EQ,  $M_w$  5.0 earthquake located offshore Petrolia, California [Braunmiller *et al.*, 1997]. Calculated arrival times for the velocity models in 2.4 (a)-(c) are shown by the solid lines. White arrows indicate possible lower crustal or Moho reflections not constrained by our line 3S velocity model. Possible mantle arrivals on OBS C3 and OBH 18 (marked '?') beneath the Gorda plate are obscured by PSN.

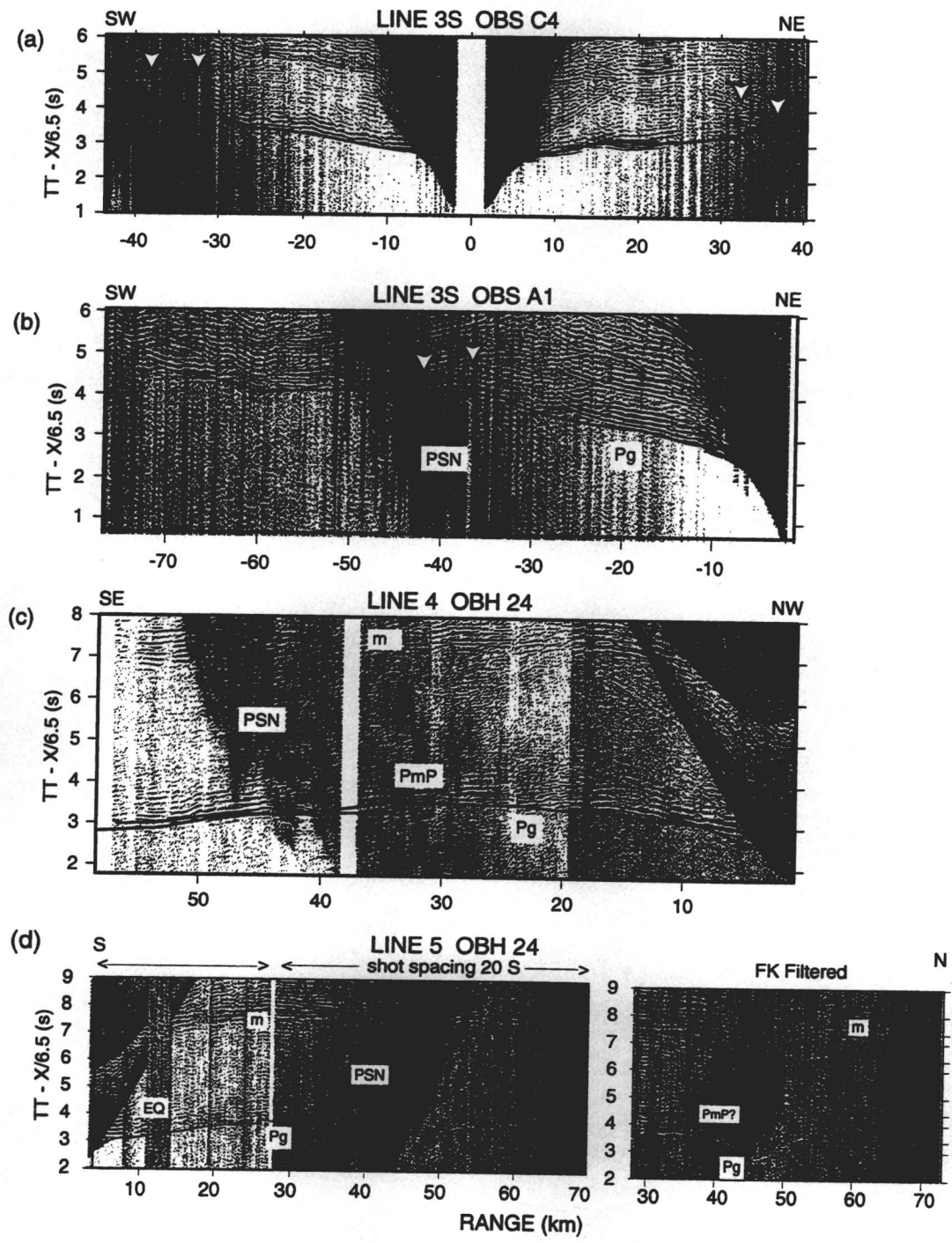


Figure 2.3 (continued)

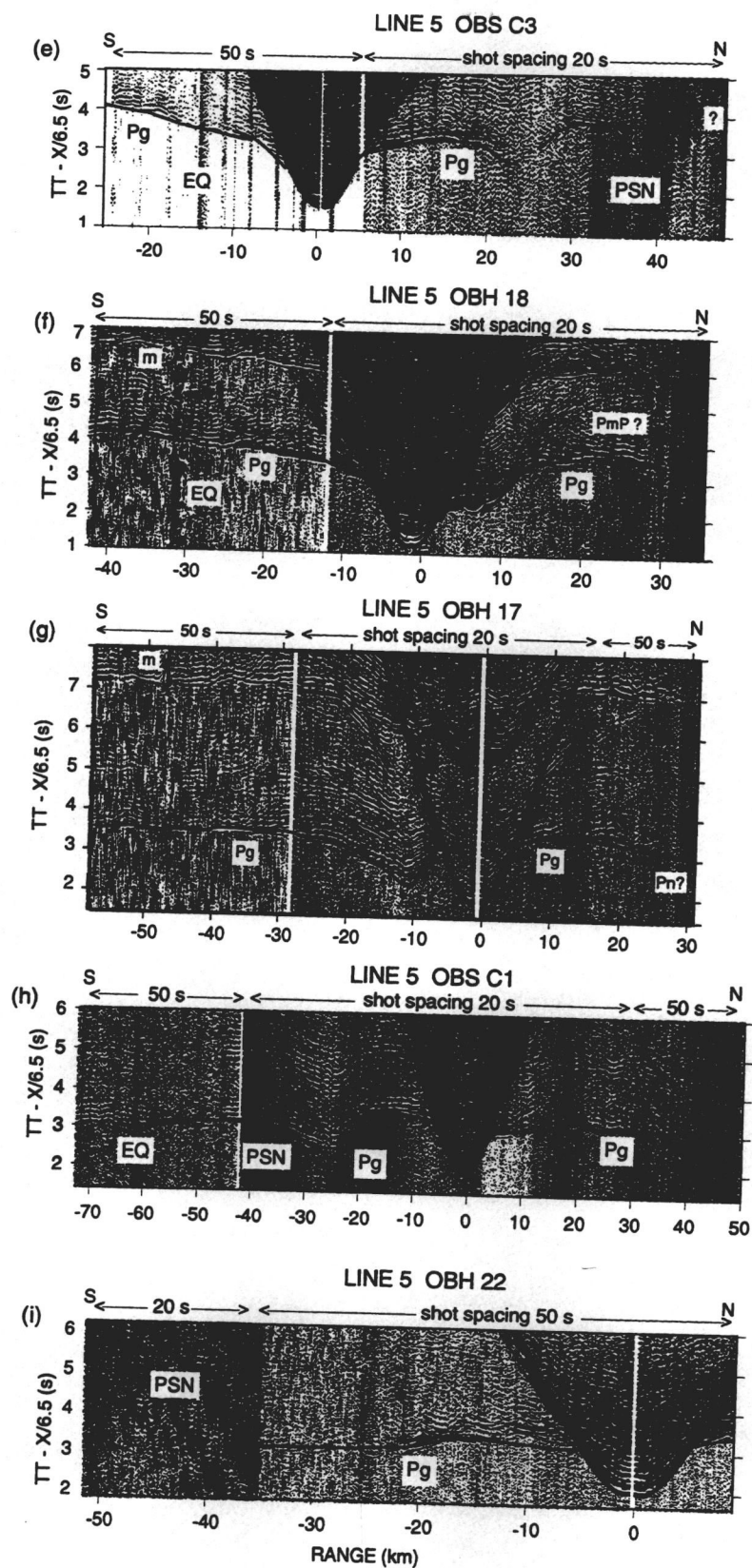
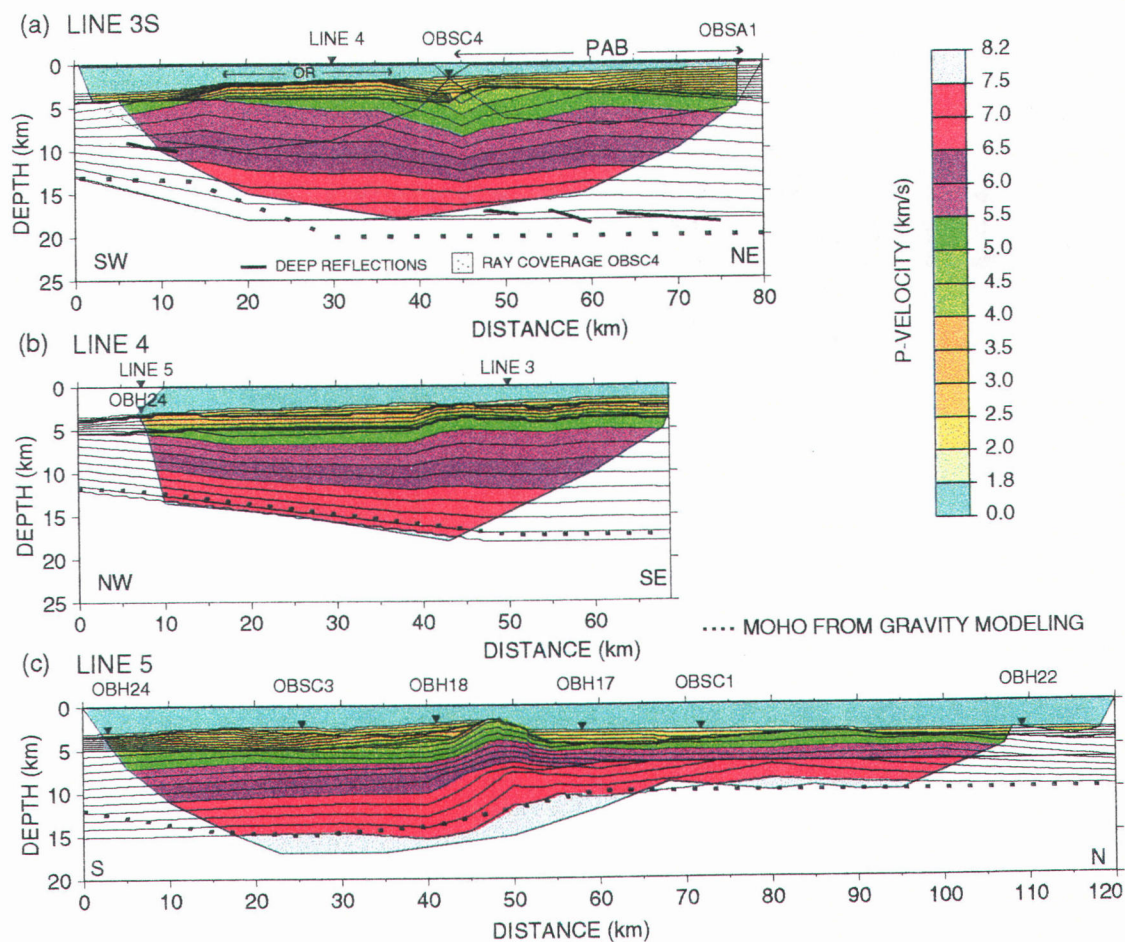


Figure 2.3 (continued)

northern end of line 5 was constrained in the inversion by velocity information from line 6 [Tréhu *et al.*, 1995].

Velocity models (Figure 2.4a-2.4c) were determined through an iterative forward/inverse modeling approach in which the initial inversion was performed for a three layer model (water, sediment, and crust) with velocities in the water and sediment layers fixed and velocity nodes to be determined by inversion placed at 20-km intervals along the top and bottom of the crustal layer. Because velocities between nodes increase linearly, velocity discontinuities and gradient changes in the crust were modeled by introducing additional layers, and the data were reinverted after the addition of each layer. The introduction of an upper crustal layer, allowing relatively low velocities and a high-velocity gradient in the upper basement of the Vizcaino block, reduced the travel time misfit for lines 3 and 5. Constraints on the velocity and thickness of the lower crust of the Gorda plate on line 5 were included as indicated by results from line 6, where reversed arrivals are observed from the lower crust and upper mantle [Tréhu *et al.*, 1995]. The modeled  $P_n$  and  $P_mP$  arrivals were not included in the inversion. The Moho depth of lines 3 and 4 were constrained by MCS and gravity data, where possible. The final models for lines 3S, 4, and 5 contain two, one, and three crustal layers, respectively. Final travel time misfits are summarized in Table 2.1.



**Figure 2.4** (a) Velocity model of line 3S. Note the absence of a continuous deep reflector between km 15 and 45. In this region basement topography is rough and energy gets scattered in the deeper section. (b) Velocity model of Line 4. Only one instrument recorded the data, and the model is constrained by the intersecting lines 3 and 5 velocity models. (c) Velocity model of line 5. The crust south of the Gorda Escarpment is twice as thick as to the north and increases abruptly beneath the Gorda Escarpment.

**Table 2.1** RMS Values of Velocity Models Based on *Pg* Arrivals (Figure 2.4a-2.4c) and Gravity Models (Figure 2.9).

Models	Line 3S	Line 4	Line5
		RMS	misfit
Velocity model	0.13	0.077	0.097
Gravity models			
Model I	2.83	3.5	3.1
Model II	1.78		2.87
Model III	1.94		

Misfits in s (velocity) and mGal (gravity).

### 2.3.1.1 Line 3S

Line 3S lies entirely within the Vizcaino block, extending diagonally from its western boundary at 125.2°W, 39.7°N to the coast near Cape Mendocino (Figure 2.1a). The profile is orthogonal to the Oconostota ridge and mapped basement ridges, providing a cross section of the Vizcaino block. Water depth decreases gradually from west (3 km) to east (0.5 km) along the profile, with a relatively rapid decrease between km 13 and 18 (the seaward edge of the Vizcaino block) (Figure 2.5a). The basement is shallowest between km 18 and 38, corresponding to the Oconostota ridge. A deep sedimentary basin (the Point Arena basin) overlies the eastern end of the profile, and sediments thicken west of the Oconostota ridge.

For this profile, we focus on using limited seismic data in conjunction with gravity data to explore a range of possible models for the Moho configuration beneath the

**Figure 2.5** Bathymetry from ship data and top of basement from depth migrated MCS data. (a) Line drawing of line 3S bathymetry and top of basement. (b) Migrated multichannel seismic data along line 4 show several basement ridges. Sediment horizons above the ridges are deformed and interrupted. (c) Line 4 bathymetry from ship measurements and top of basement from MCS data along line 4 constrain the velocity and gravity models. (d) Migrated near-trace data for line 5 shown with amplitudes corrected for spherical spreading. The top of the basement is well defined along the entire profile. The pattern of uplift and tilting of sediments on the Mendocino Ridge is similar to that reported by *Silver* [1971]. A more detailed discussion of stratigraphy based on MCS data is presented by *Godfrey et al.* [1998]. (e) Line 5 bathymetry from ship data and top of basement from time migrated MCS data (A. S. Meltzer, unpublished data, 1997). See text for details of the twtt to depth conversion. Bathymetry and sediment thickness changes between 0 and 2 km along the profile.

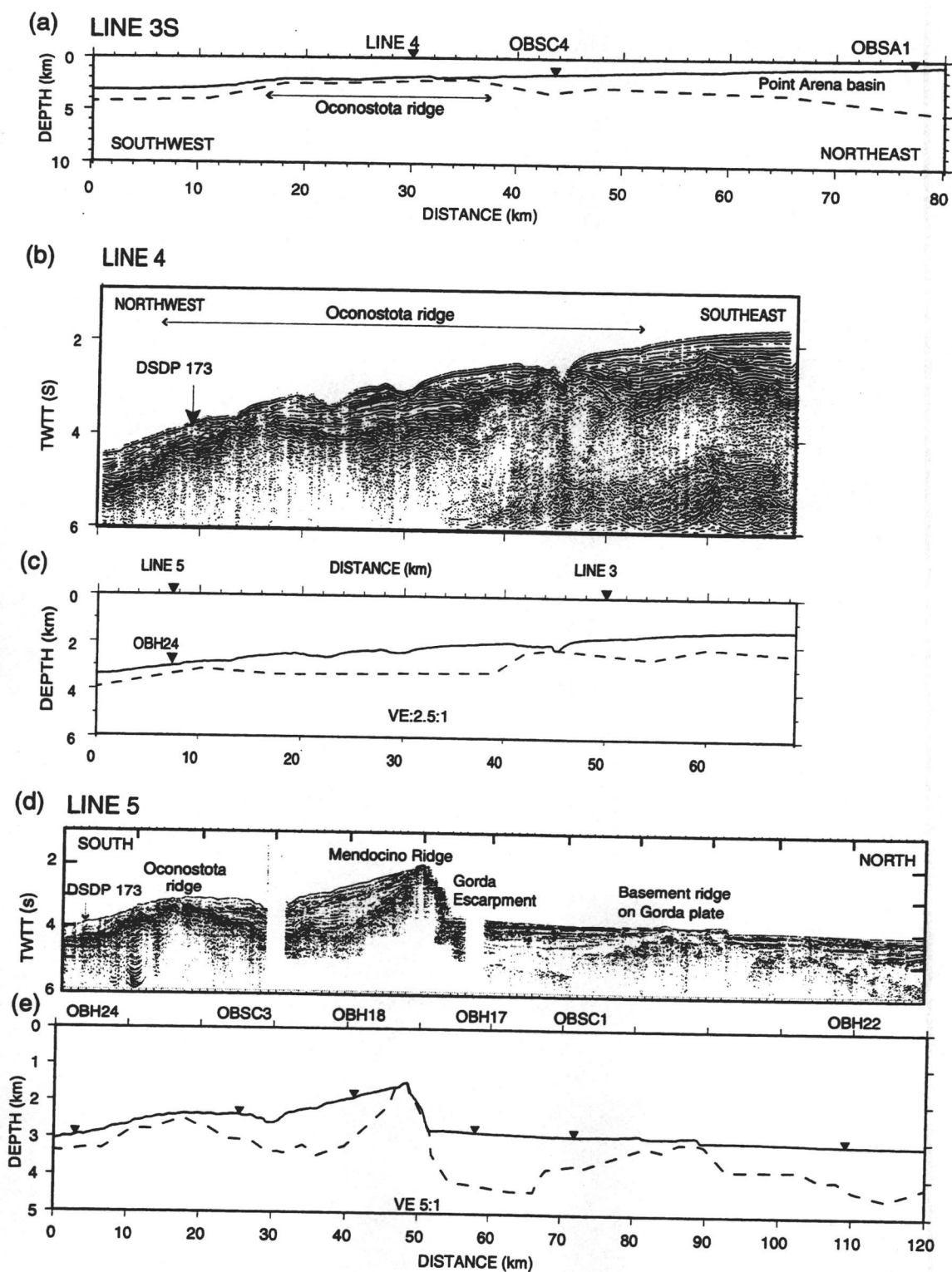


Figure 2.5

Oconostota ridge. This work complements efforts by *Henstock et al.* [1996] to determine structure beneath the triple junction region using MCS, OBS, and onshore-offshore data along two long profiles that cross approximately at the triple junction. We present a detailed analysis of a subset of the seismic data used for their model.

The large-aperture seismic data only sparsely sample the crust (Figure 2.4c). OBS C4 (Figure 2.3a) recorded diving waves ( $Pg$ ), sampling the upper 4-6 km of basement. A possible wide-angle reflection from the mid crust beneath the northeastern end of the line is marked by white arrows (Figure 2.3a) and is consistent with onshore-offshore observations, which require a thick layer of high-velocity lower crust at a depth of 9 km beneath the northeastern end of line 3S [*Henstock et al.*, 1996]. OBS A1 (Figure 2.3b) recorded  $Pg$  arrivals to an offset of 75 km, sampling the lower crust to a depth of 18 km. Ray coverage in the lower crust is limited to km 30 to 60 in the model. An arrival that may represent a reflection from either the top of the oceanic crust or from the Moho is marked by white arrows (Figure 2.3b), but due to our limited ray coverage in the lower crust, we cannot confidently model it.

A lateral velocity change in the basement rocks at about km 40 to 50 is required to model the near-range arrivals of OBS C4, which are only slightly asymmetric despite a pronounced decrease in sediment thickness west of the instrument (Figure 2.5a). In order to match these arrivals, a 2-km-thick layer with velocities of 3.5-4.5  $\text{kms}^{-1}$  was added just beneath the basement west of OBS C4 (Figure 2.4c). The thickness of and velocity in this layer agree with an intermediate velocity layer modeled at the southern end of line 5 and on the western part of line 4 (see discussion of these lines below). Beneath this depth, velocities increase approximately linearly with depth. A dip in the velocity contours beneath OBS C4 may be an artefact of uncertainties in the detailed configuration of the base of the overlying layer.

#### 2.3.1.2 Line 4

Line 4 extends for 70 km across the northwestern part of the Vizcaino block, crossing line 5 at km 7 and line 3 at km 50. Almost the entire line lies within the region of the

Oconostota ridge. MCS data define the top of the basement (Figures 2.5b and 2.5c), and no deeper reflections are observed. Basement topography is rough, and the general appearance of the data is similar to that of line 3S west of km 40 and line 5 south of the Gorda Escarpment.

OBH 24, located at the intersection of line 4 with line 5, recorded  $Pg$  and possible  $PmP$  and  $Pn$  arrivals to an offset of 60 km (Figure 2.3c). With only one receiver, we cannot resolve dipping structure and velocity gradients uniquely, although comparison with models for lines 3S and 5 help constrain the model. The resulting velocity model (Figure 2.4a) fits the data well (Table 2.1). Beneath the sediments, an intermediate velocity layer (3.5-4.5  $\text{kms}^{-1}$ ) of 2 km thickness overlies a layer with velocities of 5.0 to 7.4  $\text{kms}^{-1}$ .

### 2.3.1.3 Line 5

Four OBHs and two OBSs recorded air gun shots along the 120-km-long line 5 (Figure 2.4a). South of the Gorda Escarpment, the profile lies in the Vizcaino block. The seafloor rises from 3 km at the southern end of the profile to 1.5 km depth at the Mendocino Ridge. It then drops steeply to the 3-km-deep Gorda plate ocean floor. MCS data constrain the sediment thickness along the profile (Figure 2.5d). Sediment thickness increases towards the ridge from the south between km 20 to 40 and pinches out against the ridge crest. North of the ridge, the basement is offset by large faults that cut through the sediment and, in at least one case, offset the seafloor. No deep reflections are observed.

Rapid bathymetric and sediment thickness changes dominate the record sections (Figures 2.3d-2.3i). Modeled arrivals in the Vizcaino block are diving waves ( $Pg$ ) through the crust (OBH 24, OBS C3, OBH 18, OBH 17 south, and OBS C1 south). Shots from the southern end were recorded as far north as OBS C1 (offset of 76 km). F-k filtering enabled us to verify travel time picks between offsets of 28-45 km on OBH 24, where previous shot noise (PSN) obscured the arrivals on the unfiltered data (Figure 2.3d). The final velocity model south of the ridge (Figure 2.4c) has a 1.5-km-thick

intermediate velocity layer ( $2.5\text{--}4.5\text{ km s}^{-1}$ ) that is underlain by rocks in which velocity increases approximately linearly from 5 to  $7.4\text{ km s}^{-1}$ . The thick crust extends beneath the Mendocino Ridge to the Gorda Escarpment, north of which crustal thickness decreases abruptly.

The northern instruments were in an area of rough basement topography, leading to large diffractions, considerable scattering of seismic energy, and maximum observed offsets of about 30 km (OBH 22, OBS C1 north, OBH 17 north). Instruments north of the ridge are modeled by upper crustal velocities of  $5\text{--}6\text{ km s}^{-1}$  overlying a lower crust with velocities of  $6.5\text{--}7.6\text{ km s}^{-1}$ . The mid-crustal boundary is at 6.7 km depth, and the Moho is at 10 km depth (Figure 2.4c). Moho depth is constrained primarily by results from line 6 [Tréhu *et al.*, 1995] and is consistent with a possible *PmP* arrival on OBH 18 and *Pn* arrival on OBH 17 (Figures 2.3f and 2.3g).

We can compare our velocity model at the southern end of line 5 with results from the Deep Sea Drilling Project (DSDP) Site 173 at the intersection of lines 4 and 5 (Figure 2.6). The 0.4-km-thick sediment layer in our velocity model is in agreement with the drilling results [Kulm *et al.*, 1973]. The top of our intermediate velocity layer has velocities of  $2.5\text{--}4.5\text{ km s}^{-1}$  and coincides with the recovery of andesitic basalt at the bottom of the drill hole at 330 m. The velocities in this 1.5-km-thick layer are compatible with velocities of highly porous basalt or consolidated sediments and are observed in Franciscan/San Simeon terrane offshore central California [Howie *et al.*, 1993; Holbrook *et al.*, 1996]. The lateral extent of the andesitic basalt found in DSDP Site 173 remains uncertain.

We used elastic finite difference wave field modeling (code developed by Rodrigues and Mora [1992], adapted by Lendl [1996], summary by Lendl *et al.* [1997]), to verify the model along line 5. For this calculation, the velocity model was gridded at a 50-m spacing, and an explosive point source with a maximum frequency of 10 Hz was put at each instrument location. The wave field was recorded at 50-m intervals on the surface (i.e., the opposite of the actual experiment geometry). The synthetic record section for instrument OBH 17 shows a close match to the data (Figures 2.7 and 2.3g). The travel time advance resulting from propagation through the ridge matches the data satisfactorily, and the relative amplitudes of direct waves, multiples, shear and converted waves are

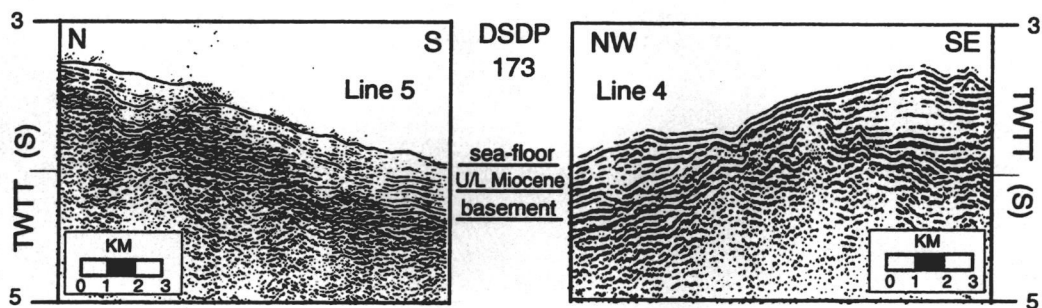


**Figure 2.6** Blow up of MCS data for lines 4 and 5 at their intersection and DSDP Site 173. Depth of the middle/late Miocene boundary converted from twtt is approximate, and no distinct sediment horizon is apparent.

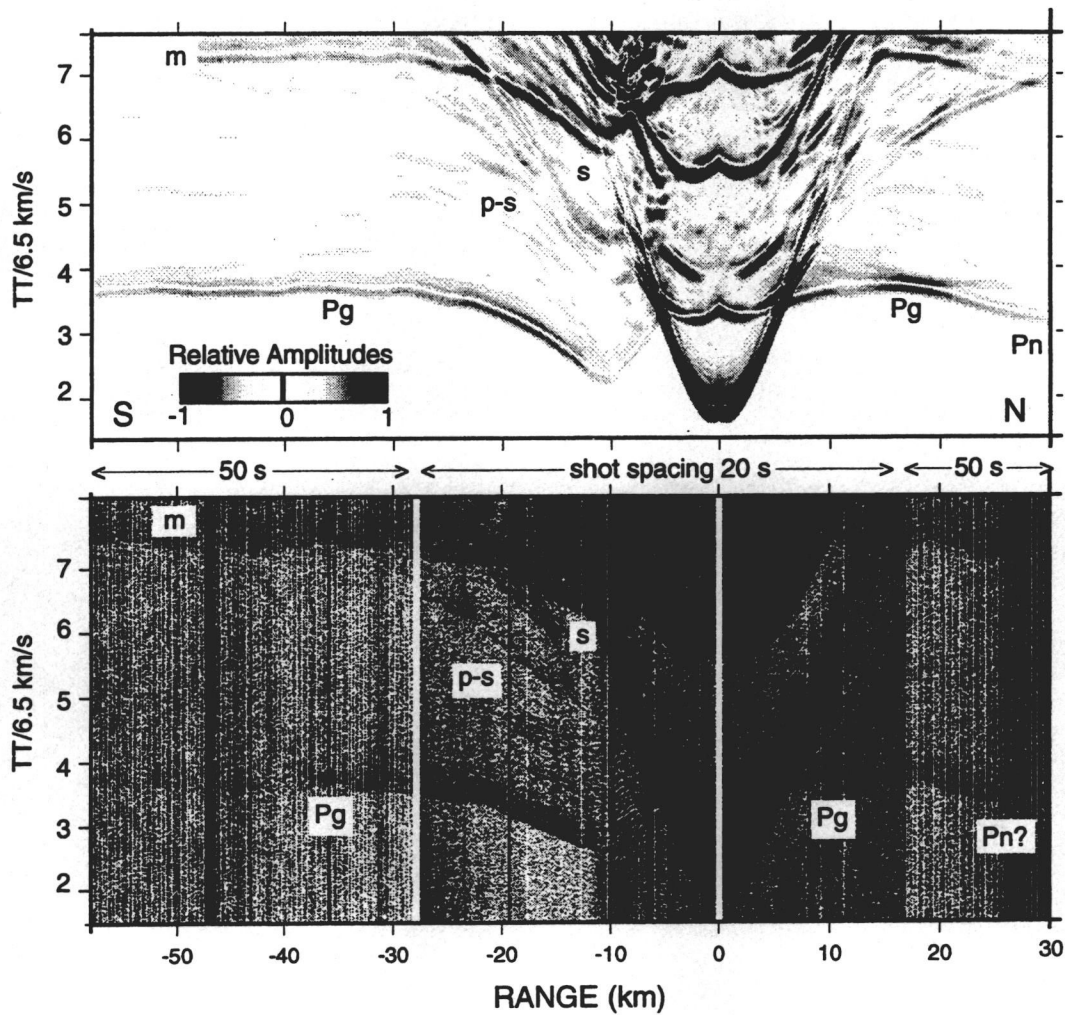


**Figure 2.7** Amplitude plots of (top) synthetic and (bottom) observed record sections of OBH 17. m, multiple caused by reflection at the water surface directly above the instrument; S, shear wave through the ridge; p-s, P-to-S conversion at basement. For comparison see also the record section in Figure 2.3g.

reproduced. We conclude that our model generally explains the amplitude of the observed wave field even in the complicated ridge area.

#### *2.3.1.4 Velocities*

We compare velocities in our models to velocities derived for the onshore Franciscan, offshore Franciscan/San Simeon (paleoaccretionary complex assemblages of pre-Miocene age) and onshore Salinian (granitic batholith) terranes (Figure 2.8). Basement along lines 3S, 4, and 5 (south of the Mendocino transform fault) is likely composed of material similar to the Franciscan and San Simeon terranes. The velocity-depth profile for line 3S at km 30, representative of the western part of the Vizcaino block, has velocities in the upper crust typical of those for San Simeon/Patton terrane. In contrast, velocities at a given depth at km 55 are slightly higher and are consistent with Franciscan or Salinian terrane, which are typically 6-6.3  $\text{kms}^{-1}$ . Velocities in the lower crust along line 3S, however, are too high to be accretionary complex material, and a tectonically or magmatically underplated mafic layer is likely. A reflection at 6-7 s twtt is apparent on a 1977 U.S. Geological Survey MCS reflection line located 10-20 km west of line 5 [McCulloch, 1987a; Godfrey, 1997]. Using our velocity-depth profile, this reflector coincides with the 6  $\text{kms}^{-1}$  contour at about 9 km depth, supporting the interpretation of tectonically underplated oceanic crust.

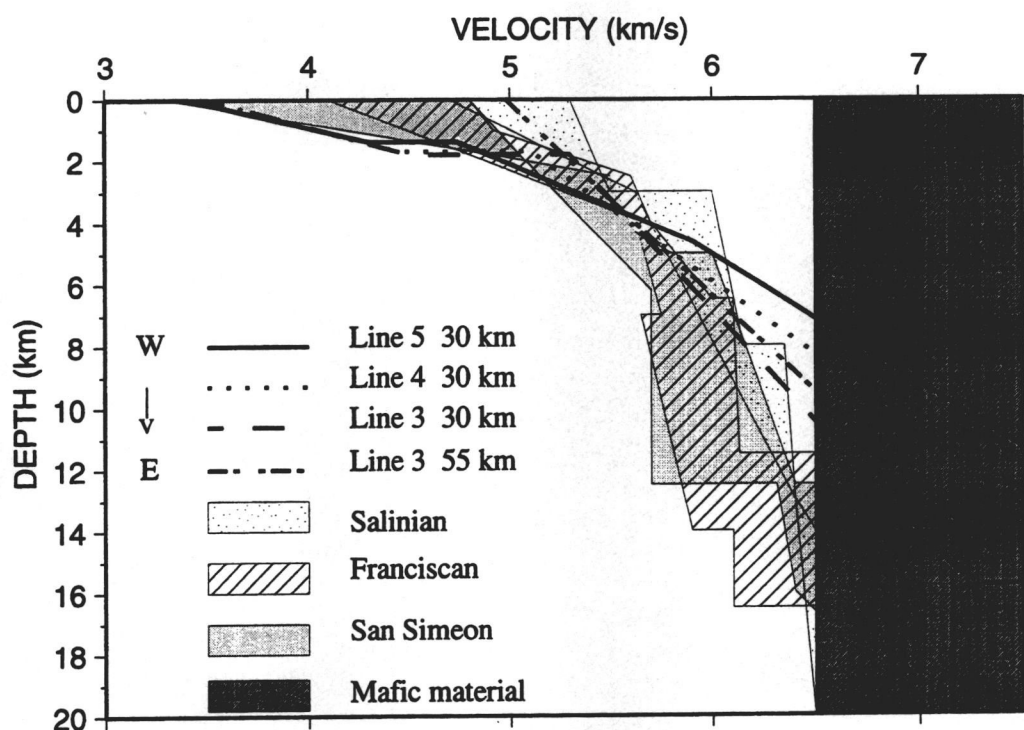


**Figure 2.8** Velocity-depth profiles of lines 3S, 4, and 5 of the velocity models shown in Figure 2.4 (a)-(c). The resolution of our velocity models is best in the top 6 km and decreases with depth. The indicated regions (see legend) mark the range of velocities for Salinian terrane onshore [Walter and Mooney, 1982; Howie et al., 1993], Franciscan terrane onshore [Walter and Mooney, 1982; Howie et al., 1993; Holbrook et al., 1996], and Patton/San Simeon terrane offshore [Howie et al., 1993; Holbrook et al., 1996]. All velocity profiles are normalized to the top of the basement as 0 km. Velocities between 6.5 to 7.5  $\text{km s}^{-1}$  are too high for Salinian, Franciscan, or San Simeon/Patton terrane and represent mafic material or underlying oceanic crust.

### 2.3.2 Modeling the Gravity Data

We modeled free-air gravity anomalies recorded by the R/V *Ewing* along the MCS profiles and merged with the navigation at 1-min time intervals. The Eötvös correction was applied, and the 1980 theoretical gravity field was removed. Data correction procedures and instrumentation on the R/V *Ewing* are described by *Diebold* [1995]. Gravity data derived from satellite altimetry [*Sandwell and Smith, 1997*] supplement the ship-board measurements at the track ends. A 5-10 mGal shift of the global marine gravity data was necessary to overlap the data sets; this is within observed shifts between global marine gravity data and ship board measurements [*Sandwell and Smith, 1997*]. In addition to the free-air anomaly, we calculated a Bouguer anomaly by removing the effect of the topography and sediment layer by replacing them with material of average crustal density ( $2.75 \text{ gcm}^{-3}$  in this study). The Bouguer anomaly reflects density variations beneath the sediment layer and can be compared to other gravity profiles with different topography and basin structure.

The main goals of the gravity modeling were to test and extend the velocity models, putting limits on the Moho where it is not imaged by the seismic data. We did not attempt to match the observed data exactly and focused on explaining long wavelength variations, which reflect density variations beneath the sediment layer. Starting gravity models incorporated bathymetry, changes in sediment thickness, and layer boundaries from the velocity model. The average velocity within layers of variable velocity was used to determine density. Velocity was converted to density using laboratory and field measurements summarized in Table 2.2.

The crust was split into middle and lower crustal layers with densities of  $2.75 \text{ gcm}^{-3}$  and  $2.9 \text{ gcm}^{-3}$ . Lithospheric and asthenospheric densities were derived by adding density contrasts of  $0.4$  and  $0.36 \text{ gcm}^{-3}$  respectively to the density of the lower crust (Table 2.2). Two-dimensional gravity modeling and inversion to obtain the crust-mantle boundary was done with GM\_SYS software (Northwest Geophysical Associates, Corvallis,

Oregon), following the theory of *Talwani et al.* [1959]. RMS values for the models outlined in this study are summarized in Table 2.1.

**Table 2.2** Velocity-Density Conversion References.

Material type	Density ( $\text{gcm}^{-3}$ )	References
Sediment	2.0-2.3	<i>Nafe and Drake</i> [1957]
Franciscan	2.75	<i>Stewart and Peselnick</i> [1977]
Upper oceanic crust	2.75	<i>Christensen and Salisbury</i> [1975]
Lower oceanic crust	2.9	<i>Christensen and Mooney</i> [1995]
Upper mantle	3.3	based on $0.4 \text{ gcm}^{-3}$ density contrast to lower crust [ <i>Jachens and Griscom</i> , 1983]
Asthenosphere	3.26	based on $-0.04 \text{ gcm}^{-3}$ density contrast to upper mantle [ <i>Jachens and Griscom</i> , 1983]

Densities were obtained by using the average velocities from the velocity models and converting to an average density using data from the appropriate reference.

### 2.3.2.1 Line 3S

We constrained the depth to the Moho at the northeastern end of line 3S to be 20 km based on a deep reflection observed on the MCS data at about 8 s twtt [*Henstock et al.*, 1996]. This event is nearly continuous on MCS line 3S from km 45-76 [*Henstock et al.*, 1996]. It is also seen on other profiles crossing the northeastern Vizcaino block [*Godfrey*, 1997; *Godfrey et al.*, 1998].

The Bouguer anomaly (Figure 2.9b) decreases by 150 mGal from west to east. This change is 3 times greater than the change in free-air gravity (50 mGal, Figure 2.9a). We interpret this signal to primarily reflect the change in Moho depth along the profile. Three different density models that all incorporate bathymetry and sediment thickness and

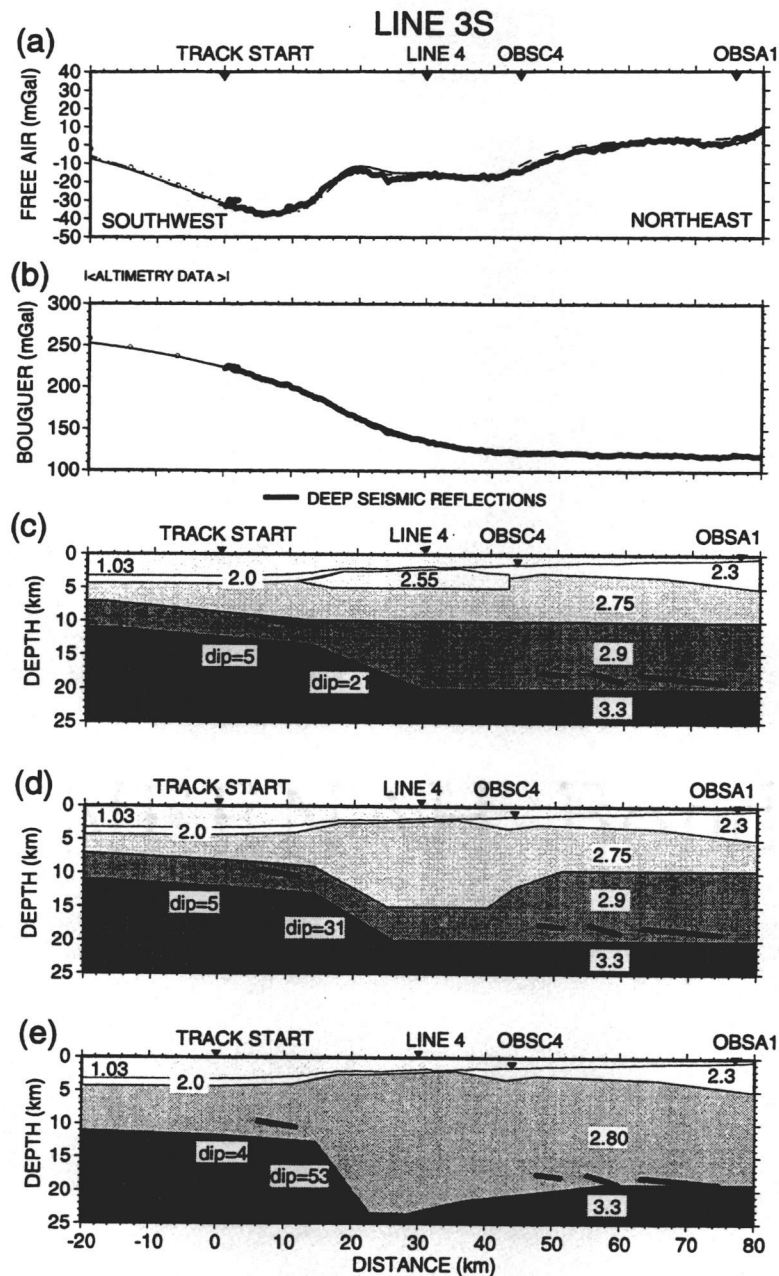


**Figure 2.9** Observed (circles) and calculated (solid line) free air and Bouguer anomalies and density models for lines 3S, 4, and 5. Altimetry data extend the profiles at the track ends. Average block densities are given in  $\text{gcm}^{-3}$ . (a) Free-air anomaly along line 3S of three possible density models shown in Figures 2.9(c), 2.9(d) and 2.9(e). Note the -20 mGal change in free-air gravity between km 40-50. (b) Bouguer anomaly of line 3S is dominated by the density anomaly of the dipping oceanic crust. (c) Density model I along line 3S has a 2-km-thick low-density body of  $2.55 \text{ gcm}^{-3}$  in the upper crust of the Oconostota ridge. (d) Density model II along line 3S has a higher-density lower crust east of the Oconostota ridge. (e) Crust in model III along line 3S has an average density of  $2.8 \text{ gcm}^{-3}$  and therefore explains the change in free air anomaly as a change in depth to the Moho.

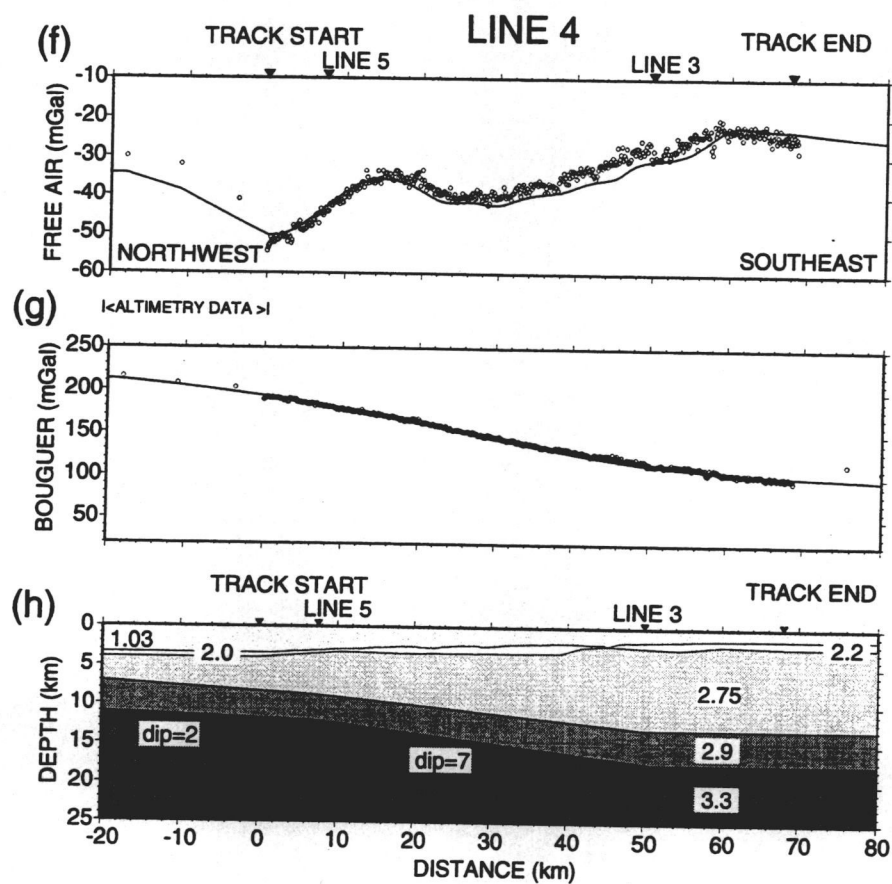


**Figure 2.9** (continued). (f) Free-air anomaly of the line 4 density model. It changes only 30 mGal along the profile. (g) Bouguer anomaly along line 4. (h) Density model of line 4. Moho dips 7° eastward to model km 50.

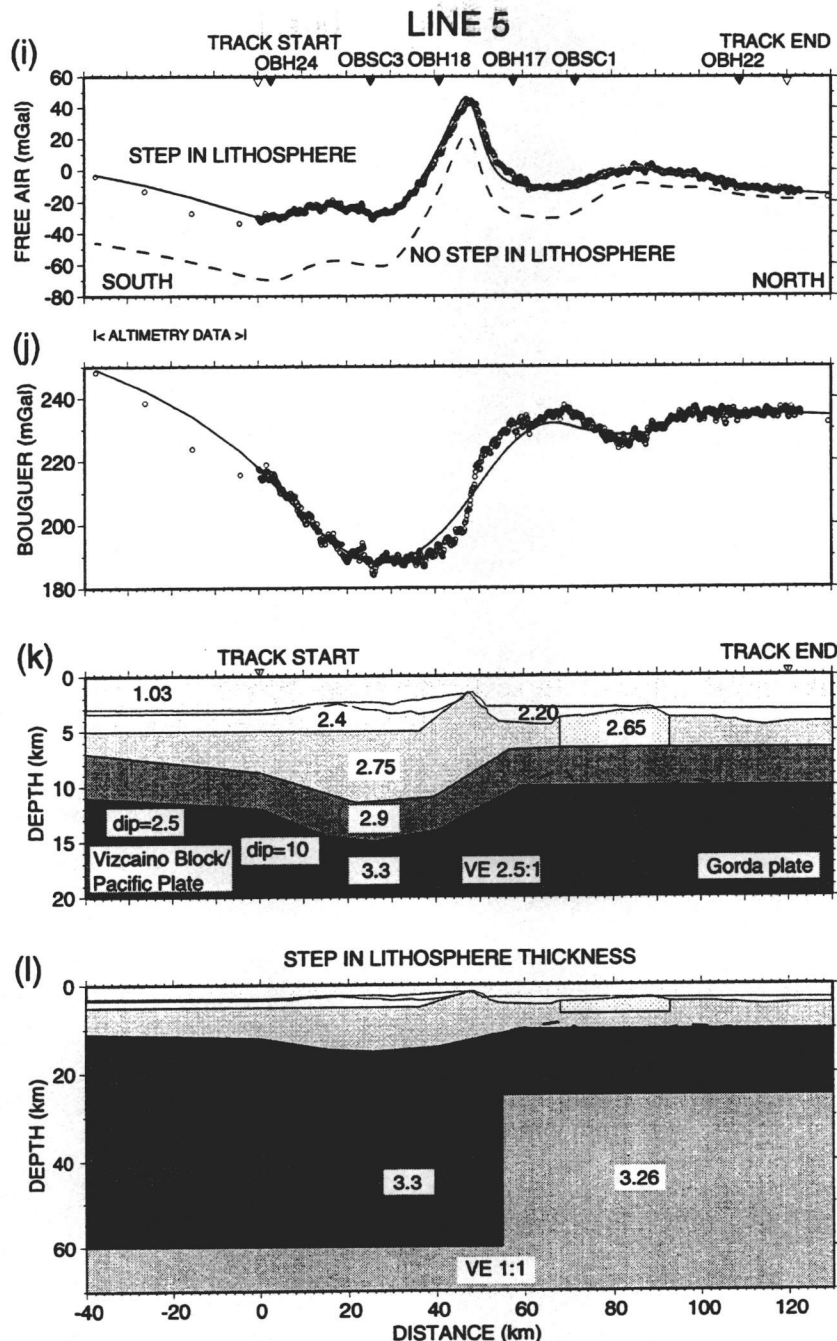


**Figure 2.9** (continued). (i) Free-air anomaly for the line 5 density model with (solid line) and without step in lithosphere thickness (dashed line) across the MTF. (j) Bouguer anomaly along line 5 is dominated by a broad low in the south indicating a thick crust and abrupt thinning at km 50. (k) Density model along line 5 has a shallow dipping Moho to km 0, Moho depth increases to 15 km and the thick crust extends under the ridge crest. The Gorda plate edge is at km 55, and the Moho is flat to the north. Densities between km 60 and 90 km are lower than in the adjacent basement blocks. The data are equally well modeled with a block of  $2.65 \text{ g cm}^{-3}$  in the upper crust (model I in 2.1) or alternately thickening and thinning lower crust (dashed line, model II in Table 2.1). (l) Same as density model in Figure 2.9k), but incorporates a step in lithosphere according to the age contrast of Pacific and Gorda plates.

which are compatible with the gravity data are shown in Figures 2.9c-2.9e. All 3 gravity models show (1) an east dipping, lower crustal layer between km 0 and 15 (dip  $\leq 5^\circ$ ), (2) a transition zone between km 15 and 30 with a steeply dipping Moho (model I =  $21^\circ$ , model II =  $30^\circ$ , model III =  $54^\circ$ ), (3) an abrupt lateral change in density at some depth in the crust or uppermost mantle between km 40 and 50. This density change is needed to account for a 20-mGal increase in the free-air gravity anomaly. Model I (Figure 2.9c) assumes a low-density body ( $2.55 \text{ gcm}^{-3}$  versus  $2.75 \text{ gcm}^{-3}$ ) at a shallow level beneath the Oconostota ridge, as suggested by our velocity model. The observed Moho dip of  $20^\circ$  beneath the Oconostota ridge is a minimum value; a shallower dip would require unreasonable low-density values. Alternatively, the density contrast can be modeled by a relative density high in the lower crust east of model km 45 (model II, Figure 2.9d), which is compatible with the velocity model derived from the onshore-offshore seismic data [Henstock *et al.*, 1996]. Model III was determined from inversion of the gravity data for Moho position assuming no lateral density variations within the crust and illustrates the change in crustal thickness needed to fit this end-member case (Figure 2.9e). Since we do not expect a westward increase in crustal thickness and both models I and II are supported by seismic data, our preferred model is a combination of model I and II with relative weights presently poorly constrained.

#### 2.3.2.2 Line 4

The free-air anomaly (Figure 2.9f) changes by only 40 mGal along the profile. The Bouguer anomaly decreases from west to east, reflecting the increase in Moho depth. Moho dip increases from  $4^\circ$  to  $7^\circ$  at km 8. Between km 8 and 50, Moho depth increases linearly from 12 to 17 km, and east of km 50, the Moho is flat. We did not force the models to agree at the intersections with lines 3S and 5, and therefore the mismatch between the models gives a qualitative measure of model uncertainty. A mismatch in Moho depth of about 3 km between the gravity models for lines 3S and 4 can be partly removed by introducing an additional low-density layer in the line 4 model upper crust, which supports the existence of an intermediate-velocity layer beneath the basement

along line 4. We did not include this layer in our gravity model since it is only based on modeling the large-aperture data near OBH 24. The observed dip of  $7^\circ$  along the line 4 profile contrasts with the steep dip on line 3S in this region, suggesting that line 4 trends obliquely to the sharply dipping structure modeled on line 3S.

### 2.3.2.3 Line 5

The free-air gravity anomaly along line 5 is dominated by large anomalies over the Mendocino Ridge (50-70 mGals), over a bathymetric high on the Vizcaino block (10 mGal) and over a basement high on the Gorda plate (20 mGal) (Figure 2.9i). The Bouguer anomaly is dominated by the change in Moho depth south of the Gorda Escarpment, where a broad low of 50 mGal outlines the thick crust of the Vizcaino block (Figure 2.9j). In addition, the Bouguer gravity has a 10 mGal low between km 60 and 100.

The density model (Figures 2.9k and 2.9l) derived from the velocity model needed three changes to fit the data satisfactorily: (1) A northward dipping Moho (maximum dip  $10^\circ$ ) beneath km 0 and 15, (2) The Gorda plate, modeled either as a low-density block (Figure 2.9k) or, alternatively, thinning and thickening of the oceanic crust between km 70 and 100 (dashed line, Figure 2.9k), (3) a contrast in upper mantle densities corresponding to a lithosphere-asthenosphere boundary calculated from the age contrast [Fowler, 1990, p. 238] between the Gorda (5-6 Ma) and Pacific (27 Ma) plates.

## 2.4 Discussion

The density and velocity models along all three profiles indicate an abrupt increase in Moho dip at the western margin of the Oconostota ridge and a thickened upper crust within the Oconostota ridge. Along line 3S, the dip of the Moho changes abruptly from  $<5^\circ$  at the western end of the profile to  $20\text{-}30^\circ$  (density models I and II, Figures 2.9c and 7d) over a maximum distance of 16 km beneath the seaward boundary of the Vizcaino block and Oconostota ridge. Line 4 is entirely within the Vizcaino block in the region of the Oconostota ridge but trends obliquely to it. The part of line 5 that is south of the Mendocino transform fault also crosses the Oconostota ridge obliquely. The Moho kink modeled beneath the Oconostota ridge on lines 4 and 5 has true dips of  $17^\circ$  and  $20^\circ$ , respectively, when corrected for obliquity (Table 2.3). This is consistent with the minimum value of Moho dip modeled along line 3S (model I). If the Moho dip along Line 3S is in fact larger than  $20^\circ$ , it would imply an increase in Moho dip along strike, but this cannot be resolved with our data set. This Moho dip is much steeper than that observed beneath the accretionary complex anywhere in the active Cascadia subduction margin [Tréhu *et al.*, 1994, 1995; Flueh *et al.*, 1997; Parsons *et al.*, 1998], suggesting that the relict subduction boundary making up the western boundary of the Vizcaino block has been significantly deformed.

**Table 2.3** Geometry of Lines and Apparent and True Dips of Moho Kink

Line	Apparent Moho Dip Along Trend of Line, ( $^\circ$ )	Angle of Line to N45 $^\circ$ E, ( $^\circ$ )	True Dip of Moho Kink ( $^\circ$ )
3	20-30 (Figures 2.9c and 2.9d)	0	20-30
4	7 (Figure 2.9f)	58	17
5	10 (Figure 2.9k)	45	20

Northeast of the Moho kink on line 3S, the Moho flattens at a depth of about 20 km, and we observe a lateral density change within the crust 10-15 km east of the Oconostota ridge. This density change can be modeled either as a change in crustal material, as thinning of the upper crust, or as thickening of the lower crust (or some combination thereof) and coincides with an apparent change in crustal reflectivity and the appearance of a deep reflector to the northeast [Henstock *et al.*, 1996; Godfrey, 1997; Godfrey *et al.*, 1998]. In contrast, no regionally coherent deep reflections are observed on any of the profiles crossing the northwestern region of the Vizcaino block.

Beneath the Gorda Escarpment, the density model of line 5 (Figure 2.9l) indicates abrupt crustal thinning to the north. Matching the long-wavelength data requires that the Mendocino transform fault continues vertically through the plate lithospheres, similar to Wilson's [1989] gravity models across the Mendocino Ridge west of 126°. The high velocities and lack of a crustal root beneath the Mendocino Ridge suggest that it was formed by uplift and tilting of the Vizcaino block in response to Pacific-Gorda compressive forces.

The low-density block and/or Moho variation beneath the basement high on the Gorda plate modeled on line 5 (Figure 2.9k) are not imaged in the large-aperture seismic data. Neither of the density models are compatible with the high being a flexural bulge, as this would result in a relative density high. The basement high may have formed either through thrusting and thickening of the Gorda crust in response to north-south compression, similar to the crustal thickening beneath the Oconostota ridge, or it may be a relict structure created by an excess of magmatism at the spreading center. We prefer the first explanation because the basement high corresponds to a southwest-northeast trending seafloor ridge visible in Gloria sidescan data [EEZ-SCAN84 Scientific Staff, 1986], which approximately coincides with a persistent lineation in the pattern of Gorda plate seismicity and with the aftershock zone of a magnitude 7 intraplate event that occurred in November 1980 [Smith *et al.*, 1993].

## 2.5 Tectonic Implications

The primary result of this study is that the paleosubduction zone preserved along the seaward edge of the Vizcaino block has been significantly deformed. This is suggested by the increase in Moho dip from about  $5^\circ$  west of the Oconostota ridge to  $20\text{-}30^\circ$  beneath the western margin of the Vizcaino block and the Oconostota ridge. This dip is consistent on all three profiles when the apparent dip is corrected for the obliquity of the profiles relative to the northwest trend of the structure indicated by global marine gravity (Figure 2.1b and Table 2.3) and multichannel seismic data [McCulloch, 1987a; Godfrey, 1997]. Crustal thickness farther east is approximately constant, resulting in a kink in the Moho that strikes about  $N45^\circ W$  and underlies the western margin of the Vizcaino block (Figure 2.10a). This type of structure is not observed farther north in Cascadia but is observed on many crossings farther south on the California continental margin [e.g. Trèhu, 1991; Meltzer and Levander, 1991; Howie et al., 1993; Holbrook et al., 1996; Miller et al., 1992, 1996]. It is not observed, however, across the southwestern boundary of the Vizcaino block [Henstock et al., 1997]. In offshore central California, the Moho kink has been attributed to crustal imbrication on thrust faults and/or deformation along buried transform faults.

In order to reconstruct the tectonic processes that lead to the Moho kink and thickened crust, several reflection profiles crossing the Oconostota ridge (red and gray lines, Figure 2.1a) are examined. These profiles show a series of basement ridges overlain by folded sediments (Figures 2.5b, 2.6, and 2.11). Because of their similarity to ridges seen in the active accretionary prism of the Cascadia subduction zone [Goldfinger et al., 1992; Pratson and Haxby, 1996], Godfrey [1997] suggested that these ridges formed in an accretionary complex during the subduction regime and were later reactivated. This outer zone of the accretionary wedge was relatively young, thin, weakened by preexisting faults and thermally weakened by the subducted Farallon ridge beneath it (Figure 2.2b). It is therefore not surprising that deformation was focused in this region. Reactivation of these thrust folds clearly continued until relatively recently (Figures 2.6 and 2.11), but the

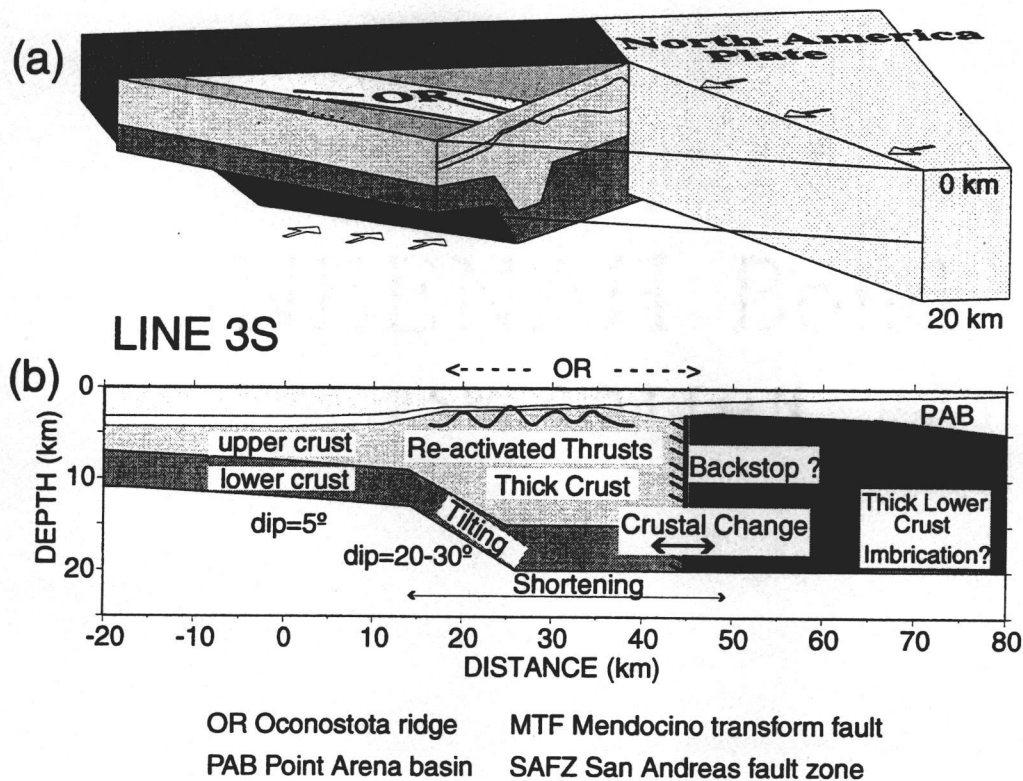


**Figure 2.10** (a) Three-dimensional cartoon of the crustal structure in the northwestern part of the Vizcaino block. The Moho dip abruptly increases to about  $20^\circ$  in the north and  $20-30^\circ$  to the south. The section ends at the southwest-northeast trending line 3S, where our data set ends. The lower crust is shown in dark gray and anything above in lighter gray. The approximate region of the Oconostota ridge is marked in light gray. Mapped basement ridges after Godfrey [1997] are solid lines, dotted where uncertain. Arrows show direction of compression. (b) Sketch of line 3S, which is a cross section of the Vizcaino block. We suggest that compression shortened the lower crust, kinked it, and thickened the upper crust along preexisting thrust faults; faulting and folding the upper crust and sediments. At model km 45, we see a crustal change and possibly thickening of the oceanic crust or mafic layer.

absence of seismicity or of northwest trending ridges on the seafloor suggests that they are not active today. We speculate that the Moho kink represents shortening of the lower crust in response to the same compression that reactivated the thrust faults and thickened the overlying accretionary complex material (Figure 2.10b). Placing constraints on the time of initiation and cessation of reactivation, however, is difficult because of the small number of drill holes in the region, the discontinuous nature of the seismic reflections, the presence of intervening basement ridges, and active seafloor erosion (Figures 2.6 and 2.11). High resolution seismic data near the ODP Site 1022 (yellow circle, Figure 2.1a) suggest that deformation ceased at about 3.4 Ma (Lyle et al., 1997).

Another significant result of our modeling is the apparent thinning of the upper crust and/or thickening of the lower-crust northeast of km 45 on line 3S (Figure 2.10b). The trend of this change in distribution of upper and lower-crustal material is presently poorly constrained because of sparse seismic data and because the wavelength of the gravity anomaly on which this feature is based on is too short to be resolved in global marine gravity data. Based on a general northwest-trending pattern in Neogene structures and gravity data (Figure 2.1a and 2.1b), we assume a northwest trend. Possible explanations for the change in crustal structure include (1) the same compressive event that resulted in the Moho kink, which might have imbricated and thickened the lower crust, (2) extension and magmatic underplating in response to subduction of the Pacific-Farallon ridge, and (3) lateral variations in crustal structure within the forearc formed during Farallon-North America plate subduction. We speculate that higher-velocity and density material 10-15 km east of the Oconostota ridge may represent a mechanical backstop that contributed to localizing deformation beneath the Oconostota ridge (Figure 2.10b).

A third result of the modeling is a new constraint on the composition of material forming the Mendocino Ridge and the geometry of changes in crustal thickness associated with the Gorda Escarpment. The model for line 5 shows that the velocity and density within the Mendocino Ridge are not resolvably different from that within the basement of the adjacent Vizcaino block. Combined with stratigraphic evidence for uplift and tilting of the Mendocino Ridge [*Silver, 1971; Godfrey et al., 1998*], this suggests that the Mendocino Ridge east of 126° is constructed from tectonically uplifted accretionary complex material. We cannot, however, rule out tectonic mixing of accretionary complex

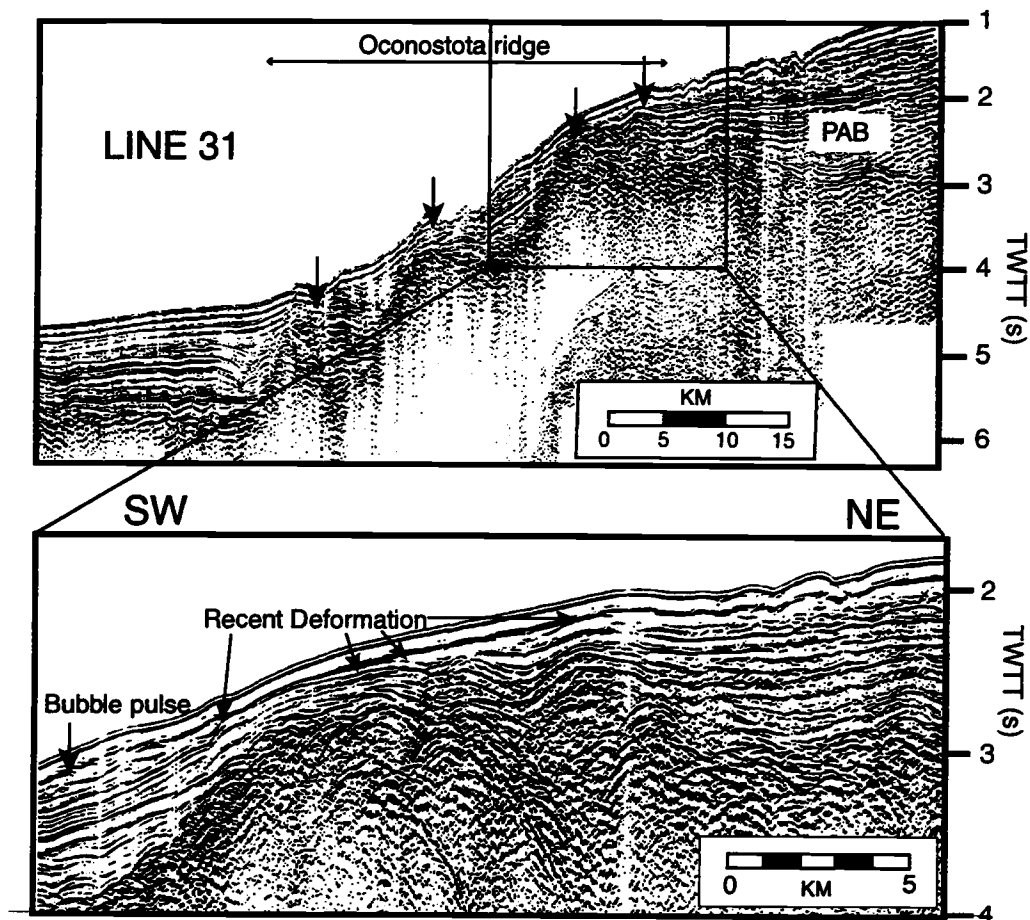


**Figure 2.11** Migrated seismic reflection profile collected by the USGS in 1977 [McCulloch, 1987a; Godfrey, 1997, Godfrey *et al.*, 1998]. Arrows mark the location of the cross cutting basement ridges seen throughout the northwestern Vizcaino block (Figure 2.1a). Bottom figure shows recent sediment deformation above one of the N45°W trending thrust faults.

rocks and uplifted oceanic crust. The configuration of the Moho beneath the Gorda Escarpment indicates that the Mendocino Ridge is not underlain by a crustal root and has therefore been formed and maintained dynamically by compressive forces across the Pacific-Gorda plate boundary. Reported subsidence of the Mendocino Ridge since 5 Ma [Fisk *et al.*, 1993] does not contradict our observations but indicates that compression is decreasing over time. Timing of the uplift and subsequent partial subsidence of the Mendocino Ridge in this region is likely related to changes in the amount of compression across the Mendocino transform fault and to the degree to which compression is accommodated by intraplate deformation.

The formation of the Oconostota ridge and underlying Moho kink and the formation of the Gorda Escarpment and adjacent basement ridge both suggest compressive stress in the Vizcaino block during and/or after its accretion to the Pacific plate, but stratigraphic constraints on the timing of compression are poor. Because these features likely occurred along preexisting faults, the direction of the maximum compressive stress is also poorly constrained.

In order to obtain additional insights into when the deformation or uplift may have occurred, we return to the plate tectonic history summarized in Figure 2.2. In Figure 2.12, we show the lithospheric age contrast across the Pacific-Juan de Fuca/Gorda plate boundary and the component of normal stress across the Mendocino transform and San Andreas fault zones and relate these parameters to the tectonic history of the Vizcaino block as inferred from our crustal models. Figure 2.12 shows that compression across the Mendocino transform was small during a relative stable phase of Pacific plate motion from about 19 to 10 Ma, increased slightly in the period between 10 and 6 Ma, and has been relatively strong since then. It also shows that the lithospheric age contrast across the Mendocino transform near its intersection with the Oconostota ridge flipped 12.5 to 10 Ma and that Pacific-North America relative plate motion was transtensional prior to ~3.5 Ma. In spite of strong normal forces across both plate boundaries at the present time, the lack of seismicity (Plate 1a) and sediment deformation since about 3.4 Ma [Lyle *et al.*, 1997] indicates that the Vizcaino block is not deforming internally under the current stress regime. Since at least 3 Ma, north-south compression has been absorbed internally

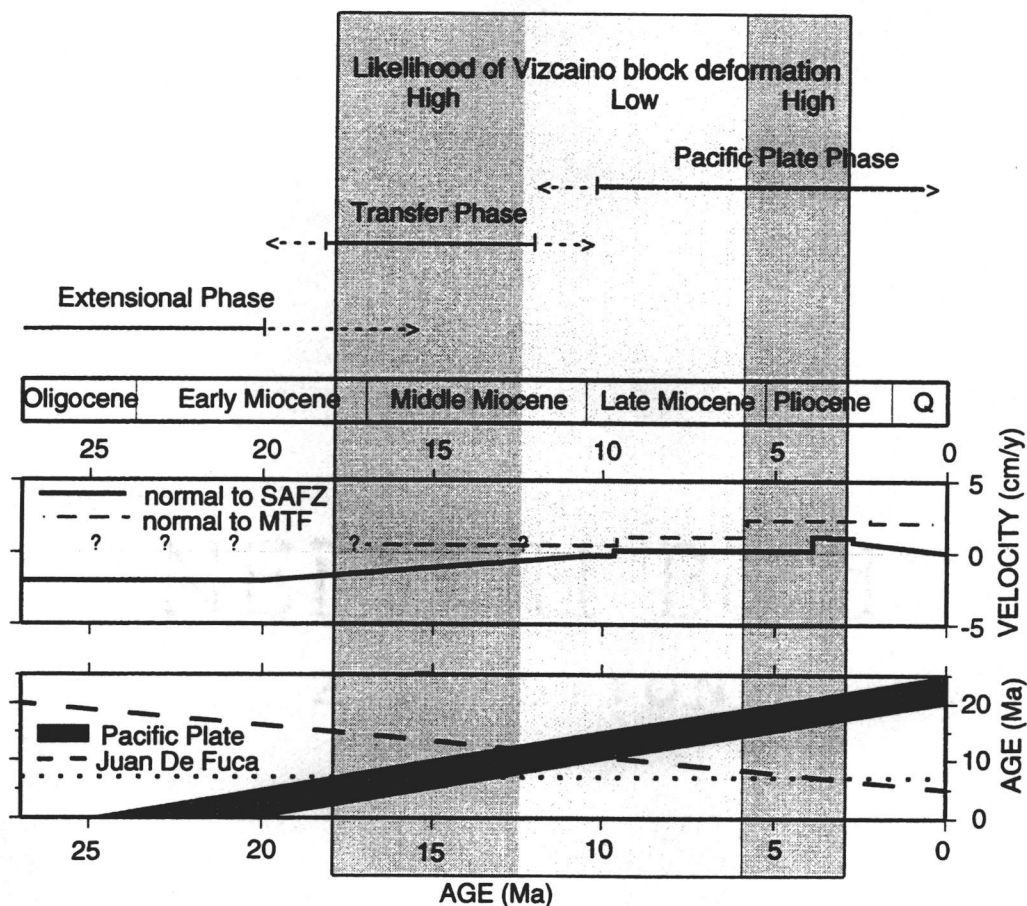


**Figure 2.12** Factors influencing the likelihood of compressional deformation in the Vizcaino block. At the top, solid lines mark lower age and dashed lines mark the upper age limit of the Vizcaino block phases sketched in Figure 2.2. Normal forces across the transforms are calculated from stage poles near the Oconostota ridge-MTF intersection [Wilson, 1993] and just south of the Mendocino triple junction region [Harbert and Cox, 1989] and are projected to a fault at  $90^\circ$  (MTF) and  $319.5^\circ$  (SAFZ). The strike of the San Andreas fault north of Point Arena (since 3.5 Ma) is about  $330^\circ$ , and therefore the present plate motion normal to the San Andreas fault is negligible. Velocity normal to the MTF of the Pacific-Farallon plates between 19 and 10 Ma was relatively small and uncertain. Age of the Farallon and later Juan de Fuca plate [Engebretson *et al.*, 1985] are estimates assuming a constant spreading rate. Pacific plate age is indicated by the dark gray region which marks the possible time span of ridge cessation at about 25 to 20 Ma. The horizontal dotted line marks the onset of Gorda plate deformation (minimum age). When considering the possible Vizcaino block deformation in the early Miocene, we assume that the then young Pacific plate deformed at about the same age. Light gray area indicates small likelihood for Vizcaino block deformation; dark gray areas indicate times of likely deformation.

by the Gorda plate [Wilson, 1989] and east-west compression has been accommodated farther east, within the Point Arena basin [Ondrus, 1997].

We suggest that most of the internal deformation of the Vizcaino block resulted from transpression in response to Pacific-Juan de Fuca/Gorda plate compression (dark gray shaded regions, Figure 2.12) when the normal stresses across the bounding transforms were relatively large (about 6-3 Ma) and/or when the Vizcaino block lower crust was very young, weak, and juxtaposed against the older stronger Juan de Fuca plate to the north (18-12.5 Ma). Internal deformation is less likely in the late Miocene (6-12 Ma), when both north-south compression and the lithospheric age contrast were relatively small (light gray shaded region, Figure 2.12). The observation that internal deformation of the Vizcaino block seems to have stopped and been transferred to the Gorda plate, even though the compressive stress within the Pacific plate should be larger now than at any time in the past history of triple junction interaction, suggests that lithospheric age has a major effect on intraplate deformation.

## 2.6 Conclusions

Our data show evidence for significant deformation of the crust in the northwestern part of the Vizcaino block. The internal deformation resulted primarily from transpression in response to Pacific-Juan de Fuca plate compression when normal stresses across the bounding transforms were relatively large (6-3.4 Ma) and/or when the Vizcaino block was considerably younger and weaker than the adjoining Juan de Fuca plate (18-12.5 Ma). This compression appears to have reactivated preexisting crustal faults, thickened the crust of the Oconostota ridge, and formed a kink in the Moho beneath the northwestern margin of the Vizcaino block. It also tilted and uplifted the Vizcaino block at its northern margin, forming the Gorda Escarpment and adjacent basement ridge. A lateral change in structure is observed to the northeast of the Oconostota ridge, but it is unclear if this is a product of the same deformation or was a preexisting feature and therefore acted as a backstop during the deformation. Deformation within the Vizcaino block appears to have ceased and shifted to the Gorda

plate sometime prior to 3 Ma. We suggest that the spatial and temporal shifts of the primary locus of deformation resulted from changes in relative motions across the Pacific, Juan de Fuca/Gorda and North America plate boundaries combined with changes in lithospheric age and age contrast across these boundaries.

## 2.7 Acknowledgments

Special thanks to the participants of the Mendocino Triple Junction Seismic Experiment, to the crews of the R/V *Ewing* and R/V *Wecoma* and to Ken Peals, Beecher Wooding and Greg Miller for running the OBS/OBHs. Thanks to T. Henstock, who provided the depth-migrated MCS profile for line 3S, and to A. S. Meltzer, who provided the time-migrated profile for line 5. Reviews by T. Brocher, R. Keller, and K. Miller greatly improved this manuscript. B. Leitner gratefully acknowledges the support of J. L. Nábelek and D. Eberhart Phillips. Gerald Connard at Northwest Geophysical Associates (Corvallis, Oregon) provided a test copy of GM\_SYS for Unix. Plots were created using GMT [Wessel and Smith, 1995]. This research was supported by NSF grants 9219870-EAR and 9527011-EAR to Oregon State University and EAR-9218209 to Stanford University.

## 2.8 References

- Atwater, T., Implications of plate tectonics for the Cenozoic tectonic evolution of western North America, *Geol. Soc. Am. Bull.*, 81, 3513-3536, 1970.
- Atwater, T., Plate tectonic history of the northeast Pacific and western North America, in *The Geology of North America*, vol. N, *The Eastern Pacific Ocean and Hawaii*, edited by E. L. Winterer, D. M. Hussong, and R. W. Decker, pp. 21-72, Geol. Soc. of Am., Boulder, Colo., 1989.
- Atwater, T., and J. Severinghaus, Tectonic maps of the northeast Pacific, in *The Geology of North America*, vol. N, *The Eastern Pacific Ocean and Hawaii*, edited by E. L. Winterer, D. M. Hussong, and R. W. Decker, pp. 15-20, Geol. Soc. of Am., Boulder, Colo., 1989.
- Blake, M. C., Jr., and D. L. Jones, The Franciscan assemblage and related rocks in northern California: A reinterpretation, *The Geotectonic Development of California*, edited by W. G. Ernst, pp. 307-328, Prentice-Hall, Englewood Cliffs, N.J., 1981.
- Bohannon, R. G., and T. Parsons, Tectonic implications of post-30 Ma Pacific and North American relative plate motions, *Geol. Soc. Am. Bull.*, 107, 937-959, 1995.
- Bonatti, E., Vertical tectonism in oceanic fracture zones, *Earth Planet. Sci. Lett.*, 37, 369-379, 1978.
- Braunmiller, J., B. Leitner, J. Nábelek, and A. M. Tréhu, Location and source parameters of the 19 June 1994 ( $M_w=5.0$ ) offshore Petrolia, California, earthquake, *Bull. Seismol. Soc. Am.*, 87, 272-276, 1997.
- Castillo, D. A., and W. L. Ellsworth, Seismotectonics of the San Andreas fault system between Point Arena and Cape Mendocino in northern California: Implications for the development and evolution of a young transform, *J. Geophys. Res.*, 98, 6543-6560, 1993.
- Christensen, N. I., and W. D. Mooney, Seismic velocity structure and composition of the continental crust: A global view, *J. Geophys. Res.*, 100, 9761-9788, 1995.

- Christensen, N. I., and M. H. Salisbury, Structure and constitution of the lower oceanic crust, *Rev. Geophys.*, 13, 57-86, 1975.
- Christeson, G. L., Y. Nakamura, K. D. McIntosh, and P. Stoffa, Effect of shot interval on ocean bottom seismograph and hydrophone data, *Geophys. Res. Lett.*, 23, 3783-3786, 1996.
- Cox, A., and D. Engebretson, Change in motion of Pacific plate at 5 Myr BP, *Nature*, 313, 472-474, 1985.
- Denlinger, R. P., A model for large-scale plastic yield of the Gorda deformation zone, *J. Geophys. Res.*, 97, 15415-15423, 1992.
- Dickinson, W. R., and W. S. Snyder, Geometry of triple junctions related to San Andreas transform, *J. Geophys. Res.*, 84, 561-572, 1979.
- Diebold, J., *R/V Ewing leg EW9412*, Lamont-Doherty Earth Obs., Columbia Univ., Palisades, N.Y., 1995.
- Drake, D. E., D. A. Cacchione, J. V. Gardner, D. S. McCulloch and D. Masson, Morphology and growth history of Delgada fan: Implications for the Neogene evolution of Point Arena basin and the Mendocino triple junction, *J. Geophys. Res.*, 94, 3139-3158, 1989.
- Duncan, R. A., and D. A. Clague, Pacific plate motion recorded by linear volcanic chains, in *The Ocean Basins and Margins*, vol. 7A, edited by A. E. M. Nairn, F. G. Stehli, and S. Uyeda, pp. 89-121, New York, Plenum, 1985.
- Duncan, R. A., M. R. Fisk, A. G. Carey Jr., D. Lund, L. Douglas, D. S. Wilson, D. Krause, R. Stewart, and C. G. Fox, Origin and emergence of Mendocino Ridge (abstract), *Eos Trans. AGU*, 75 (44), Fall Meet. Suppl., 475, 1994.
- EEZ-SCAN 84 Scientific Staff, Atlas of the exclusive economic zone, western conterminous United States, *U.S. Geol. Surv. Misc. Invest.*, I-1792, 152 pp., 1986.

- Engebretson, D. C., Cox, and R. G. Gordon, Relative motions between oceanic and continental plates in the Pacific Basin, *Geol. Soc. Am. Spec. Pap.*, 206, 59 pp., 1985.
- Fernandez, L. S., and R. N. Hey, Late Tertiary tectonic evolution of the seafloor spreading system off the coast of California between the Mendocino and Murray fracture zones, *J. Geophys. Res.*, 96, 17955-17979, 1991.
- Fisk, M. R., R. A. Duncan, C. G. Fox, and J. B. Witter, Emergence and petrology of the Mendocino Ridge, *Mar. Geophys. Res.*, 15, 283-296, 1993.
- Flueh, E., M. Fisher, D. Scholl, T. Parsons, U. ten Brink, D. Klaeschen, N. Kukowski, A. Tréhu, J. Childs, J. Bialas, and N. Vidal, Scientific teams analyze earthquake hazards of the Cascadia subduction zone, *Eos Trans. AGU*, 78, 153-157, 1997.
- Fowler, C. M. R., *The solid earth*, An introduction to global geophysics, 472 pp., Cambridge University Press, 1990.
- Godfrey, N. J., Crustal structure of northern California, Ph.D. thesis, Stanford University press, Stanford, 177 pp., 1997.
- Godfrey, N. J., A. S. Meltzer, S. L. Klemperer, A. M. Tréhu, B. Leitner, S. H. Clarke Jr. and A. Ondrus, Evolution of the Gorda Escarpment, San Andreas fault, and Mendocino triple junction from multichannel seismic data collected across the northern Vizcaino block, offshore northern California, *J. Geophys. Res.*, 103, 23795-23812, 1998.
- Goldfinger, C., L. D. Kulm, R. S. Yeats, B. Appelgate, M. E. MacKay, and G. F. Moore, Transverse structural trends along the Oregon convergent margin; Implications for Cascadia earthquake potential and crustal rotations, *Geology*, 10, 141-144, 1992.
- Graham, S. A., and W. Dickinson, Evidence for 115 kilometers of right slip on the San Gregori-Hosgri fault trend, *Science*, 199, 179-181, 1978.
- Griscom, A., and R. C. Jachens, Tectonic history of the north portion of the San Andreas fault system, California, inferred from gravity and magnetic anomalies, *J. Geophys. Res.*, 94, 3089-3099, 1989.

- Harbert, W., and A. Cox, Late Neogene motion of the Pacific plate, *J. Geophys. Res.*, *94*, 3052-3064, 1989.
- Henstock, T. J., A. Levander, and the Mendocino Working Group, Images of the Mendocino and San Andreas transforms in the Mendocino triple junction region: Continous seismic profiling across the continental margin (abstract), *Eos Trans. AGU*, *77* (46), Fall Meet. Suppl., F741, 1996.
- Henstock, T. J., A. Levander, and J. A. Hole, Deformation in the lower crust of the San Andreas fault system in northern California, *Science*, *278*, 650-653, 1997.
- Holbrook, W. S., T. M. Brocher, U. S. ten Brink, and J. A. Hole, Crustal structure of a transform plate boundary: San Francisco Bay and the central California continental margin, *J. Geophys. Res.*, *101*, 22311-22334, 1996.
- Hoskins, E. G., and J. R. Griffiths, Hydrocarbon potential of northern and central California offshore, *Future Petroleum Provinces of the United States, Marine Geology and Potential*, edited by I. H. Cram, *AAPG Mem.*, *15*, 212-228, 1971.
- Howie J. M., K. C. Miller, and W. U. Savage, Integrated crustal structure across the south central California margin: Santa Lucia escarpment to the San Andreas fault, *J. Geophys. Res.*, *98*, 8173-8196, 1993.
- Jachens, R. C., and A. Griscom, Geometry of the Gorda plate beneath northern California, *J. Geophys. Res.*, *88*, 9375-9392, 1983.
- Krause, D. C., H. W. Menard, and S. M. Smith, Topography and lithology of the Mendocino Ridge, *J. Mar. Res.*, *22*, 236-249, 1964.
- Kulm, L. V. D., R. von Huene, J. R. Duncan, J. C. J. Ingle, S. A. Kling, L. F. Musich, D. J. W. Piper, R. M. Pratt, H. Scradler, O. E. Weser, and S. W. J. Wise, Site 173, *Initial Rep. Deep Sea Drill. Proj.*, *18*, 31-62, 1973.
- Lendl, C., Finite difference wavefield modeling of large-aperture data from the 1993 Mendocino Triple Junction Seismic Experiment, master thesis, 163 pp., Oreg. State Univ., Corvallis, 163, 1996.

- Lendl, C., A. M Tréhu, J. A. Goff, A. R. Levander, and B. C. Beaudoin. Synthetic seismograms through synthetic Franciscan: Insights into factors affecting large-aperture seismic data. *Geophys. Res. Lett.*, 24, 3317-3320, 1997.
- Lonsdale, P., Structural patterns of the Pacific floor offshore of Peninsular California, in *Gulf and Peninsular Provinces of the Californias*, edited by P. Dauphin, J. Ness and B. Simoneit, *AAPG Mem.*, 47, 87-125, 1991.
- Lyle, M., I. Koizumi, C. Richter, and the Shipboard Scientific Party, *Proceedings of the Ocean Drilling Program: Initial Reports, V. 167*, Ocean Drill. Program, College Station, Tex., 1997.
- Mattinson, J. M., Age, origin, and thermal histories of some plutonic rocks from the Salinian block of California, *Contrib. Mineral. Petrol.*, 67, 233-245, 1978.
- McCrary, P. A., D.S. Wilson, J.C. Ingle Jr., and R.G. Stanley, Neogene geohistory analysis of Santa Maria Basin, California, and its relationship to transfer of central California to the Pacific plate, *U.S. Geol. Surv. Bull.*, J, 1-38, 1995.
- McCulloch, D. S., The Vizcaino block south of the Mendocino triple junction, northern California, *Tectonics, Sedimentation and Evolution of the Eel River and Associated Basins of northern California, Proceedings of a Symposium*, edited by H. Schymiczek and R. Suchland, pp. 129-137, San Joaquin Geol. Soc. Misc. Publ., Bakersfield, Cal., 1987a.
- McCulloch, D. S., Regional geology and hydrocarbon potential of offshore central California, in *Geology and Resource Potential of the Continental Margin of Western North America and Adjacent Ocean Basins - Beaufort Sea to Baja California*, *Earth Sci. Ser.*, vol. 6, edited by D. W. Scholl, A. Grantz and J. G. Vedder, pp. 353-401, Circum-Pac. Counc. for Energy and Miner. Resour., Houston, Tex., 1987b.
- McCulloch, D. S., Evolution of the offshore central California margin, in *The Geology of North America*, vol. N, *The Eastern Pacific Ocean and Hawaii*, edited by E. L. Winterer, D. M. Hussong, and R. W. Decker, pp. 439-470, Geol. Soc. of Am., Boulder, Colo., 1989.
- McLaughlin R. J., S. A. Kling, R. Z. Poore, K. McDougall, and E. C. Beutner, Post-middle Miocene accretion of Franciscan rocks, northwestern California, *Geol. Soc. Am. Bull.*, 93, 595-605, 1982.

- McLaughlin, R. J., W.V. Sliter, N. O. Frederiksen, W. P. Harbert, and D. S. McCulloch, Plate motions recorded in Tectonostratigraphic terranes of the Franciscan complex and evolution of the Mendocino triple junction, northwestern California, *U.S. Geol. Surv. Bull.*, 1997, 60 pp., 1994.
- McLaughlin, R. J., W.V. Sliter, D.H. Sorg, P.C. Russell, and A.M. Sarna-Wojcicki, Large-scale right-slip displacement on the East San Francisco Bay region faults system, California: Implications for location of late Miocene to Pliocene Pacific plate boundary, *Tectonics*, 15, 1-18, 1996.
- Meltzer, A.S., and A. R. Levander, Deep crustal reflection profiling offshore southern central California margin, *J. Geophys. Res.*, 96, 6475-6491, 1991.
- Miller, K.C., J. M. Howie, and S. D. Ruppert, Shortening within underplated oceanic crust beneath the central California margin, *J. Geophys. Res.*, 97, 19961-19980, 1992.
- Miller, K. C., M. Dober, F. Hua, and R. G. Bohannon, Crustal gravity models along seismic reflection profiles, California Continental Borderland (abstract), *Eos Trans. AGU*, 77 (46), Fall Meet. Suppl., F737, 1996.
- Nafe, J. E., and C. L. Drake, Variation with depth in shallow and deep marine sediments of porosity, density and the velocities of compressional and shear waves, *Geophysics*, 22, 523-552, 1957.
- Nicholson, C., C. Sorlien, T. Atwater, J. Crowell, and B. Luyendyk, Microplate capture, rotation of the western Transverse Ranges, and initiation of the San Andreas transform as a low-angle fault system, *Geology*, 22, 491-495, 1994.
- Ondrus, A., Deformation of the Point Arena basin and the location of the San Andreas Fault Zone, offshore northern California, M.S. thesis, 46 pp., Lehigh Univ., Bethlehem, Pa., 1997.
- Parsons, T., A. M. Tréhu, J. H. Luetgert, F. Kilbride, K. Miller, R. E. Wells, M. A. Fisher, N. I. Christensen, U. S. ten Brink, E. Flueh, and W. D. Mooney, A new view into the Cascadia subduction zone and volcanic arc: Implications for earthquake hazards along the Washington margin, *Geology*, 26, 199-292, 1998.

- Pratson, L. F., and W. F. Haxby, What is the slope of the U. S. continental slope?, *Geology*, 24, 3-6, 1996.
- Riddihough, R. P., Gorda plate motions from magnetic anomaly analysis, *Earth Planet. Sci. Lett.*, 51, 163-170, 1980.
- Riddihough, R. P., Recent movements of the Juan de Fuca plate system, *J. Geophys. Res.*, 89, 6980-6994, 1984.
- Rodrigues, D. and P. Mora, Analysis of a finite difference solution to the three-dimensional elastic wave equation, paper presented at 67nd. Annual International Meeting, Soc. for Explor. Geophys, 1992.
- Sandwell, D. T., and W. H. F. Smith, Marine gravity anomaly from Geosat and ERS 1 satellite altimetry, *J. Geophys. Res.*, 102, 10039-10054, 1997.
- Sedlock, R. L., and D. H. Hamilton, Late Cenozoic tectonic evolution of southwestern California, *J. Geophys. Res.*, 96, 2325-2351, 1991.
- Severinghaus, J., and T. Atwater, Cenozoic geometry and thermal state of the subducting slabs beneath western North America, in B. P. Wernicke, *Basin and Range Extensional Tectonics Near the Latitude of Las Vegas, Nevada*, edited by Geol. Soc. of Am. Mem., 176, 1-22, 1990.
- Silver, E. A., Tectonics of the Mendocino triple junction, *Geol. Soc. Am. Bull.*, 82, 2965-2978, 1971.
- Smith, S. W., J. S. Knapp, and R. C. McPherson, Seismicity of the Gorda plate, structure of the continental margin, and an eastward jump of the Mendocino triple junction, *J. Geophys. Res.*, 98, 8153-8171, 1993.
- Stewart, R., and L. Peselnick, Compressional velocities in dry Franciscan rocks to 8 kbar and 300°C, *J. Geophys. Res.*, 83, 2027-2039, 1977.
- Stoddard, P. R., A kinematic model for the evolution of the Gorda plate, *J. Geophys. Res.*, 92, 11524-11532, 1987.

- Talwani, M., J. L. Worzel, and M. Landisman, Rapid gravity computations for two-dimensional bodies with application to the Mendocino submarine fracture zone, *J. Geophys. Res.*, *64*, 49-59, 1959.
- Tréhu, A. M., Tracing the subducted oceanic crust beneath the central California continental margin: Results from ocean bottom seismometers deployed during the 1986 Pacific Gas and Electric EDGE Experiment, *J. Geophys. Res.*, *96*, 6493-6506, 1991.
- Tréhu, A. M., I. Asudeh, T. M. Brocher, J. H. Luetgert, W. D. Mooney, and J. L. Nábelek, Crustal architecture of the Cascadia forearc, *Science*, *266*, 237-242, 1994.
- Tréhu, A. M., and the Mendocino Working Group, Pulling the rug out from under California: Seismic images of the Mendocino triple junction region, *Eos Trans. AGU*, *76*, 369, 380-381, 1995.
- Walter, A. W., and W. D. Mooney, Crustal structure of the Diablo and Gabilan Ranges, central California: A reinterpretation of existing data, *Bull. Seismol. Soc. Am.*, *72*, 1567-1590, 1982.
- Wessel, P., and W. H. F. Smith, New version of the generic mapping tools released, *Eos Trans. AGU*, *76*, 329, 1995.
- Wilson, D. S., A kinematic model for the Gorda deformation zone as a diffuse southern boundary of the Juan de Fuca plate, *J. Geophys. Res.*, *91*, 10259-10269, 1986.
- Wilson, D. S., Tectonic history of the Juan de Fuca ridge over the last 40 million years, *J. Geophys. Res.*, *93*, 11863-11876, 1988.
- Wilson, D. S., Deformation of the so-called Gorda plate, *J. Geophys. Res.*, *94*, 3065-3075, 1989.
- Wilson, D. S., Confidence intervals for motion and deformation of the Juan de Fuca plate, *J. Geophys. Res.*, *98*, 16053-16071, 1993.
- Wilson, D. S., R. N. Hey, and C. Nishimura, Propagation as a mechanism of orientation of the Juan de Fuca Ridge, *J. Geophys. Res.*, *89*, 9215-9225, 1984.

Zelt, C. A., and R. B. Smith, Seismic traveltime inversion for 2-D crustal velocity structure, *Geophys. J. Int.*, 108, 16-34, 1992.

## **Chapter 3**

### **A Focused Look at the Alpine Fault, New Zealand: Seismicity, Focal Mechanisms and Stress Observations**

**Beate Leitner, Donna Eberhart-Phillips, Helen Anderson, and John L. Nábelek**

**In preparation for submission to the Journal of Geophysical Research**

### 3.1 Abstract

The Alpine fault is the Pacific-Australian plate boundary in the South Island of New Zealand. Depth and mechanisms of small earthquakes in the central South Island are not resolved routinely by the present permanent national seismic network. This study analyses 195 earthquakes recorded during the 6 month duration of the Southern Alps Passive Seismic Experiment (SAPSE) in 1995/1996 and 2  $M_L$  5.0 earthquakes and aftershocks in 1997, which occurred close to the central part of the Alpine fault. Precise earthquake locations are derived by simultaneous inversion for hypocenter parameters, a 1-D velocity model, and station corrections. Together with focal mechanisms calculated using a first motion and amplitude ratio method, these results provide a picture of the seismotectonics in the central South Island over a 6 month period. Moment tensor inversions of 5 earthquakes provide an independent means of comparison to the focal mechanisms derived with the amplitude/first motion method. To validate our observations over time, we compare the SAPSE seismicity with the seismicity recorded by the New Zealand National Seismic Network (NZNSN) and a local network at Lake Pukaki east of the Southern Alps (6 month versus 8 years).

Our study indicates that the Alpine fault releases elastic strain seismically from the surface down to 10-12 km depth between Milford Sound in the south and the intersection of the Alpine fault with the Hope fault in the north. The base of the seismogenic zone is uniform at 10-12 km depth throughout the central South Island. Elevated isotherms have wavelengths smaller than 30 km and are located to the east of the surface trace of the Alpine fault. The seismicity rate of the Alpine fault is low, but comparable to locked sections of the San Andreas fault, with large earthquakes expected. Seismicity decreases north of Bruce Bay, indicating a different behaviour of the Alpine fault to the north. In the north, a triangular shaped region along the Alpine fault located between the Hope and Porters Pass fault zones is characterised by the absence of earthquakes. We interpret this as the result of the plate boundary shift from the Alpine fault to the Hope and Porters Pass fault zones. In this northern region, the seismic activity is constrained to a narrow

corridor about 60 km wide; south of it the seismicity is observed as far as 100 km east of the Alpine fault. Most of the study region appears to deform under a uniform stress field with a maximum principal horizontal stress direction of 110-120°, consistent with geodetic observations and plate motions. This confirms that the Alpine fault is not undergoing strain partitioning. The earthquake data reveal a strong 3-D character of the plate boundary deformation and show that the deformation away from the Alpine fault is distributed on mainly NNE trending thrust faults and strike-slip transfer faults with a maximum seismogenic depth of 10-12 km.

### 3.2 Introduction

The central South Island of New Zealand presents a continent/continent collision zone, where a large part of the transpressional plate motion between the Australian and Pacific plates is accommodated by the Alpine fault (Figure 3.1). Erosion on the western side of the Southern Alps exposes continuously uplifting lower crustal material, accommodating part of the shortening component of the oblique plate motion. The Alpine fault accommodates oblique plate motion on a single structure, whereas similar convergence near the San Andreas fault in California is partitioned into strike slip on the San Andreas fault and dip-slip normal to the San Andreas fault on nearby structures.

In the last 10 years, numerical plate deformation models have improved our understanding of the tectonic evolution of this plate boundary by modeling measured uplift rates, plate convergence, crustal thickening, heat flow, and erosion. By modeling the present day topography, strain rates, and thermal structure along 2-D profiles the effect of the model parameters can be assessed. The region between Jackson Bay and the intersection of the Alpine fault with the Hope fault (Figure 3.2) is often assumed for reason of model simplicity to behave in a 2-D fashion, despite evidence for lateral variation of the model parameters. The earthquake data reveal a 3-D structural character of the plate boundary and provide important constraints on the depth of the brittle/ductile transition zone in this region.

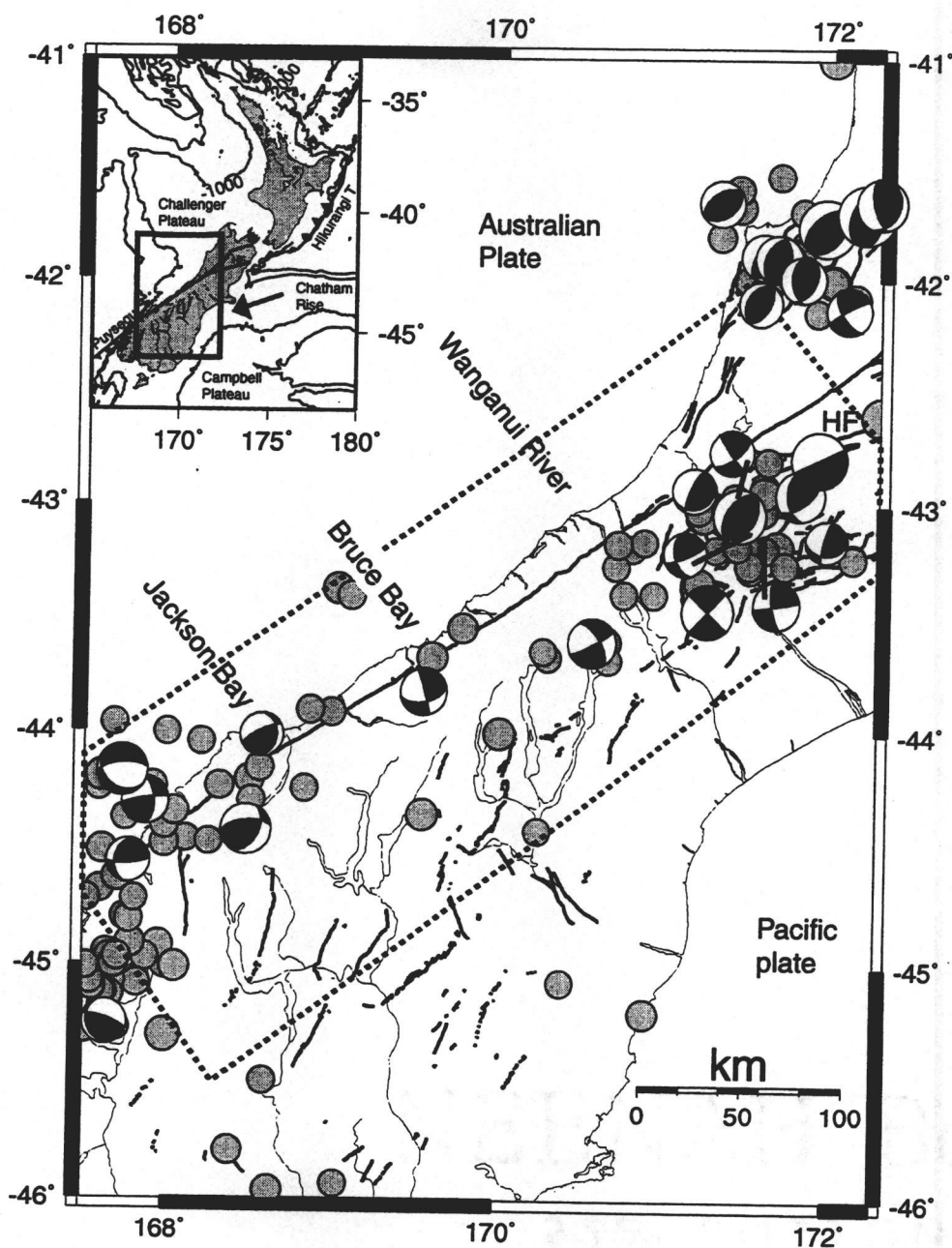


**Figure 3.1** Earthquakes and focal mechanisms derived from body waveform modeling plotted in lower hemisphere projection [Harvard CMT catalogue; *Anderson et al.*, 1993; *Doser and Webb*, submitted] for  $M_w > 5.4$  in the South Island. Grey circles are earthquakes with  $M_L > 5$  recorded since 1920. Dashed line outlines the study region. Inset shows 1000 m bathymetry contours delineating the continental plateaus converging obliquely along the Australian and Pacific plate boundary. Arrow gives the direction of relative plate motion between the plates calculated with the Nuvel 1A rotation pole [*DeMets et al.*, 1994]. The solid box is the map region shown in the enlargement. HF Hope fault.

In this paper new precise earthquake locations and mechanisms throughout the central South Island are determined and interpreted together with results from existing earthquake studies, from thermal and strain models across the plate boundary, from new results of a comprehensive multi-geophysical investigation along 2 transects, and repeat measurements of an array of GPS stations in the region between the transect lines.

### 3.3 Overview

The study region comprises a corridor 150 km wide parallel to the Australian and Pacific plate boundary (Figure 3.1 and 3.2). It is dominated by the 600 km long Alpine fault to the west and is bounded to the north by the Marlborough fault system and in the south by the Puysegur subduction zone. West of the Alpine fault Paleozoic and Mesozoic granitoid, gneiss and lower Paleozoic metasedimentary basement is overlain by up to 500 m thick glacial deposits. The region east of the Alpine fault consists of schist and greywacke (Figure 3.2) underlain by a layer of oceanic crust, dipping westwards [Holbrook *et al.*, 1998; Kleffman *et al.*, 1998; Reyners, 1987; Stern *et al.*, 1997]. The eastern limit of tectonic uplift follows the eastern foothills of the Southern Alps. Prior to this study, earthquake data were too limited to resolve the seismotectonic character of this diverse region in the central South Island in detail. Earthquake depths and mechanisms were only available from microseismicity studies near Lake Pukaki [Reyners, 1988] and along parts of the Alpine fault [Scholz *et al.*, 1974], and are not resolvable from the New Zealand National Seismic Network (NZNSN) due to the sparse station distribution and low magnitudes of earthquakes.

In this study, this information gap is filled by providing precise earthquake locations and focal mechanisms for  $M_L$  2-4.2 earthquakes recorded by the Southern Alps Passive Seismic Experiment (SAPSE) over a 6 month period. Long-term seismicity from the NZNSN and Lake Pukaki networks validate our observations over time (8 years versus 6 month), although earthquake locations have a larger error than the SAPSE data. Earthquake analysis indicates changes in deformation at both the northern and southern transition zones and along strike of the Alpine fault.

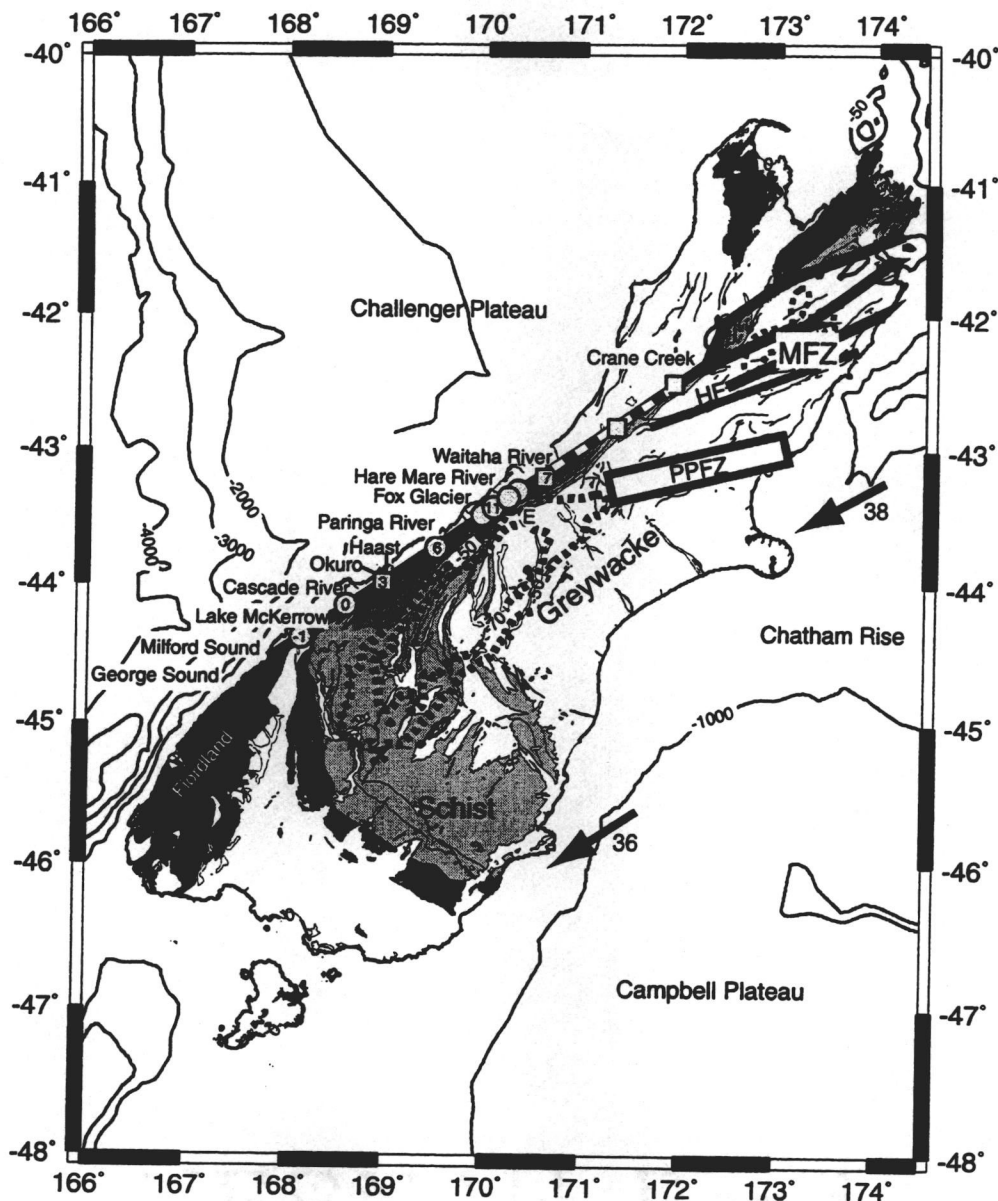


**Figure 3.2** Overview of geology and geologic site locations. The Fiordland block and Dun Mountain Ophiolite belt are shown in black. Schist is marked in grey. Greywacke is the white region bordered by the Alpine fault to the west and Schist to the southwest. Bathymetry contours shown every 1000 meters. Bouguer gravity lows are marked by the dashed lines and are the  $-50$  and  $-70$  mGal contours. Circles and squares mark sites with known uplift rates in mm/year given inside the symbols (Richard Norris, personal communication, 1998). Squares indicate Alpine fault trench sites. Paleoseismic evidence shows single earthquake slips of 8-12 m south of Waitaha. Between Waitaha River and Crane Creek, it is 4-6 m. HF = Hope fault, PPFZ= Porters Pass fault zone, MFZ Marlborough fault zone, E=Elie de Beaumont. Plate motion vectors in mm/year are calculated with the NUVEL 1A rotation pole [DeMets *et al.*, 1994].

### 3.3.1 Seismicity

Seismicity in the region is moderate, and large events have occurred mainly in the regions adjacent to the subduction zones to the north and south (referred to in this paper as transition zones), where focal mechanisms derived from teleseismic body-waveform modeling, are available (Figure 3.1). Eberhart-Phillips [1995] reported about 9 earthquakes of  $M_L$  2.5-3.6 per year on the Alpine fault, using the data from the NZNSN stations from 1991 to 1994. Due to the sparse network, the depth is poorly constrained, and focal mechanisms from this data are not available. Scholz et al. [1974] did a microseismicity survey for several weeks along the Alpine fault. Scholz et al. [1974] recorded events of magnitude 1-3 and derived composite mechanisms for 4 events. Seismicity in the central South Island is confined to the crust [Allis and Shi, 1995; Reyners, 1988; Reyners et al., 1983; Rynn and Scholz, 1978; Scholz et al., 1974], with the exception of a small number of 50-100 km deep earthquakes beneath the Southern Alps [Reyners, 1987]. Here earthquakes outline a westward dipping seismic zone in the upper mantle, parallel in strike to the observed Bouguer gravity low which strike is  $17^\circ$  counterclockwise to the strike of the Alpine fault (Figure 3.2). Our new data set defines the depth of the seismogenic zone throughout the central South Island and provides precise locations and focal mechanisms for tectonic and stress analysis.

### 3.3.2 Alpine Fault

The Alpine fault marks the plate boundary between the Australian and Pacific plates, which are converging obliquely at a rate of about 35.5 mm/year parallel and 10.2 mm/year normal to the fault (37 mm/year relative plate motion at  $43.5^\circ, 170.0^\circ$ , calculated with Nuvel 1A rotation pole [DeMets et al., 1994]). The Alpine fault connects the subduction zones to the north and south, which have opposite facing convergence directions (inset Figure 3.1). From Jackson Bay to the Hope fault intersection, the plate boundary is a continent/continent collision zone with the Challenger plateau to the west

and the Chatham Rise and Campbell Plateau to the east (Figure 3.2). The Alpine fault accommodates half to three quarters of the relative plate motion [Norris and Cooper, 1995; Beavan *et al.*, submitted]. Satellite pictures show the Alpine fault as a clearly defined linear feature from Milford Sound to the northern end of the South Island. On the ground the Alpine fault is seldom clearly defined due to dense vegetation and small-scale surface complexity.

The Alpine fault changes in character along strike (Figure 3.2). From Milford Sound to the Cascade River, the Alpine fault is a steeply dipping strike slip fault with very little dip-slip component [Hull and Berryman, 1986; Sutherland and Norris, 1995]. The thrust component in this region is accommodated by offshore structures and by a wide zone of crustal deformation extending east into Central Otago [Norris *et al.*, 1990]. Farther north it is a moderately eastward dipping oblique thrust fault [Berryman *et al.*, 1992; Norris and Cooper, 1995] with highest uplift rates at Paringa River [Simpson *et al.*, 1993] and between Fox Glacier and Hare Mare River [Cooper and Norris, 1994; Wellman, 1979]. Small-scale segmentation into NW-SE thrust and NE-SW strike slip segments at the surface occurs between about 10 km north of the Haast River and to the Waitaha River (Figure 3.2). This apparent segmentation is believed to be topography controlled, and it is assumed that the faults connect at a depth of a few kilometers [Norris and Cooper, 1995]. The region of highest uplift coincides with a high thermal gradient [Allis and Shi, 1995; Koons, 1987a; Shi *et al.*, 1996]. Thermal modeling [Allis and Shi, 1995; Batt and Braun, 1999; Shi *et al.*, 1996], data from fluid inclusion studies [Craw, 1988; Craw *et al.*, 1994; Holm *et al.*, 1989; Jenkins *et al.*, 1994], zircon reset ages [Tippett and Kamp, 1993] and heat flow measurements [Funnell and Allis, submitted] all indicate elevated temperatures and predict a thermally weakened crust. Allis and Shi [1995] point out that thermal models predict elevated temperatures near the surface, but temperatures below 20 km should be depressed as a result of the building of a crustal root. The estimated brittle/ductile transition zone ranges from 4 to 12 km based on different models. This study provides important new constraints for the brittle/ductile transition zone from precise determination of the earthquake depth.

Paleoseismic evidence along the 600 km long Alpine fault suggests that it has ruptured in large earthquakes ( $M > 7.5$ ) with recurrence intervals of about 200-300 years

[*Bull and Brandon, 1998; Norris and Cooper, 1998; Yetton and Wells, 1998*]. The most recent event is dated at about 1720 [*Norris and Cooper, 1998; Wright et al., 1998; Yetton and Wells, 1998*], therefore a large earthquake on the Alpine fault is likely to occur soon (M. Stirling, personal communication, 1998). Paleoseismic recurrence intervals are shorter in the northern part of the Alpine fault (dashed region of Alpine fault in Figure 3.2) with a slip of 4-5 m per earthquake [*Berryman et al., 1992; Wright et al., 1998; Yetton and Wells, 1998*]. Along the southern part of the Alpine fault, single-event offsets are 8-12 m [*Berryman et al., 1992; Cooper and Norris, 1990*]. The fact that earthquakes in the northern part of the Alpine fault occur more frequently with less single event slip offsets compared to the southern section is possibly related to the occurrence of earthquakes in the Marlborough fault system. Or it may be caused by the possible thermally weakened central section of the Alpine fault, which could form a barrier to southward-propagating earthquakes. This paper investigates if the changes observed along the Alpine fault are reflected by the regional seismic activity and the depth of seismicity.

The Alpine fault north of Jackson Bay does not partition strain as is observed along the San Andreas fault [*Stein and Yeats, 1989; Yeats and Berryman, 1987*], but instead it accommodates both thrust and strike slip component of the relative plate motion along a single fault [*Berryman et al., 1992; Cooper and Norris, 1994; Norris et al., 1990; Simpson et al., 1994*]. Beavan's et al. [submitted] confirm accumulation of oblique plate motion at the Alpine fault based on GPS observations, but they suggest that the normal convergence is higher than that predicted by the plate motion vector. Geodetic data indicate that between 50-70 % of the relative plate motion between the Australian and Pacific plates is accommodated by stable slip on the Alpine fault below 5-8 km [*Beavan et al., 1998; Pearson et al., 1995*]. A further 10-30% of the relative plate motion is accommodated east of the Alpine fault and modeled by Beavan et al.'s [submitted] as stable slip below 30 km.

### 3.3.3 Transition Zones

At the northern end of the South Island, the transition from transpression on the Alpine Fault to westward subduction of the Pacific plate beneath the Australian plate has generated a broad zone of active deformation [Berryman *et al.*, 1992; Lamb and Bibby, 1989; Walcott, 1978]. Northwest of the Alpine fault shortening is accommodated on reverse faults in the Buller region [Rattenbury, 1986]. In the northeast, the Marlborough fault system, a region 100 km wide and 300 km long with active dextral strike slip faults, transfers deformation from the Hikurangi margin subduction zone to the Alpine fault [Van Dissen and Yeats, 1991]. The most active fault of the Marlborough system at present is the Hope fault which intersects the Alpine fault near Arthur's Pass [Beavan *et al.*, 1994; Bourne *et al.*, 1998; Holt and Haines, 1995, Pearson *et al.*, 1995]. Several large earthquakes have occurred on and near the Hope fault since 1881 (summary in [Gledhill *et al.*, submitted]). The 1994  $M_w$  6.7 Arthur's Pass [Abercrombie *et al.*, submitted; Arnadottir *et al.*, 1995; Robinson and McGinty, submitted; Robinson *et al.*, 1994] and 1995  $M_w$  6.2 Cass [Gledhill *et al.*, submitted] earthquakes occurred south of the Hope fault and had a large component of reverse slip in this predominantly strike-slip zone, suggesting complex, diffuse deformation and possible block rotation to accommodate the local stress field at the intersection of the Hope and Alpine fault systems [Robinson and McGinty, submitted; Walcott, 1998]. Southeast of the Hope fault, the incipient Porters Pass fault zone [Cowan *et al.*, 1996] marks the southeastern end of the Marlborough fault system [Carter and Carter, 1982; Herzer and Bradshaw, 1985; Rynn and Scholz, 1978] and possibly intersects the Alpine Fault near Fox Glacier, and coinciding with the segmentation of the Main divide fault zone at Elie de Beaumont [Cox and Findlay, 1995].

At the southern end of the South Island, the change from transform to subduction occurs in Fiordland. The Alpine fault continues offshore at Milford Sound and extends along the western boundary of the Fiordland block where it follows the continental margin as a single structure and splays into an eastern and western branch south of

George Sound. The Alpine fault is seismically active at least as far south as Milford Sound. The north-eastward subducted slab related to the Puysegur subduction zone reaches as far north as Milford Sound. Here the slab is almost vertical at depths greater than 40 km due to collision with the Pacific plate crustal root and underlying lower crustal layer [Smith and Davey, 1984]. The Fiordland subduction zone is defined by seismicity in the down-going slab [Anderson and Webb, 1994] and at least one large earthquake on the thrust surface [Anderson et al., 1993], but lacks the volcanic activity typical for a subduction zone margin. Crustal seismicity is diffuse in this region [Anderson and Webb, 1994; Eberhart-Phillips, 1995] and crustal shortening extends eastward to Central Otago [Yeats, 1987].

### **3.4 Data and Earthquake Locations**

We use four different complementary data sets to evaluate the seismicity in the central South Island (Figure 3.3). The Southern Alps Passive Seismic Experiment (SAPSE) gives unprecedented high-quality earthquake locations and focal mechanisms throughout the central South Island. The New Zealand National Seismic Network (NZNSN) and Lake Pukaki network data provide insight into the long-term seismicity (8 years versus 6 months for SAPSE). Mt Cook earthquakes and aftershocks, recorded by the NZNSN and a temporary aftershock deployment of three stations, outline the tectonics at the southern margin of the Marlborough fault system. The location techniques applied and errors of the final locations are dataset dependent and are outlined below.

#### **3.4.1 Southern Alps Passive Seismic Experiment**

SAPSE was a 6 month temporary seismic experiment recording local, regional and teleseismic earthquakes for various seismic studies from November 1995 to April 1996 [Stern et al., 1997]. SAPSE operated 40 temporary stations which were augmented by 15 permanent national seismic network stations, resulting in an average station distance of

**Figure 3.3** South Island seismicity maps. a) NZNSN (1990-1997) and b) Lake Pukaki network seismicity. Network stations are indicated by squares. c) Station distribution of broadband and short-period instruments of the Southern Alps Passive Seismic Experiment in 1995/1996. During the 6 month deployment, 5491 earthquakes were recorded based on two or more triggers on the short period instruments. Grey stars indicate the location of refraction shots, T1 is the location of the northern transect, T2 the location of the southern transect. White stars mark the location of the Arthur's Pass and Cass earthquakes. d) Station corrections in seconds derived through simultaneous inversion of hypocenter locations and a 1-D velocity model are indicated by the shading of the symbols. See Table 3.1 for details.

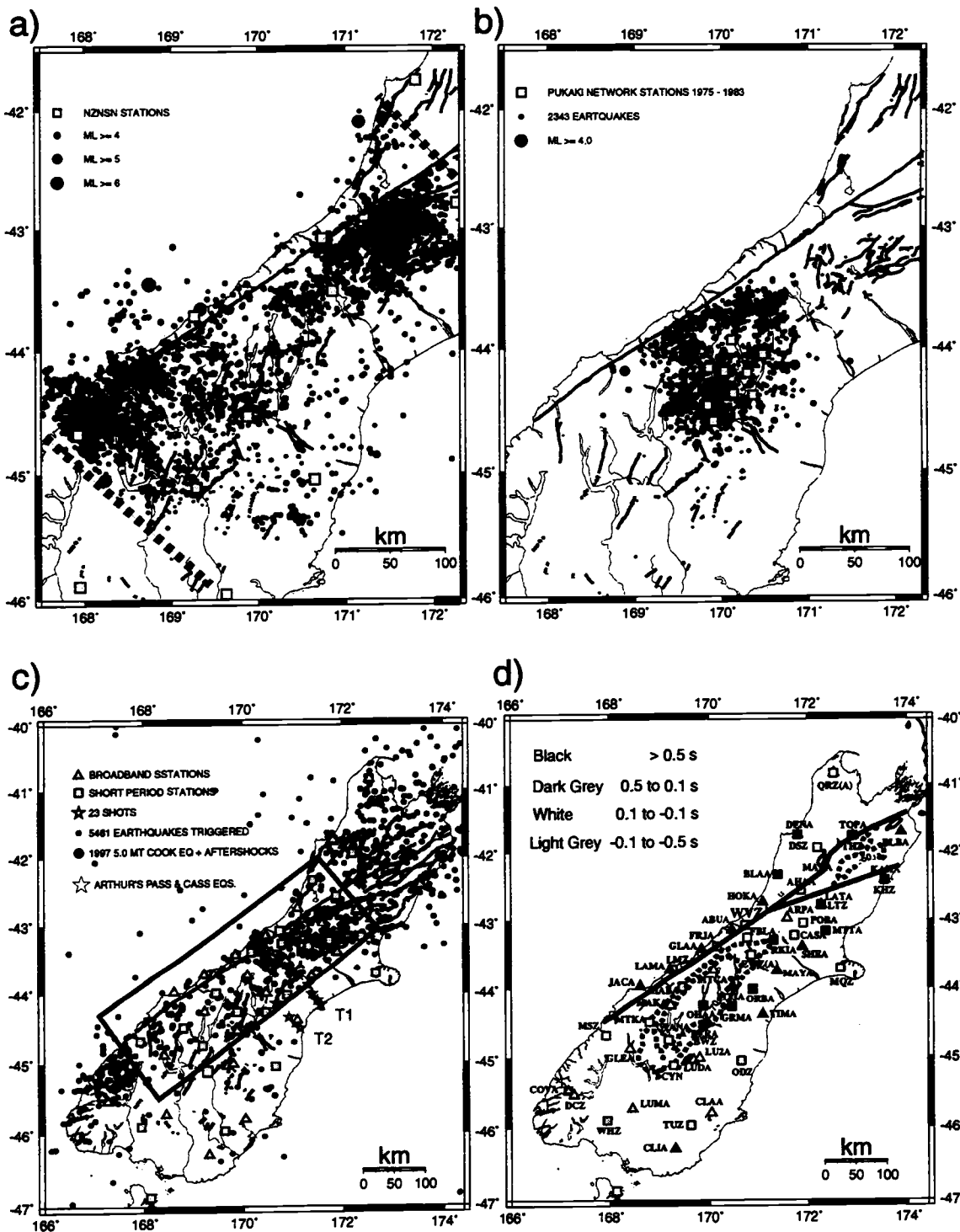


Figure 3.3

30-50 km [Anderson *et al.*, 1997]. The 14 temporary and 15 permanent short period stations (EARSS recorder and 1 Hz, 3 component, L4-C instruments, [Gledhill and Chadwick, 1991]) operated in trigger mode. The 26 temporary broadband stations were equipped with STS2 sensors (except two with CMG-3 instruments at LAMA and GLAA) and Reftek recording units and operated continuously. All earthquakes triggered by 2 or more short period stations were routinely located with HYPOELLIPSE [Lahr, 1992] and the locations of these 5491 earthquakes are shown in Figure 3.3c [Anderson *et al.*, 1997]. Magnitudes given for all earthquakes in this study are derived from the short period stations recordings and are Richter magnitudes corrected for regionally observed characteristics in energy propagation in the same fashion as done routinely for the NZNSN [Haines, 1981]. For 10% of the earthquakes, only a few short period stations detected the event, and no magnitude could be calculated.

230 earthquakes were selected within a 150-km-wide region near the Alpine fault, in the central South Island of New Zealand (black box, Figure 3.3c). In this study, emphasis is given to the long-term regional seismicity, hence aftershocks of the Arthur's Pass and Cass earthquakes are excluded. The tectonic interpretation of these earthquake sequences [Gledhill *et al.*, submitted; Robinson and McGinty, submitted; Robinson *et al.*, 1994] will be summarised together with results of this study. Using the preliminary event origin time, all available broadband station data were extracted and combined with the short-period data in event directories. P and S arrivals and first motion directions were picked on the broadband data and the preexisting picks on the short period data were re-evaluated. The mean characteristics of the data used for the earthquake locations are azimuthal gap  $133^\circ$  (range  $50^\circ$ - $200^\circ$ ), number of picks 16 (range 8-30) and distance to the nearest station 24 km (0-50 km). Single-event locations improved significantly relative to the initial locations based on the short-period station recordings, especially when the azimuthal gap and distance to the nearest station decreased.

### 3.4.2 Joint Hypocenter Determination

We relocated 195 earthquakes by inverting simultaneously for the hypocenter location, a 1-D velocity profile and the station corrections [Crosson, 1976], using the code VELEST [Ellsworth, 1977; Kissling *et al.*, 1994; Krodolf, 1989; Roecker, 1981]. Only events with at least 8 phases and a RMS travel-time misfit smaller than 0.8 s qualified for relocation. This technique improves the single event location by absorbing local changes in the velocity through station corrections. Our data set has a spread of several hundred kilometers over the central South Island, but velocities east of the Alpine fault are fairly homogenous and the calculated station corrections are stable and within reasonable bounds (Figure 3.3d, Table 3.1). Nine well recorded refraction shots (Figure 3.3c) in the study region are used in the inversion and provide test data to estimate the location error. We started the inversion using single event locations and the velocity model of Eberhart-Phillips [1995]. Station elevations were set to the average station height, therefore station delay due to topography is included in our station corrections. We tested different damping values in the inversion, different weights for S picks and the influence of fixing the shots, by comparing the locations of the best resolved earthquakes and shots. For the final inversion we included only S and P picks of quality 2 and higher (scale of 0-4), used an S weighting of 0.8, fixed the shot locations and damped the upper and lower layers of the velocity with 0.1 versus 0.01 for the middle crustal layers. RMS reduction (about 15%) is reached mainly by calculating station corrections, with minor changes of the velocity model. The only significant change between the starting and final velocity model is a thicker upper crust and thinner lower crust (Figure 3.4). The velocity and layer thickness are similar to those derived from the two transect lines. The final locations of the earthquakes are plotted in Figure 3.5.

Table 3.1 Station Corrections. WVZ is the fixed station

Station	Lat (°)	Lon (°)	Elev. (m)	delay (s)
ABUA	43.148	170.463	94	0.8
AHAA	42.569	171.867	215	-0.2
ARPA	42.977	171.579	707	0.1
BERA	44.531	169.884	507	0.3
BWZ	44.532	169.883	490	0.4
BLAA	42.340	171.400	305	0.4
CASA	43.227	171.720	789	0.0
CLAA	45.792	170.044	438	0.0
CLIA	46.293	169.314	359	0.3
CYN	45.149	169.275	1039	-0.1
DCZ	45.468	167.154	50	-0.8
DENA	41.747	171.805	662	0.3
DSZ	41.747	171.803	630	0.0
EWZ (A)	43.512	170.853	620	0.1
FBLA	43.260	170.780	1237	-0.1
FRJA	43.384	170.166	118	0.1
GLAA	43.424	169.848	23	0.7
GLEA	44.875	168.408	463	0.0
GRMA	44.264	170.462	621	0.3
HABA	43.985	169.459	117	-0.2
HOKA	42.743	171.091	236	0.8
JACA	43.971	168.609	50	0.5
KAHA	42.419	173.541	67	0.0
KHZ	42.418	173.540	70	0.4
LAMA	43.723	169.214	110	0.4
LATA	42.783	172.269	636	0.3
LMZ	43.717	169.270	-50	0.0
LTZ	42.783	172.269	640	0.3
LU2A	45.038	169.705	398	-0.1
LUDA	45.035	169.687	385	0.1
LUMA	45.724	168.449	296	-0.4
MAKA	44.252	169.223	336	0.1
MAYA	43.747	171.369	529	0.6
MQZ	43.708	172.652	60	-0.5
MTCA	43.736	170.091	858	0.1
MTJA	43.987	170.465	1042	0.4
MTKA	44.486	168.797	374	-0.1
MTTA	43.165	172.363	880	0.8
ODZ	45.045	170.645	270	-0.2
OHAA	44.255	169.883	688	0.4
POBA	43.047	171.903	524	0.1
QRZ (A)	40.828	172.529	260	0.1
RKIA	43.302	171.310	478	0.2
SHEA	43.393	171.880	448	0.6
THZ	41.764	172.904	760	0.6
TIMA	44.384	171.079	244	0.9
TOPA	41.765	172.905	747	0.6
TUZ	45.956	169.632	110	-0.1
WANA	44.743	169.181	503	0.1
WHZ	45.894	167.947	320	-0.5
MTBA	44.486	168.797	374	-0.2
FOXA	43.490	170.032	240	0.4
AXZ	45.267	169.331	260	-0.5
WVZ	43.076	170.736	75	0.0

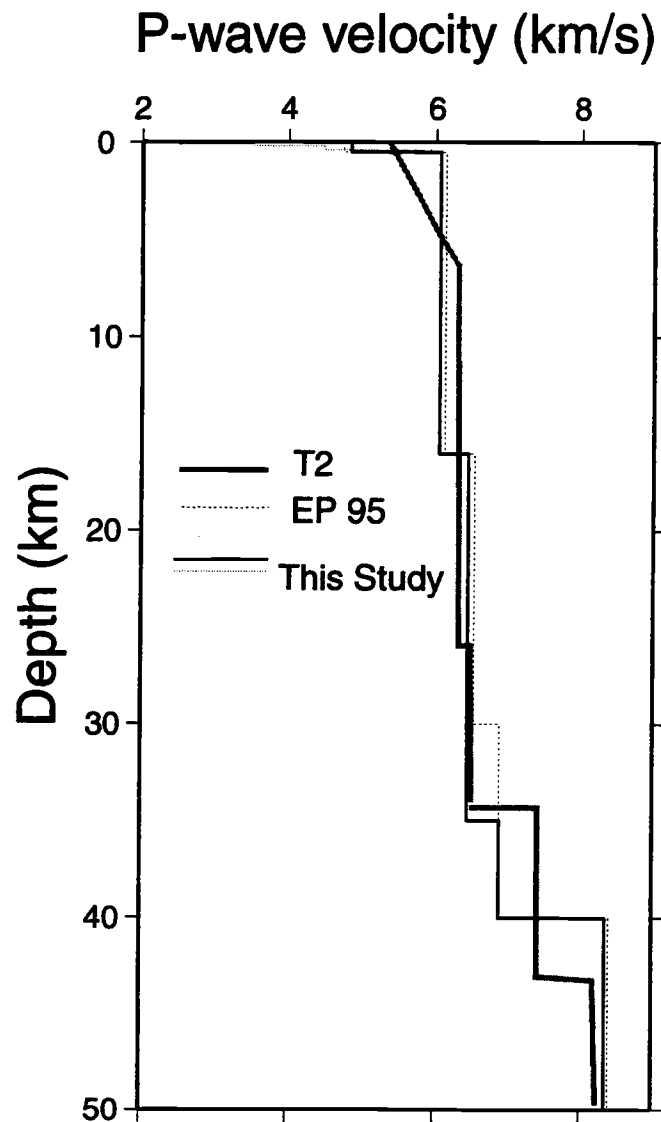


**Figure 3.4** P-velocity models discussed in text. Solid line shows p-wave velocities derived by simultaneous inversion for the hypocenter parameters, station corrections and the velocity model. Dotted line is the velocity model used to calculate the amplitude ratios and has low velocity layers at the surface. Dashed line is from Eberhart-Phillips [1995] and was used as a starting model. Thick grey line is the velocity model at 45 km distance from the Alpine fault on transect 2 [Kleffmann *et al.*, 1998b].

**Figure 3.5** a) Histograms showing magnitude and depth of earthquakes recorded with SAPSE. Depth distribution is for earthquake depth < 30 km illustrating that most earthquakes occur at depths shallower than 10-12 km. b) Location of SAPSE earthquakes relocated by Joint Hypocenter inversion using P and S wave picks of the short period and broadband stations. Nine shots marked as white diamonds, were used to relocate and test the earthquake relocations. Shape of symbol marks the depth error, and color indicates the depth range as shown in the legend. Stars mark earthquakes deeper than 30 km. Grey shades mark the maximum depth of the seismogenic zone outlined by SAPSE, Pukaki and NZNSN network seismicity. Light grey region marks 10-12 km depth to base of the seismogenic zone. Regions in medium grey indicate a shallower seismogenic zone with 5-10 km depth. Dark grey region had almost no earthquakes during SAPSE, NZNSN and Pukaki network operations. Lines show position of cross sections shown in Figure 3.13. MS Milford Sound; HF Hope fault.

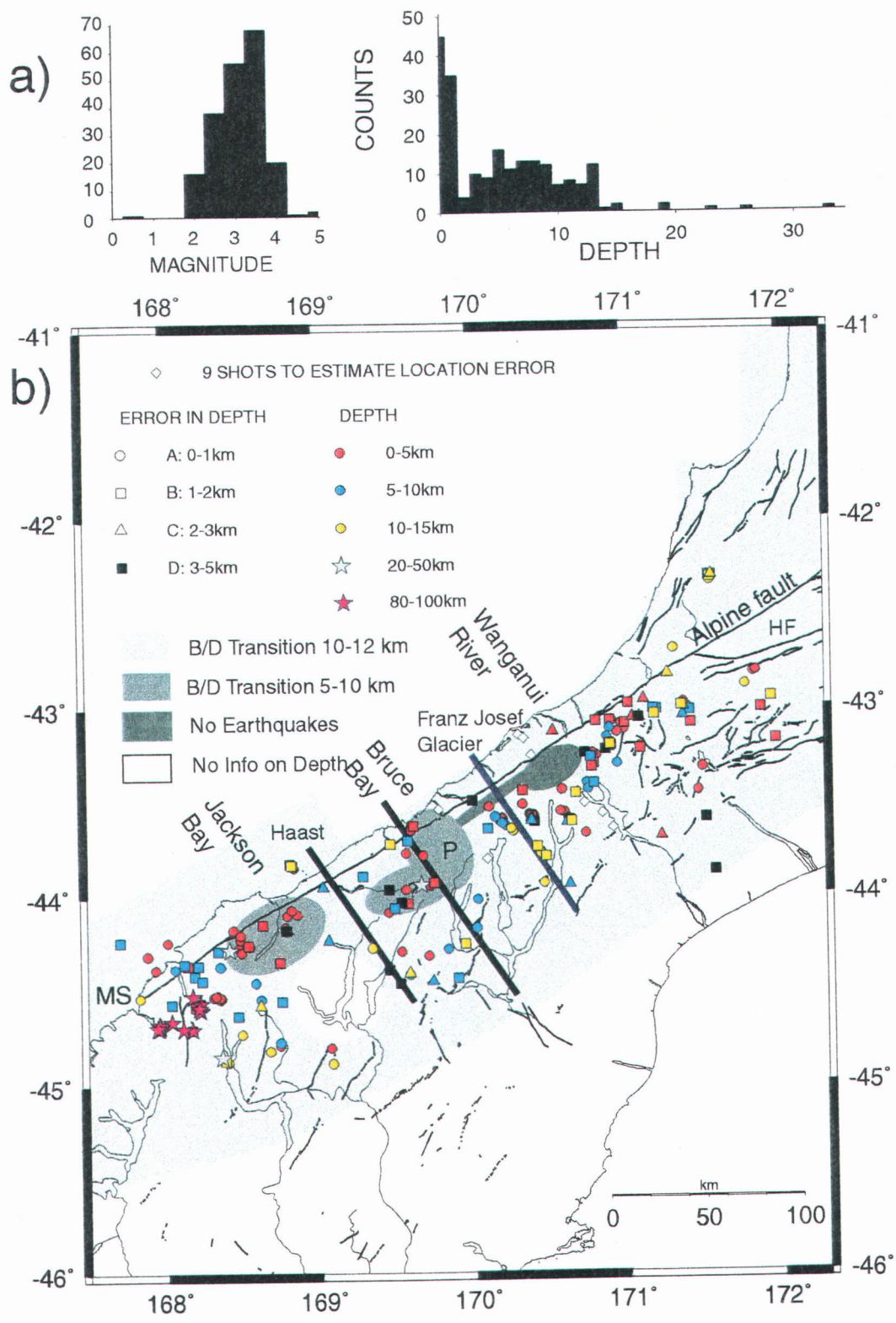


Figure 3.5

Our station corrections are the sum of travel time differences due to velocity heterogeneities at the site and topography. The station corrections (Figure 3.3d and Table 3.1) are nearly zero east of the Alpine fault in the general area of thick crust, as reflected by the extent of the Bouguer gravity low (Figure 3.2). Large positive delays at the West Coast and within the Canterbury basin are caused by thick sediment layers at the surface [Kleffman *et al.*, 1998b; Stern *et al.*, 1997]. The velocity model (Figure 3.4) should not be interpreted too literally in representing a crustal profile because it does not account for 2-D and 3-D velocity variations. Our velocity in the upper crust is 6.0 km/s compared to 6.2 km/s [Kleffmann *et al.*, 1998b] and 5.8-6.2 km/s [Holbrook *et al.*, 1998] derived from travel time inversion along the two seismic transects. Figure 3.4 shows that the velocity model derived in this study is very similar down to 30 km depth to that of Eberhart-Phillips [1995] and Kleffmanns *et al.* [1998b] velocity model positioned at 45 km east of the Alpine fault.

The location error of the data set was evaluated in two ways. First shots and earthquakes were relocated. The distance between the true and calculated location of the 9 refraction shots within our study region is given in Table 3.2. The location error is smaller than 2 km for all except the 2 shots near the West Coast, where the azimuthal gap of 150° results in a trade off between the epicenter location and depth, resulting in an error of 5 km. No S arrivals were used to calculate the shot locations, therefore the location error of a shot will be larger than one for an earthquake with the same P arrival picks.

The location error was estimated in a second way. For each earthquake the maximum distance and depth difference to the final location between different inversion runs was calculated. Twenty separate inversion runs testing different velocity models, S pick weighting and damping values for the velocity layers and hypocenter parameter were run. The usefulness of this calculation was verified by calculating the relative errors for the shots, using runs without fixed shots. The average location error in depth is 1.5 km. About 90% of the data have a depth error of less than 3 km (Table 3.3). The depth error for each earthquake location was assigned 1 of 4 qualities A-D and is marked by different symbols in Figure 3.5.

Table 3.2 Location Error of Refraction Shots

YYMMDD	HHMM	S (s)	Lat (°)	Lon (°)	Depth (km)	D-EPI	M <sub>L</sub>	Gap (°)	RMS s	M-DIST km	# Picks
960116	1000	3.69	43.80	170.10	0.5	0.1	4.0	57	0.31	7	19
960116	1100	5.68	43.54	169.79	0.1	1.0	3.6	135	0.34	13	29
960127	1000	4.51	43.51	170.74	0.1	1.7	3.6	70	0.33	9	18
960127	1100	2.01	43.64	170.92	1.7	2.1	3.5	79	0.43	16	21
960127	1200	1.26	43.14	170.31	4.6	2.1	N/A	169	0.46	12	28
960127	1300	0.97	43.16	170.35	7.0	3.4	3.5	162	0.77	10	26
960127	1400	2.81	43.45	170.70	0.1	1.7	3.5	79	0.27	14	14
960127	1430	0.72	43.25	170.40	1.1	0.5	3.5	144	0.15	13	14
960128	1000	4.80	43.57	170.85	1.4	1.1	3.6	81	0.45	6	19

Time and location of the refraction shots. The depth is derived by relocating the shots by simultaneous inverting for the hypocenter parameters, station corrections and a 1-D velocity model. D-Epi is the distance between the true and calculated epicenter. M-DIST = distance to closest recording station.

Table 3.3 Depth Quality of SAPSE and Mt Cook Earthquakes

Quality	Depth error (km)	# of Earthquakes	% of Earthquakes
A	0-1	103	53
B	1-2	66	66
C	2-3	23	23
D	3-5	20	20

Depth error = (maximum depth-minimum depth)/2

### 3.4.3 New Zealand National Seismic Network

Seismicity recorded by the NZNSN over the period 1990-1997 provides long term seismicity of comparable magnitude to the SAPSE data but larger uncertainties of the hypocenter parameters due to an average station distance of about 100 km (Figure 3.3a). Depth are only reliable when the nearest station is within 25 km of the epicenter, which applies to only a small percentage of the data set. Of the 15800 earthquakes recorded during this 8 year period, over half are aftershocks of the 1994  $M_w$  6.7 Arthur's Pass earthquake [Robinson *et al.*, 1994].

We improve the locations by relocating the earthquakes using the 1-D velocity model and station corrections derived from the inversion of the SAPSE data. We thereby redo Eberhart-Phillips [1995] study, and include the now available 8 year data set. To compare the data to the SAPSE data, the following selection criteria were applied: RMS travel time misfit  $< 0.8$  s, at least 8 phase data, azimuthal gap  $< 200^\circ$  and a minimum distance of 50 km to the nearest station. There is a tradeoff between tightening the quality parameters and the spatial distribution of data coverage. We chose a data set which reveals the seismic patterns and has acceptable quality parameters. It is necessary to verify that seismic patterns are not caused by the selection criteria and are apparent in both the raw and selected data. Note that the offshore seismicity south of Bruce Bay is real and excluded by the selection criteria.

### 3.4.4 Lake Pukaki Network

The Lake Pukaki network provides quality earthquake locations (Figure 3.3b) for the time between 1975-1983 [Haines *et al.*, 1979]. The network monitored the seismicity during impounding of Lake Pukaki during 1976-1979 [Reyners, 1988]. Due to the dense station distribution near Lake Pukaki (about 30 km average station distance) 2660 earthquakes were recorded, complete from about magnitude 1.8 upwards, providing good depth resolution within 25 km of the nearest station. The errors in depth and hypocenter

parameters are estimated to 3-5 km [Reyners, 1988]. The Lake Pukaki network complements the SAPSE data in a low seismicity region and provides insight into the seismicity at a lower magnitude threshold. The hypocenter parameter errors are comparable to those of the SAPSE data, but are dependent on the distance to the network stations. We selected earthquakes with RMS travel time  $< 0.8$  s, at least 8 arrival picks and magnitude  $> 1.8$  (1260 earthquakes).

#### 3.4.5 1997 Mt Cook Earthquake and Aftershocks

The Mt Cook earthquake sequence occurred in September 1997 and included 2  $M_L$  5.0 main shocks followed by 8 aftershocks. The first 6 earthquakes were recorded by the NZNSN, and the locations are not well constrained. A temporary network of 3 short period EARSS stations was deployed on October 22, reoccupying the two SAPSE sites GLAA and MTCA and an additional new site at FOXA. This earthquake sequence is of special interest to us because of its size and proximity to the Alpine fault. Events recorded by the temporary stations have good quality locations and focal mechanisms.

### **3.5 Focal Mechanisms**

Earthquakes used in this study have magnitudes ranging from about  $M_L$  2 to 4.2. The network spacing is too sparse to calculate focal mechanisms using first-motion polarity observations. Schwartz [1995] showed that matching amplitude ratios of P/SV, P/SH and P/SV waves is a fast and robust method to calculate focal mechanisms using sparse three component networks. The focal mechanisms were stable for a wide range of crustal models, earthquake locations and depths. Amplitude ratios have been used in several studies [Julian and Foulger, 1996; Kisslinger, 1980; Rognvaldson and Slunga, 1993; Snoke *et al.*, 1984] and have the advantage that path effects, attenuation and instrument response are eliminated or much reduced, so that changes in S/P ratios reflect changes in source orientation. The amplitude ratio technique can be used at frequencies higher than 1 Hz, where the energy is concentrated for earthquakes smaller than magnitude 4.

We apply a combined first motion and amplitude ratio technique to our data set. This has the advantage of utilizing both types of information and is important because first motion or amplitude ratios alone do not constrain the mechanisms tightly. The technique is an excellent tool for the moderate sized earthquakes in the study region.

Three component waveform modeling is sensitive to the earth structure and [Dreger and Helmberger, 1993; Fan and Wallace, 1991; Nabelek and Xia, 1995; Ritsema and Lay, 1993] is performed at much lower frequencies (less than 0.1 Hz) where the earth's structure can be satisfactorily approximated. In our data set the signal to noise ratio limits waveform modeling to earthquakes with magnitude  $M_w$  3.9 ( $\sim 4.1 M_L$ ) and higher. The moment tensor solutions of the  $M_w$  6.2 Cass earthquake, 3 of its largest aftershocks and one event of our data set were calculated using the code of Nabelek and Xia [1995]. For three events both techniques yielded mechanisms and their results can be compared.

### 3.5.1 Amplitude Ratio and First Motion Method

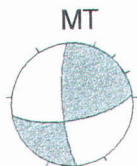
We apply a first motion and amplitude technique [Robinson and Webb, 1996], which searches for the double couple mechanisms which best fits all chosen amplitude ratios [technique after Schwartz, 1995] and satisfies the maximum possible number of first motion observations. This technique has provided excellent results with aftershock and temporary deployments of short period EARSS instruments [Gledhill et al., submitted; Reyners and McGinty, 1999; Reyners et al., 1997; Robinson et al., 1994]. The selected frequency band (1-4 Hz), maximum distance of calculated synthetics (75 km) and use of all amplitude ratios gave good results throughout New Zealand [Gledhill et al., submitted; Reyners and McGinty, 1999; Reyners et al., 1997; Robinson et al., 1994] and was adapted for our study.

The envelopes of complete theoretical seismograms [Herrmann, 1991] are calculated and the maximum values within 1.5 s of the P and S arrivals are automatically picked and, if necessary, modified by hand. When several phases arrive within the pick window, the user needs to narrow the window on a distinct arrival (e.g. station JACA in Figure 3.6b). The method searches for the mechanisms which best fits all 7 log amplitude ratios

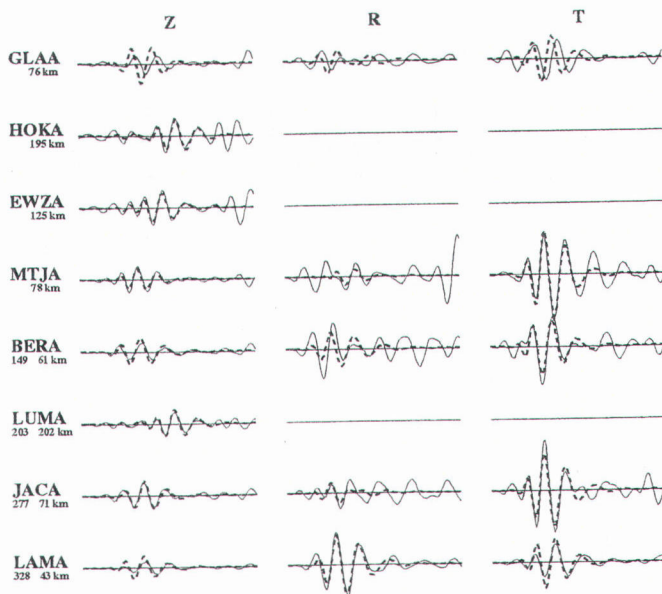
**Figure 3.6** a) Synthetic (dashed line) and observed (solid line) seismograms for 960124.174426. The full waveform inversion was performed in the 14-25s pass-band. Z, R and T are vertical, radial and transverse component for each modeled station. Station name, azimuth and epicentral distance are listed to the left of the vertical trace. Beachball on left shows best fitting solution derived by the waveform inversion and azimuthal distribution of the stations plotted. Seismogram amplitudes are normalized to 100 km distance assuming cylindrical spreading. A strike-slip solution is obtained which is similar to the best fitting mechanism derived by the first motion and amplitude ratio technique. b) Synthetic (black) and observed (red) seismograms for 960124.174426. The amplitude ratio technique was performed in the 1-4 Hz pass-band for the mechanisms of the best amplitude ratio fit shown at the top left. Z, R and T are vertical, radial and transverse components of the stations. Plotted are the envelope functions of synthetic and observed data normalised by the maximum amplitude for each station. For this plot (not for the calculation of mechanism) synthetics are calculated to nearest 5 km which causes a slight offset between observed and synthetic seismograms for some stations. Station name, azimuth and epicentral distance are at start of the Z component. A star marks stations that were used in the amplitude ratio technique. On the left hand side the two outputs from the first motion amplitude technique are; top: P (pluses) and T (open circles) axes which fit all first motions in grey, and P and T (both crosses) axes which best fit the amplitude ratios are marked in black. bottom: the focal mechanisms that best fits first motion and amplitude ratios. The first motions are marked by circles where black is compressional and grey indicate dilatational first motion.

a)

960124.174426  
Mw=3.87 14-25s 6km



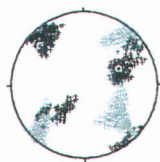
0 100  
Time (s)  
maximum amplitude: 0.8 μm



b)



FMO=17 AMP=6



FMO+AMP

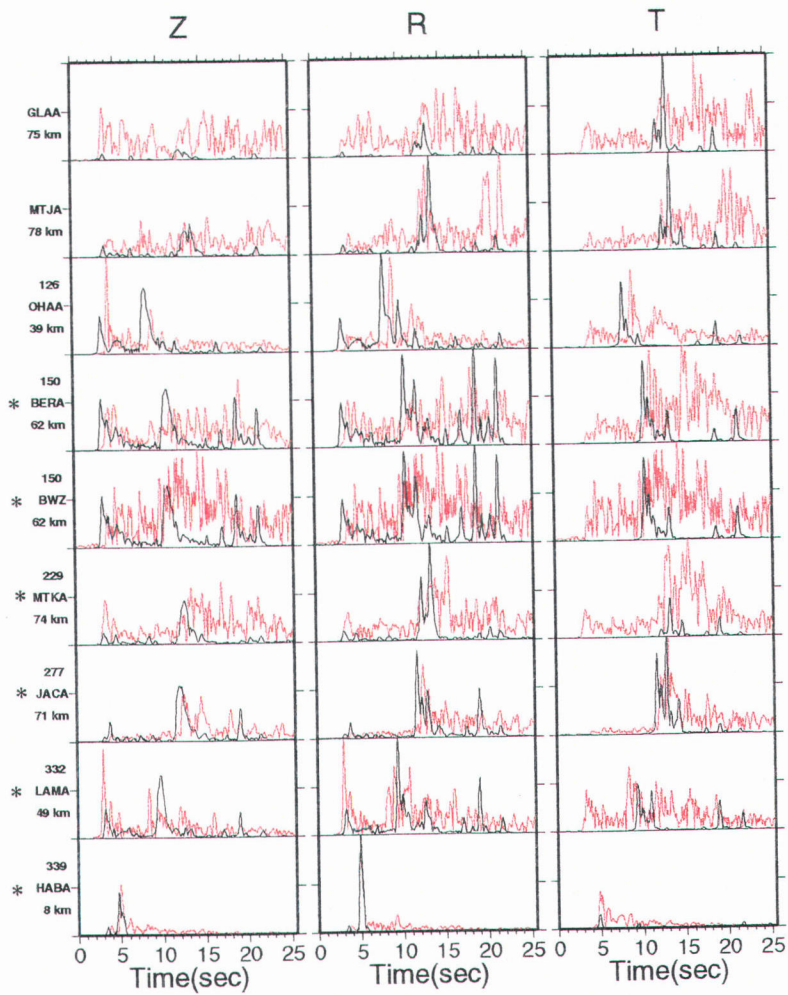


Figure 3.6

(PZ/SZ, PZ/SR, PZ/ST, PR/SR, PR/SZ, PR/ST, SR/ST) of observed and synthetic data (example in Figure 3.6b). The final hypocenter parameters and velocity model from the simultaneous hypocenter inversion are used in the calculation. Three low velocity surface layers were added to simulate scattering and attenuation of seismic waves expected near the surface and to steepen the ray path (e.g. [Abercombie, 1997]). Refracted arrivals from the lower crust arrive at distances of about 150 km and can complicate the waveforms. Hence, we did not use stations at this distance range for amplitudes or first motions calculations.

The operation of the technique is best described by examples of the program shown in Figures 3.7 and 3.8. All mechanisms shown in this paper are equal area projections of the lower hemisphere. The plot to the left (see Figure 3.6b left hand side, Figure 3.7, Figure 3.8, Figures 3.10a and 3.10b right hand side) shows all possible P (pluses) and T (open circles) axes of focal mechanisms which either fit the maximum amount of first motions (grey) or fit the amplitude ratios within a given error limit. All included amplitude ratios have a standard error more than 2 standard deviations below the mean error. Only clear first motions should be included, since the best solution will try to satisfy all first motions. Mechanisms are determined by stepping through strike, dip and rake in 7.5° increments. To the right we see all P and T axes which are common to the first motion and amplitude ratio methods shown in the plot to the left. In addition first motions are plotted, where solid circles are compressions and grey circles are dilatations. The best mechanism shown in the right diagram has the lowest amplitude ratio error and the lowest number of first motion errors (e.g. fits all first motions if possible). The spread of P and T axes in the plot to the right shows the error bounds of the best mechanism. Error calculation of strike, dip and rake is only appropriate when P and T axis are tightly clustered around the best fitting P and T axes (Figures 3.7a, 3.7c, 3.8a and 3.8c).

We apply the method to seismograms recorded by broadband and short-period recorders and thereby modified the code slightly. On average we have fewer first motion and amplitude ratio observations than in previous investigations. To test the robustness of the method, we selected events with good coverage and tested that the solution was recoverable with fewer observations. For example, event 960328.164047 is well constrained by 14 first motions and 8 amplitude ratios (Figure 3.7a). The two focal

960328.164047 -43.6022 170.6530 Depth=10.84 ML=3.4

S,D,R= 337.5 67.5 -22.5

S,D,R= 76.5 69.3 204.1

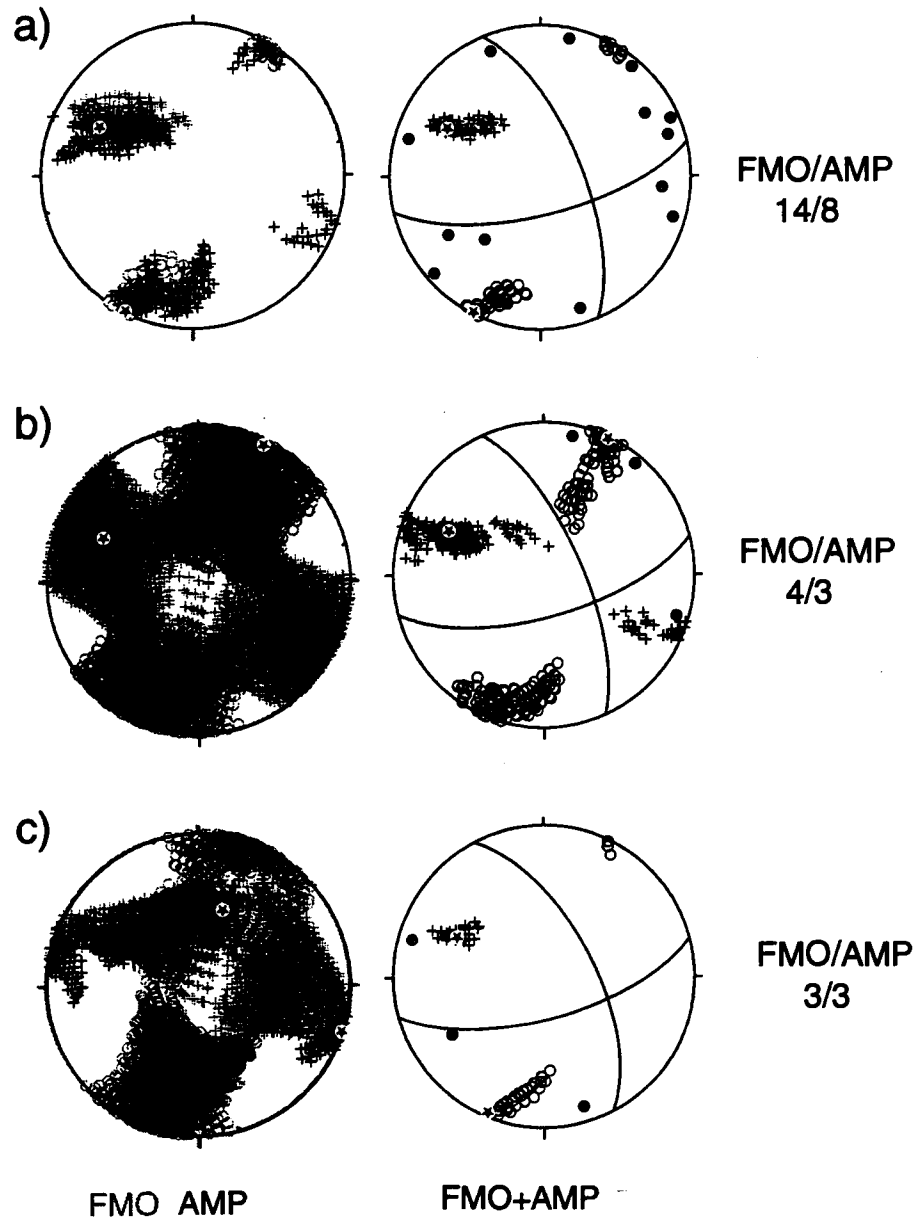


**Figure 3.7** Example earthquake 960328.164027 shows robustness of method by similarity of the calculated focal mechanisms using a) all available observations b) 3/4 c) 3/3 first motion/amplitude ratio observations. At the left are plotted P (pluses) and T (open circles) axes which fit all first motions in grey, and P and T (crosses) axes which best fit the amplitude ratios are marked in black. To the right is the focal mechanisms which best fits first motion and amplitude ratios. First motions are marked by circles where black is compressional and grey is dilatational first motion.

mechanisms calculated with only 4 (Figure 3.7b) and 3 (Figure 3.7c) first motions and 3 amplitude ratios vary only  $7.5^\circ$  (the increment of the grid search technique) from the strike, dip and rake of the well constrained solution. No mechanism in this paper was calculated with less than the above tested observations.

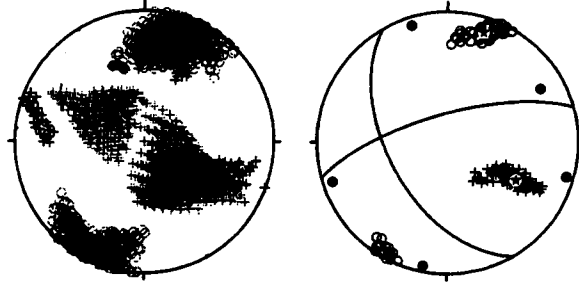
In addition we selected only the most reliable results by introducing quality selection criteria. All mechanisms selected in this study have a good correlation (correlation coefficient  $> 0.7$  on a scale from 0-1) between synthetic and observed log amplitude ratios for the best fitting mechanism (Table 3.4). Mechanisms with on average 9 first motion observations and 6 amplitudes have A quality, when the P and T axes within the given error cluster tightly around the best solution (Figures 3.7a and 3.8a). Mechanisms which are constrained by on average 5 first motions and 4 amplitudes have C quality, when all mechanisms within the given misfit cluster tightly around the best solution (Figure 3.8c). Often, despite a satisfying amount of first motions and amplitudes, mechanisms can have several possible solutions with large differences between the P and T axis within the given misfit (Figures 3.8b and 3.8d). This reduces the quality of the solution unless other a priori information can select a single mechanism. We downweighted those mechanisms from A to B and C to D respectively. Frequently the first motion and amplitude mechanisms can not distinguish between the  $180^\circ$  rotated solutions of dip slip fault mechanisms (Figure 3.8b).

Table 3.4 Quality of Focal Mechanisms

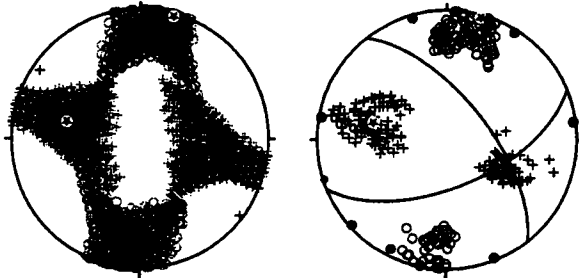
Quality	S/D/R Error ( $^\circ$ )	# of Eqs	% of Eqs	Selection Criteria
A	15/15/30	28	21	mean # FMO/A 9/6 RMS $<  \text{mean} - 2\text{sdv} $
B	Two or more mechanisms possible	21	16	mean FMO/A 9/6 RMS $<  \text{mean} - 2\text{sdv} $
C	20/20/30	25	19	mean # FMO/A 5/4 RMS $<  \text{mean} - 2\text{sdv} $
D	Two or more mechanisms possible	35	27	mean # FMO/A 5/4 RMS $<  \text{mean} - 2\text{sdv} $

**Figure 3.8** Examples of first motion and amplitude ratio method for earthquakes with A-D quality (quality criteria are summarised in Table 3.4). For each event the focal mechanism is shown in lower hemisphere projection. To the left, grey P (pluses) and T (circles) axis of focal mechanisms satisfy the maximum amount of first motions and black P and T axis of the focal mechanisms which best fit the amplitude ratios (RMS error more than two standard deviations below the mean error) are shown in an equal area projection. To the right: P and T axes which satisfy amplitude and first motion criteria and first motions projected on best fitting mechanism where black circles present compressional and grey circles present dilatational first motions. a) A quality, b) B quality, c) C quality and d) D quality.

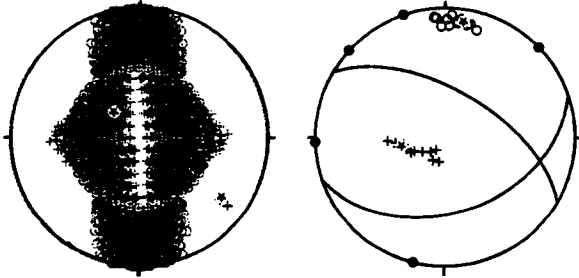
a) 950328.170309 -43.3990 170.6487 S,D,R= 330.0 52.5 -22.5  
 Depth 6.72 ML=3.5 FMO/A 6/7 S,D,R= 74.2 72.3 219.7



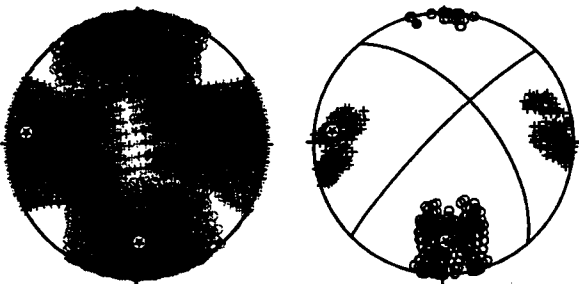
b) 960222.005550 -43.6698 170.7435 S,D,R= 67.5 60.0-150.0  
 Depth 3.5 ML=2.2 FMO/A 9/7 S,D,R= 321.4 64.3 326.3



c) 960320.210747 -43.5285 170.1152 S,D,R= 300.0 60.0 -60.0  
 Depth 0.5 ML=3.1 FMO/A 5/3 S,D,R= 70.9 41.4 229.1



d) 951231.085520 -43.3162 170.7885 S,D,R= 225.0 82.5 150.0  
 Depth=0.5 ML=3.7 FMO/A 4/4 S,D,R= -40.7 60.3 8.6



FMO AMP

FMO+AMP

Figure 3.8

Table 3.5 Focal Mechanisms of A and C Quality Events

Q	YYMMDD.HHMMSS	Lat (°)	Lon (°)	Strike Dip	Rake	Strike Dip	Rake
A	951116.125029	-44.5465	168.7637	127.5 82.5	-30.0	221.8 60.3	188.6
C	951118.214349	-44.5130	168.1897	97.5 37.5	105.0	-101.2 54.0	78.8
A	951119.020252	-43.6075	170.6252	330.0 60.0	-22.5	71.7 70.6	212.0
A	951122.011148	-44.1705	168.7947	360.0 37.5	-15.0	102.0 80.9	233.5
A	951122.135212	-44.1678	168.7972	352.5 67.5	-37.5	98.9 55.8	207.6
C	951123.042743	-44.0917	168.8002	52.5 75.0	-142.5	311.3 54.0	341.3
C	951204.115359	-43.9562	169.5728	255.0 37.5	157.5	3.2 76.5	54.7
C	951209.143322	-42.3015	171.5728	352.5 45.0	-157.5	246.2 74.3	312.7
A	951209.223000	-43.4885	170.0057	262.5 52.5	127.5	30.9 51.0	51.6
A	951210.172357	-42.8205	171.8392	255.0 75.0	150.0	-6.5 61.1	17.2
A	951211.132138	-42.8248	171.2878	360.0 67.5	15.0	-95.9 76.2	156.8
C	951213.091016	-43.5910	170.3977	210.0 45.0	-120.0	69.2 52.2	296.6
A	951217.164153	-43.5910	171.5255	247.5 22.5	112.5	43.4 69.3	81.0
A	951222.201507	-43.5975	170.3928	217.5 37.5	-120.0	73.5 58.2	291.0
C	951228.104058	-43.3002	170.7995	7.5 67.5	-37.5	113.9 55.8	207.6
C	951228.105932	-43.2643	170.7837	82.5 82.5	112.5	-170.0 23.7	19.0
A	960102.190535	-42.9918	171.3697	285.0 45.0	-135.0	159.7 60.0	305.3
A	960104.094241	-43.2580	170.8192	90.0 75.0	-142.5	348.8 54.0	341.3
C	960104.100937	-44.3082	169.7152	15.0 30.0	52.5	-123.5 66.6	109.4
C	960105.233536	-44.4020	169.5932	345.0 37.5	52.5	-151.0 61.1	115.0
A	960106.221616	-43.7048	169.5855	97.5 60.0	-142.5	346.5 58.2	324.0
C	960107.134014	-43.3230	171.5058	97.5 52.5	-157.5	353.3 72.3	320.3
A	960113.201106	-44.1687	168.7993	360.0 30.0	-15.0	103.1 82.6	240.9
A	960115.135309	-43.2253	170.8807	67.5 45.0	172.5	162.8 84.7	45.2
A	960124.174426	-44.0507	169.4927	360.0 82.5	-22.5	93.1 67.7	188.1
C	960126.060919	-43.0120	171.2122	82.5 75.0	135.0	-173.0 46.9	20.8
A	960128.010500	-44.5570	168.2488	232.5 45.0	165.0	-26.8 79.5	46.0
A	960130.005333	-43.4360	170.7607	15.0 52.5	7.5	-79.6 84.1	142.3
A	960330.012342	-43.5992	170.6373	337.5 75.0	-37.5	78.7 54.0	198.7
C	960131.021014	-43.5950	170.2025	37.5 67.5	105.0	-177.5 26.8	58.0
C	960209.134021	-44.5352	168.6242	352.5 82.5	37.5	-103.2 52.9	170.6
A	960211.234027	-43.5590	170.6040	225.0 37.5	165.0	-33.0 80.9	53.5
A	960220.043251	-43.3032	170.9513	180.0 82.5	-60.0	282.7 30.8	194.8
C	960222.124201	-44.2507	168.5455	112.5 37.5	-22.5	220.7 76.5	234.7
C	960223.102038	-44.3507	168.1423	30.0 37.5	82.5	-140.6 52.9	95.7
A	960226.135139	-43.1775	171.9818	360.0 60.0	22.5	-101.7 70.6	148.0
A	960304.100642	-44.4453	168.5937	157.5 75.0	-37.5	258.7 54.0	198.7
C	960304.105643	-44.5715	168.2017	180.0 60.0	-135.0	63.4 52.2	320.8
C	960305.195022	-44.7658	168.7532	352.5 82.5	-52.5	92.2 38.1	192.2
A	960309.042412	-43.4540	170.6782	135.0 45.0	-45.0	260.3 60.0	234.7
C	960309.063353	-44.2260	169.0638	97.5 52.5	-105.0	301.3 40.0	288.6
A	960312.194612	-44.2833	169.5417	150.0 52.5	-15.0	249.3 78.2	218.5
C	960313.071440	-44.5897	168.2132	45.0 30.0	172.5	141.5 86.3	60.2
C	960316.032440	-44.5612	168.0440	90.0 45.0	90.0	-90.0 45.0	90.0
C	960319.095902	-42.3092	171.5615	285.0 52.5	105.0	81.2 40.0	71.4
A	960319.142120	-44.5718	168.6262	142.5 52.5	-30.0	251.9 66.6	221.5
C	960319.164120	-44.8130	168.6788	330.0 60.0	37.5	-141.0 58.2	144.0
C	960319.184804	-44.1650	168.4535	60.0 82.5	135.0	157.4 45.5	10.5
C	960320.210747	-43.5285	170.1152	300.0 60.0	-60.0	70.9 41.4	229.1
A	960328.164047	-43.6022	170.6530	337.5 67.5	-22.5	76.5 69.3	204.1
A	960328.170309	-43.5990	170.6487	75.0 67.5	-142.5	328.6 55.8	332.4
A	960330.012342	-43.5992	170.6373	337.5 75.0	-37.5	78.7 54.0	198.7
A	960402.004126	-43.9458	169.0297	82.5 75.0	127.5	-168.9 40.0	23.8
A	960406.152047	-43.2417	170.7450	172.5 60.0	-45.0	289.1 52.2	219.2
C	970923.021014	-43.5950	170.2025	37.5 67.5	105.0	-177.5 26.8	58.0

Only quality A and C events (Table 3.5) can be used directly for stress inversion or be plotted as focal mechanisms. Quality B and D events have an ambiguity between different focal mechanisms, and are only useful when other a priori information can distinguish between them. Therefore we will only show these mechanisms when they are of particular interest and care must be taken with their interpretation.

The focal mechanisms of our data set are dominated by thrust and oblique strike slip mechanisms (Figure 3.9c and Figure 3.11c). The P axes lie between  $90^{\circ}$ - $160^{\circ}$  of the stereonet projection (Figure 3.9a and 3.9d) and reflect the observed maximum horizontal strain of about  $110^{\circ}$  [Pearson *et al.*, 1995]. South of Jackson Bay, the 4 available focal mechanisms of large earthquakes have P axes of about  $140^{\circ}$  (Figure 3.9e). In contrast, P axes from the smaller earthquakes fall between  $90^{\circ}$  and  $180^{\circ}$  (Figure 3.9d). It is not clear if the discrepancy is biased by sparse spatial sampling of the large earthquakes or if indeed the smaller earthquakes are caused by a different stress field. North of Jackson Bay large and small earthquakes have similar mechanisms (Figure 3.9a and 3.9b) and P and T axes respond to the same stress field.

**Figure 3.9** Stereonet projection of P and T axes. a) P and T axes for  $M_L$  2-4.2 earthquakes north of Jackson Bay. b) P and T axes for  $M_w > 5.4$  earthquakes (see also Figure 3.1) north of the dashed line near Jackson Bay. c) Lower hemisphere projection of A quality (compressional quadrant in black) and C quality (compressional quadrant in dark grey) mechanisms derived with the first motion and amplitude ratio method. Lower hemisphere projections of large earthquakes have light grey compressional quadrants in (reference see Figure 3.1). d) P and T axes for  $M_L$  2-4.2 earthquakes south of Jackson Bay. e) P and T axes for  $M_w > 5.4$  earthquakes (see also Figure 3.1) south of Jackson Bay.

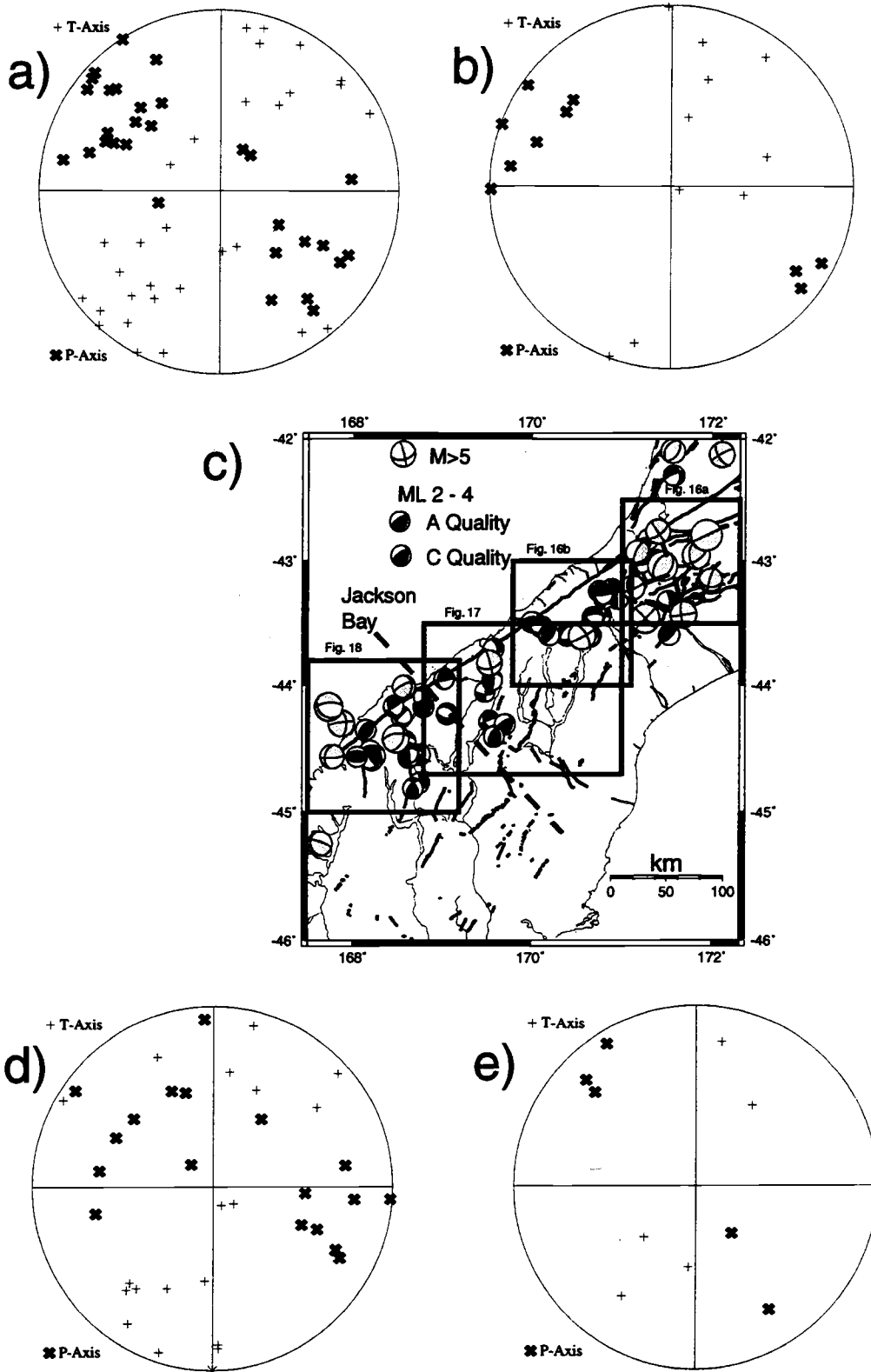


Figure 3.9

### 3.5.2 Moment Tensor Inversion

We invert the seismograms of the SAPSE broadband stations to obtain the seismic moment tensor, the source time function and the centroid depth. The least square inversion fits synthetic seismograms calculated with the velocity model obtained in this study (Figure 3.4) with observed three component seismograms at frequencies lower than 0.1 Hz. The frequency band is adjusted according to the signal to noise ratio for each event, 0.07 – 0.03 Hz for the events  $< M_L$  5 and 0.04 – 0.02 for the earthquakes  $> M_L$  5. We use all available broadband recordings, i.e. 4-7 stations at distances of 50-300 km and good azimuthal spread, which gives well constrained mechanisms. An example of the waveform fit for the 960124\_1744 is shown in Figure 3.6a. The technique is described in Nabelek and Xia [1995] and is routinely used for regional moment tensor inversions using permanent broadband network stations in the Pacific Northwest (OSU web page <http://quakes.oce.orst.moment-tensors>). We expect that the temporary stations have a lower signal to noise ratio [Braunmiller *et al.*, 1995] and therefore the magnitude threshold of earthquakes is higher than expected for permanent stations. We first applied the technique to the Cass main shock. For this event the permanent station SNZO was available and instrument responses of the temporary stations could be verified (the Guralp station needed an adjustment of 50 in gain). We then applied the method to the smaller Cass aftershocks: the 951125\_0816, 5.2  $M_L$  and 951125\_0942 4.2  $M_L$  and 951125\_2314 4.1  $M_L$  events, using only SAPSE broadband stations. The solution for the  $M_L$  4.1 event is poorly constrained due to the low signal to noise ratio and gives the lower magnitude limit for resolvable earthquakes. Consequently we could only use one event from the data set shown in this paper, the 960124\_1744 event with  $M_L$  4.2.

### 3.5.3 Technique comparison

The 2 techniques give consistent results for all events examined (Figure 3.10a), but with varying amounts of dip-slip component. In particular, the directions of the P and T

**Figure 3.10** a) Focal mechanisms derived by moment tensor inversion are shown in the top row. Mechanisms from first motion and amplitude ratio method are given in the second row, where available. b) and c) Observed and synthetic seismograms for mechanism derived by waveform inversion. Z, R and T are vertical, radial and transverse components for the stations. Station name, azimuth and epicentral distance are given at the left. Seismogram amplitudes are normalized to 100 km distance assuming cylindrical spreading. To the right output of the amplitude ratio method. Top: Grey P and T axes of all focal mechanisms which fit all first motions, black P and T axis which fit amplitude ratios within a given error. At the bottom: P and T axes which satisfy first motions and amplitude ratios plotted on the best mechanisms (black circles are compressional, grey circles dilatations). b) Cass main shock. c) Largest Cass aftershock. This earthquake has two cluster of P and T axis, one of them (dashed nodal planes) has a focal mechanisms similar to the solution derived by the waveform inversion. This is our preferred solution.

951124.061857 951125.081617 951125.094235 951125.231427 960124.174426

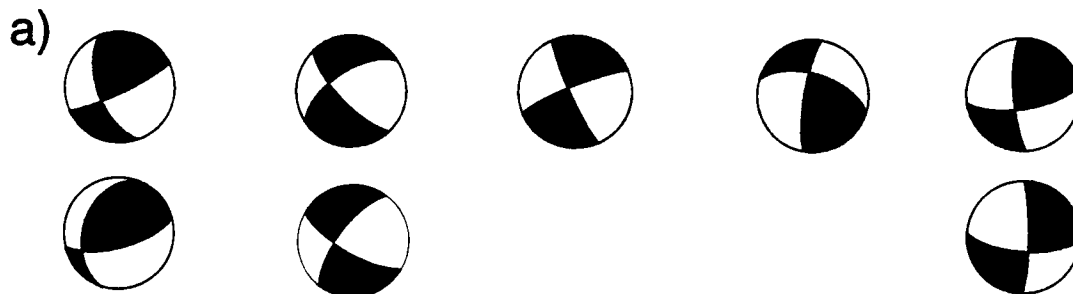
Mw=6.2  
ML=6.3  
DC=95

Mw=4.8  
ML=5.2  
DC=56

Mw=4.0  
ML=4.2  
DC=65

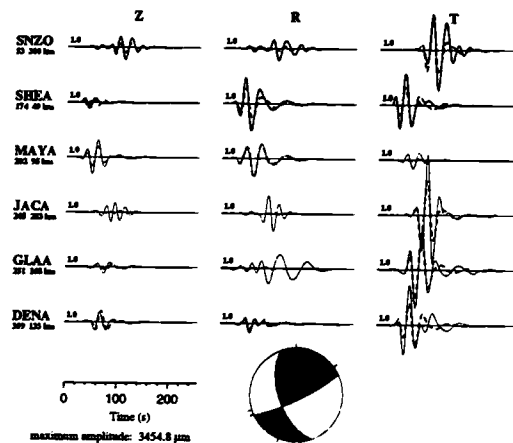
Mw=3.9  
ML=4.1

Mw=3.9  
ML=4.2  
DC=95

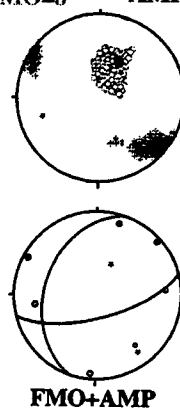


b)

951124.061857 Mw=6.20 20-50s 6km



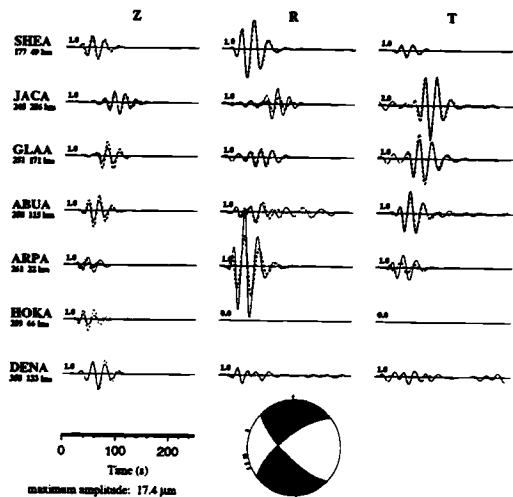
FMO=8 AMP=5



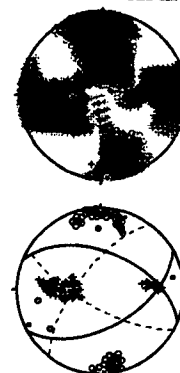
FMO+AMP

c)

951125.081617 Mw=4.76 20-30s 6km



FMO=7 AMP=5



FMO+AMP

Figure 3.10

axes are broadly similar, with trends of P and T axes varying by  $10^\circ$  between the techniques.

The Cass main shock moment tensor solution (Figure 3.10b) has a slightly higher strike slip component than the mechanisms derived with the first motion and amplitude ratio technique [Gledhill *et al.*, submitted], but is within the limits of mechanisms derived by NEIC and Harvard [Gledhill *et al.*, submitted]. The  $M_L 5.2$  aftershock (Figure 3.10c) is an example where the first motion/amplitude ratio technique gives two different type of mechanisms and is therefore classified as B quality. The P and T axes of the moment tensor inversion technique are similar in direction to one of the clusters of P and T axis (Figure 3.10c, bottom right, dashed nodal plane) and is our preferred solution. The other possible focal mechanism derived by the first motion and amplitude ratio method cannot fit the relatively large amplitudes of the tangential components (Figure 3.10c). This earthquake exemplifies that B quality mechanisms have the ambiguity of different mechanisms and need other a priori information to select a unique focal mechanism. Event 960124\_1744 is the only mechanism from the data discussed in this paper that has A quality. In Figure 3.6 we show the synthetics and observed seismograms (envelope function of waveform, 1-4 Hz) of the best fitting solution for all amplitude ratios and the full waveform inversion (waveform, 0.07-0.04 Hz). For these events the 2 techniques are providing reasonable fits to very different parts of the frequency spectrum. The amplitude ratio method shows a range of P and T axis within the given misfit. By combining the first motion information the method selects a tightly constrained mechanism. This validates our approach that amplitude ratios provide good constraints, but are best used in combination with the first motion data. The comparison demonstrates the uncertainty in using either technique for small magnitude events. For the SAPSE data, we estimate that the directions of P and T axis are constrained within  $15^\circ$  (quality A), but there is approximately  $30^\circ$  uncertainty in rake.  $M_w$  values are 0.2-0.45 smaller than the  $M_L$  calculated from the short period instruments. This is in agreement with recent observations [Anderson and Webb, 1994], that NZNSN magnitudes are overestimated by  $0.3 M_L$  owing to a local site effect at station WEL.

### 3.6 Stress Observations

Focal mechanisms of moderate sized earthquakes do not necessarily reflect slip on mapped faults but often respond to the regional stress tensor. Michael's grid search technique is used to solve for the regional stress tensor [Michael, 1987a; 1987b; 1991]. The method works under the assumption that all earthquakes occur independently and represent the same stress tensor. The grid search method changes the direction of the stress tensor in  $10^\circ$  steps and the shape factor  $\Phi$  ( $\Phi = S_2 - S_3 / S_1 - S_3$ ; where  $S_1, S_2, S_3$  are the three principal stress directions listed from most compressional to most tensional) in 0.1 increments. It tests both fault planes and selects the fault plane with the best fit to the calculated stress direction. We find maximum stress directions of  $110^\circ$ - $120^\circ$  and  $\Phi$  of about 0.5, meaning that all 3 principal stress axes have different magnitude. Confidence regions are calculated with Michael's [1987b] bootstrap technique. For the 80% confidence region the data set is sampled 500 times and each time mechanisms are randomly sampled from the given fault planes and the best fitting stress tensor calculated. To estimate the misfit for each individual mechanism, we applied Michael's inversion method originally designed for slip data [Michael, 1984]. We assign each mechanism the fault plane selected by the grid search technique as the best fitting one. The stress inversion technique calculates the best fitting stress tensor and the degree of misfit between the slip vector and traction vector for each event (within  $5^\circ$  of grid search results). A few events had misfits greater than  $100^\circ$  ( $100^\circ$ - $130^\circ$ ), and we eliminated such events from the final stress inversion.

The regional stress fields of all selected areas (Figure 3.11c) have the principal stress axis at about  $110^\circ$ - $120^\circ$  in agreement with GPS strain observations and other stress modeling in the north of our study region [Robinson and McGinty, submitted]. At the 80% confidence level the stress tensors for all regions are the same. North of Jackson Bay, the direction of the principal stress axis is horizontal at  $120^\circ$ ,  $\Phi$  is 0.5 and the mean misfit for all events is  $19^\circ$  (Figure 3.11a). The least principal stress axis is horizontal, indicating a stress field favouring strike-slip. If we subdivide the northern region further and look at

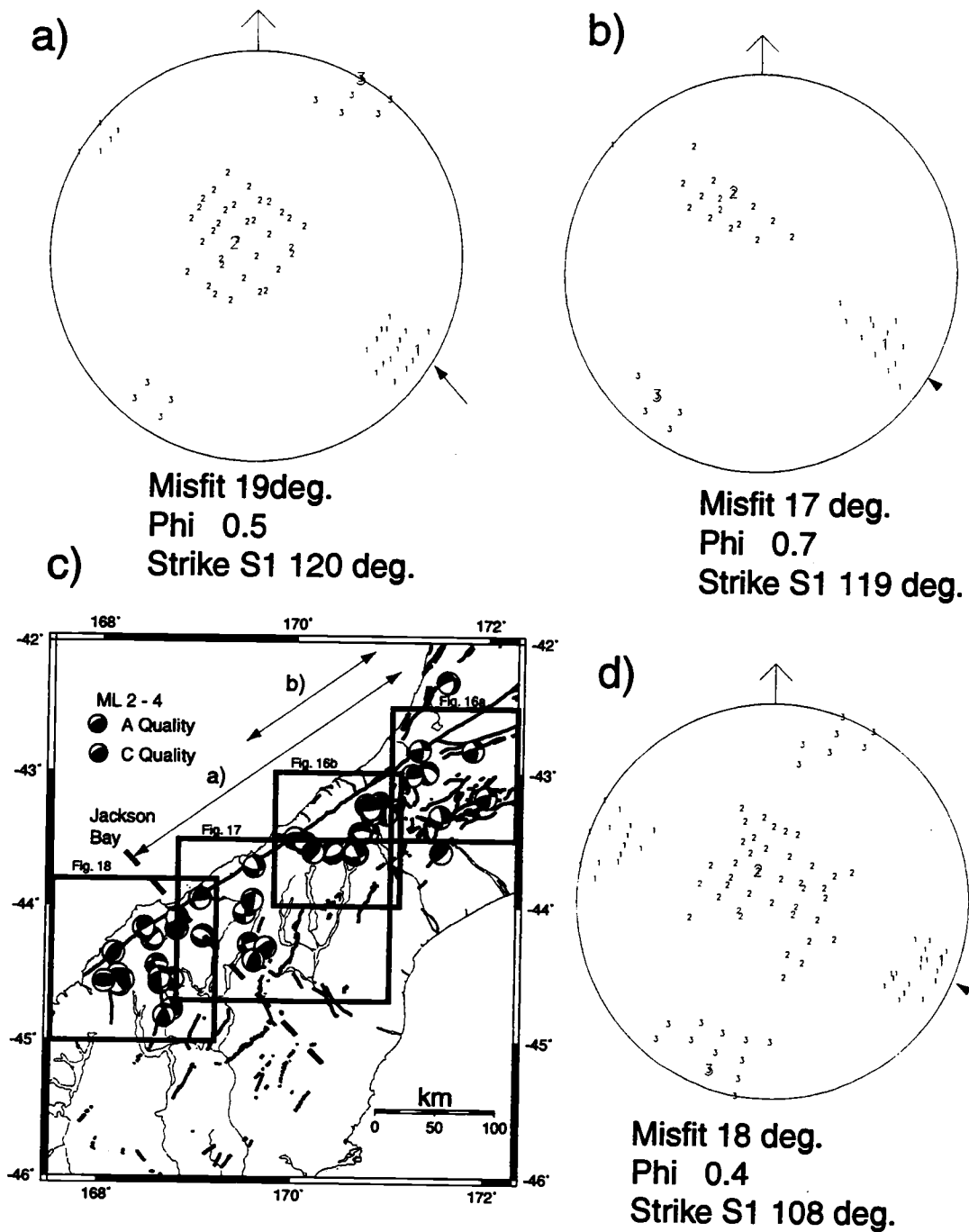


**Figure 3.11** Stereonet projection of the 80% confidence regions for the three principal stress axes of the best fitting stress tensor which fits A and C quality focal mechanisms. a) For mechanisms north of Jackson Bay; b) For mechanisms north of Mt Cook, d) For mechanisms south of Jackson Bay.

events north of Mt Cook, the results are essentially the same, but the direction of the intermediate stress axis indicates an oblique thrust component (Figure 3.11b). South of Jackson Bay the direction of the principal stress is  $108^\circ$ ,  $\Phi$  is 0.4 and the mean misfit is  $18^\circ$  (Figure 3.11c). A slight anticlockwise rotation of the principal stress axis is noticed. It is within the error limits, however an anticlockwise rotation from north to south would be in agreement with the anticlockwise rotation of the relative plate motion vector.

### 3.7 Results

To interpret the seismicity we combine all data. SAPSE data, Mt Cook earthquakes and aftershocks, and quality locations of the NZNSN and Pukaki network (for selection criteria, see data description) are plotted in map view (Figure 3.12). In the Pukaki region, the depth of earthquakes recorded by the Pukaki network agrees well with the depth of the SAPSE data (Figure 3.13f). NZNSN data (depth only resolved with minimum station distance of 25 km) have 1-2 km deeper hypocenters than the SAPSE data. Both data were located with the same velocity model and station distribution, with the only difference of the sparser network distribution for the NZNSN. The depth of the SAPSE data is better constrained and more reliable.

At the magnitude  $M_L > 3$  level, all data sets are almost complete (Figure 3.12a). At the magnitudes  $M_L > 1.8$  (Figure 3.12b) some spatial patterns are more pronounced, especially within the Pukaki network due to the lower magnitude completeness threshold. Seismicity with  $M_L < 3$  is probably as high in other regions [Rynn and Scholz, 1978; Scholz *et al.*, 1974], but only microseismicity studies can resolve that.

Earthquakes occur in a wide region from west of the Alpine fault to Central Otago. In the northern third of the study region the band of seismicity is only 60 km wide, whereas farther south, the band is up to 100 km wide. The narrower seismicity band appears to reflect the narrower Greywacke belt and the seismicity band widens within the wider belt of Schist. The distinctive changes from south to north in the level and spatial distribution of seismicity are discussed below in conjunction with focal mechanisms and the tectonics of the Alpine fault and the southern region of the Marlborough fault system.

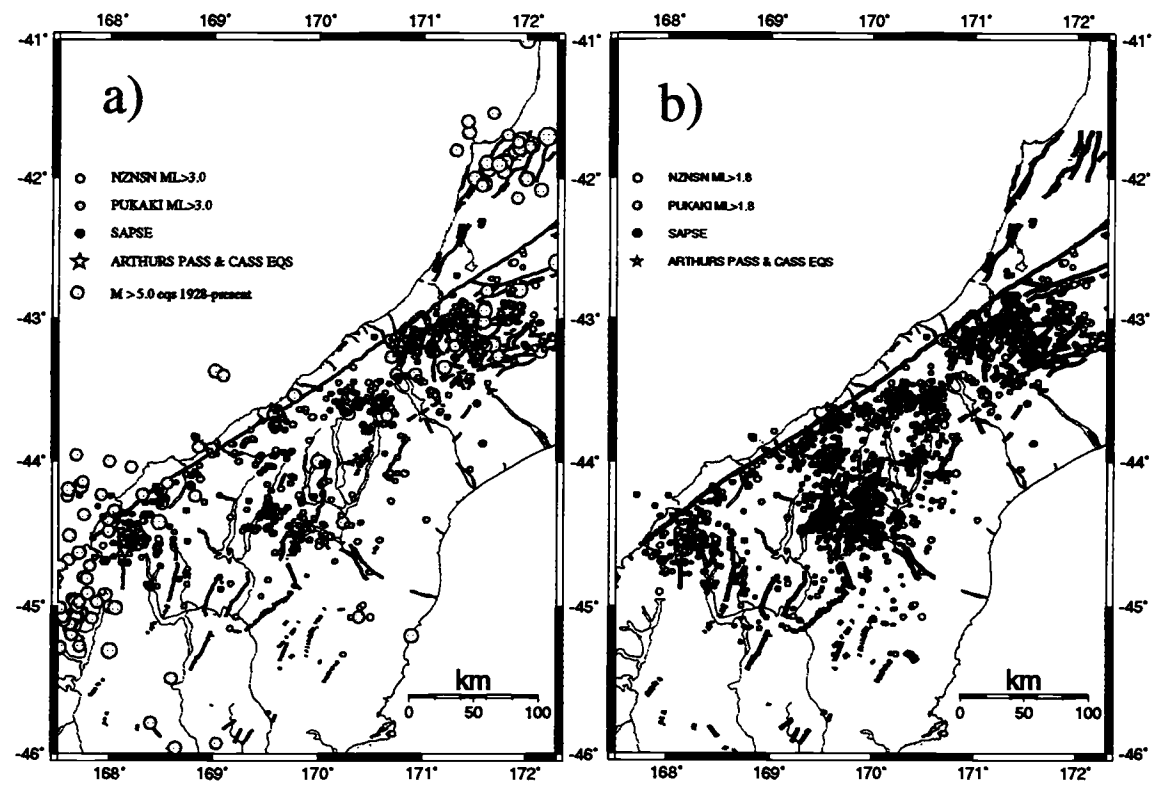


**Figure 3.12** Maps showing quality locations of SAPSE (black), Pukaki (grey) and NZNSN (open circles) earthquakes. a)  $M_L > 3$ , Large grey circles are  $M_L > 5$  earthquakes since 1920. Note that larger earthquakes follow the seismicity patterns for the smaller earthquakes. b)  $M_L > 1.8$ . See text for details.

### 3.7.1 Depth of Seismicity

The most striking observation is that the maximum depth of crustal seismicity is uniform over large parts of the central South Island at about 10-12 km depth (light grey in Figure 3.5, Figure 3.13). Microseismicity studies in Canterbury [Reyners and Cowan, 1993], along the Alpine fault [Rynn and Scholz, 1978; Scholz et al., 1974] and within the Marlborough fault system [Reyners, 1989; Reyners et al., 1983; Reyners et al., 1997; Robinson et al., 1994] also show the maximum depth of upper crustal seismicity at about 12 km. The maximum depth of seismicity provides an estimate of the thickness of the seismogenic zone and therefore relates to the brittle/ductile transition zone [Scholz, 1990; Yeats et al., 1997]. Seismogenic thickness of continental crust depends on the thermal gradient and the rheology of the material, but often falls within the range of 12-15 km [Scholz, 1990; Yeats et al., 1997]. The consistent maximum earthquake depth throughout the central South Island suggests that regional isotherms do not vary across the Southern Alps at wavelengths greater than 30 km. Locally, in regions smaller than 30 km, we observe changes in the maximum earthquake depth and this is outlined below. The crustal structure derived along both transects show uniform velocities of 5.8 to 6.2 km in the upper 25-30 km thick crust [Holbrook et al., 1998; Kleffmann et al., 1998a; Stern et al., 1997] at distances of 30-100 km east of the Alpine fault. No crustal boundary, no change in seismic character, and no change in electric conductivity are apparent near the base of the seismogenic zone observed in this study.

Three regions are anomalous. North of Franz Josef Glacier seismicity ( $M_L > 2.0$ ) is almost absent in a 10-20 km wide band (Figure 3.5, dark grey, Figure 3.12). Results from geophysical investigations of the northern and southern seismic transects (marked T1 and T2, Figure 3.3c) indicate low velocity zones near the Alpine fault and up to 30 km east of the fault [Holbrook et al., 1998; Kleffmann et al., 1998b; Stern et al., 1997] on both transects. Bannister et al. [1998] imaged a low velocity region with 3-D tomographic inversion of active and passive source data, which extends from Franz Josef Glacier to the Waitaha River. The low velocity on the southern transect is likely caused by fluids

**Figure 3.13** Seismicity along 3 cross sections shown in Figure 3.5 projected orthogonal to the Alpine fault. Half width of the cross sections is 25 km. SAPSE locations are indicated by open circles and Pukaki network locations are marked by black circles. Isotherms near Franz Josef and Haast are from Shi et al's [1996] preferred model with no friction. a), d) and g) shows topography along the cross sections. b), e) and h) shows the Bouguer anomaly in mGal. Along the cross section the 350°C isotherm of Shi et al. [1996] is marked as thick black line in Figures c) and j). The 350°C isotherm from Koons [1987] is shown as dashed line on Figure 3.13c. Grey triangles in f) mark the projected location of the Pukaki network stations. Pukaki network locations in the western half of the profile have consequently larger errors than in the eastern half.

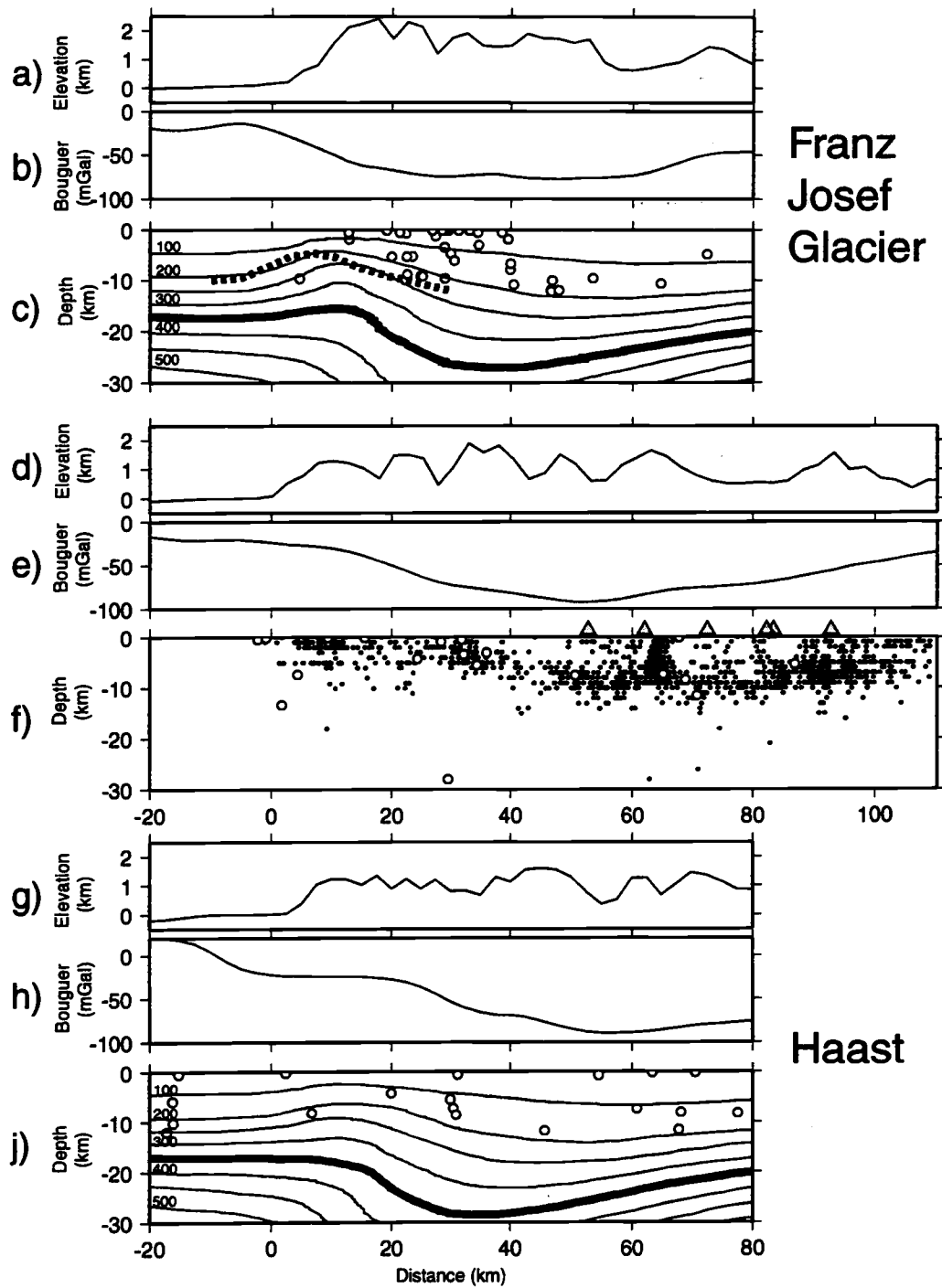


Figure 3.13

under high pore pressure [Kleffmann *et al.*, 1998b]. Holbrook *et al.* [1998] suggest that the low velocity zone at the northern transect is caused by a combination of fluids and high mid-crustal temperatures. Magnetotelluric measurements along the northern transect show a prominent u-shaped eastward dipping high conductivity zone at about 25 km depth and a horizontal high conductivity zone at 10 km depth. The high conductivity layer is possibly attributed to fluids released by metamorphism which could result in a sudden increase in electrical conductivity. The upper horizontal layer may represent the transition to the brittle/ductile zone and the fluids are possibly trapped under compression (G. Caldwell, personal communications, 1999). This feature only extends 30 km east of the fault and appears to overlap with low velocity zones imaged by the northern transect, the 3-D tomographic inversion and the zone of low earthquake activity (dark grey in Figure 3.5). In Figure 3.13c SAPSE earthquakes, the isotherms of Shi *et al.* [1996], and Koons [1987b] (only 350°C, dotted line) are plotted across the Southern Alps. The main difference between the models is that Shi *et al.* [1996] incorporated crustal thickening in their model, which caused depression of the 350°C isotherm. Both models are based on known plate motion and uplift rates, but vary considerably in the depth to the brittle/ductile transition zone and shape of the isotherms. Given the large differences between thermal models and estimated depths to the brittle/ductile transition zone from fission track and fluid inclusion data (between 250°C at 10 km [Kamp and Tippett, 1993]; and 400°C at 5 km [Craw, 1988; Craw *et al.*, 1994]) only the shape and extent of the thermal anomalies are comparable with the earthquake distribution. If the lack of seismicity is caused by higher temperatures, than temperatures are higher to the east of the fault and require a narrow heat anomaly. Shi *et al.* [1996] incorporated crustal thickening in their uplift models, which depresses the brittle/ductile transition zone in regions of thickened crust (Figure 3.13). Our data do not confirm a deepening of the brittle/ductile transition zone.

Beneath Mt Cook, the Lake Pukaki network data show the base of earthquake depths to be shallower by 1-2 km (Figure 3.13f), although too few SAPSE earthquakes were recorded to confirm this. Note that the earthquakes from 0-40 km distance to the Alpine fault have relatively large errors, since the Lake Pukaki network was centered over the eastern half of the cross section. The area characterised by shallower earthquake depth is

marked by the medium grey colour in Figure 3.5. The data support slightly elevated isotherms east of the Alpine fault. The Alpine fault itself has earthquakes down to a depth of 10-12 km.

Near Haast, thermal models predict lower thermal gradients due to lower uplift and convergence rates. Shi et al. [1996] modeled this assuming 30% of crustal shortening by uplift and 70% as crustal thickening. In comparison with Franz Josef, the isotherms are only slightly elevated and more depressed below the 350°C isotherm. The SAPSE earthquakes support a seismogenic depth of about 10-12 km.

Farther south, a region of shallow maximum earthquake depth is centered at the Alpine fault near Jackson Bay. It appears to be a localised feature. This section of the Alpine fault is characterized by almost pure strike-slip motion with a small amount of extension. This is observed near Cascade River and offshore south of Milford Sound. It is possible that the change of the plate boundary from the Alpine fault to subduction below Fiordland is causing extension and associated higher heat flow. Heat flow measurements near Haast are higher than normal at 60°C/km, and a hot spring near Cascade River points to elevated temperatures in the region.

Deep earthquakes (80-100 km) are only observed in a small region near Milford Sound (Figure 3.5) and are likely to occur at the northern tip of the subducting Australian plate. North of Jackson Bay, only one event in the study is deeper than 15 km. This event is at 30 km depth and at a distance of 30 km east from the Alpine fault (Figure 3.5 and 3.13f). Given an estimated dip of about 45° of the Alpine fault it could have occurred on the Alpine fault. We do not observe deep earthquakes below the Lake Pukaki region, as Reyners [1987] did. These earthquakes appear to occur very infrequently and Eberhart-Phillips [1995] did not observe them in her 3.5 year study. The Pukaki network recorded only 12 earthquakes deeper than 50 km compared to 2800 earthquakes in the shallow crust between 0-15 km depth.

### 3.7.2 Alpine Fault

SAPSE observed 60 earthquakes in a band from 5 km left to 15 km right of the surface fault trace of the Alpine fault (Figure 3.14a). Given an approximate fault dip of  $45^\circ$  these earthquakes occurred on or close to the fault, therefore outlining its seismogenic zone. Seismicity is highest just north of Milford Sound (Figure 3.3a). North of Bruce Bay the seismicity rate drops abruptly. Between Bruce Bay and the Wanganui River seismicity of the Alpine fault is unusually low both during the SAPSE and the 8 years of NZNSN recordings. The occurrence of a few earthquakes up to 10 km depth (Figure 3.14a) suggests that the crust in the vicinity of the Alpine fault is capable of releasing elastic strain seismically and that the fault does not behave aseismically. The seismicity rate is comparable with rates of locked sections of the San Andreas fault (Figure 3.15), where large historic earthquakes have been recorded. Both the Carrizo Plain and the Mojave section of the San Andreas fault experienced no earthquakes larger than  $M_b=3.5$  over the time period 1990-1997 (same time span as the NZNSN data set shown in this study), and show only few events larger than  $M_b$  2.5 (Figure 3.15), which is the threshold of our study. Despite the relatively low frequency of magnitude  $M_b > 2.5$  earthquakes on this locked section of the San Andreas fault, 2 historic earthquakes of approximately  $M_w=7.9$  (Fort Tejon, 1857) and  $M_w=7.5$  (Wrightwood earthquake, 1812) demonstrate that large events occur. The 1868 Hayward fault  $M=7.0$  earthquakes are examples for seismic strain release of a creeping segment of the San Andreas fault. This shows that aseismic regions are able to store elastic strain, although the mechanism is not fully understood (Robert Yeats, personal communications, 1999). Given that parts of the Alpine fault are bounded by thermally weakened crust to the east and stronger Australian plate crust to the west, we expect that it is possibly to store elastic strain in this regions. Elsewhere field evidence and numerical models of earthquake rupture show that slip often propagates along the interface between weak and strong material but rupture anisotropy may occur such that there would be a preferred direction for rupture

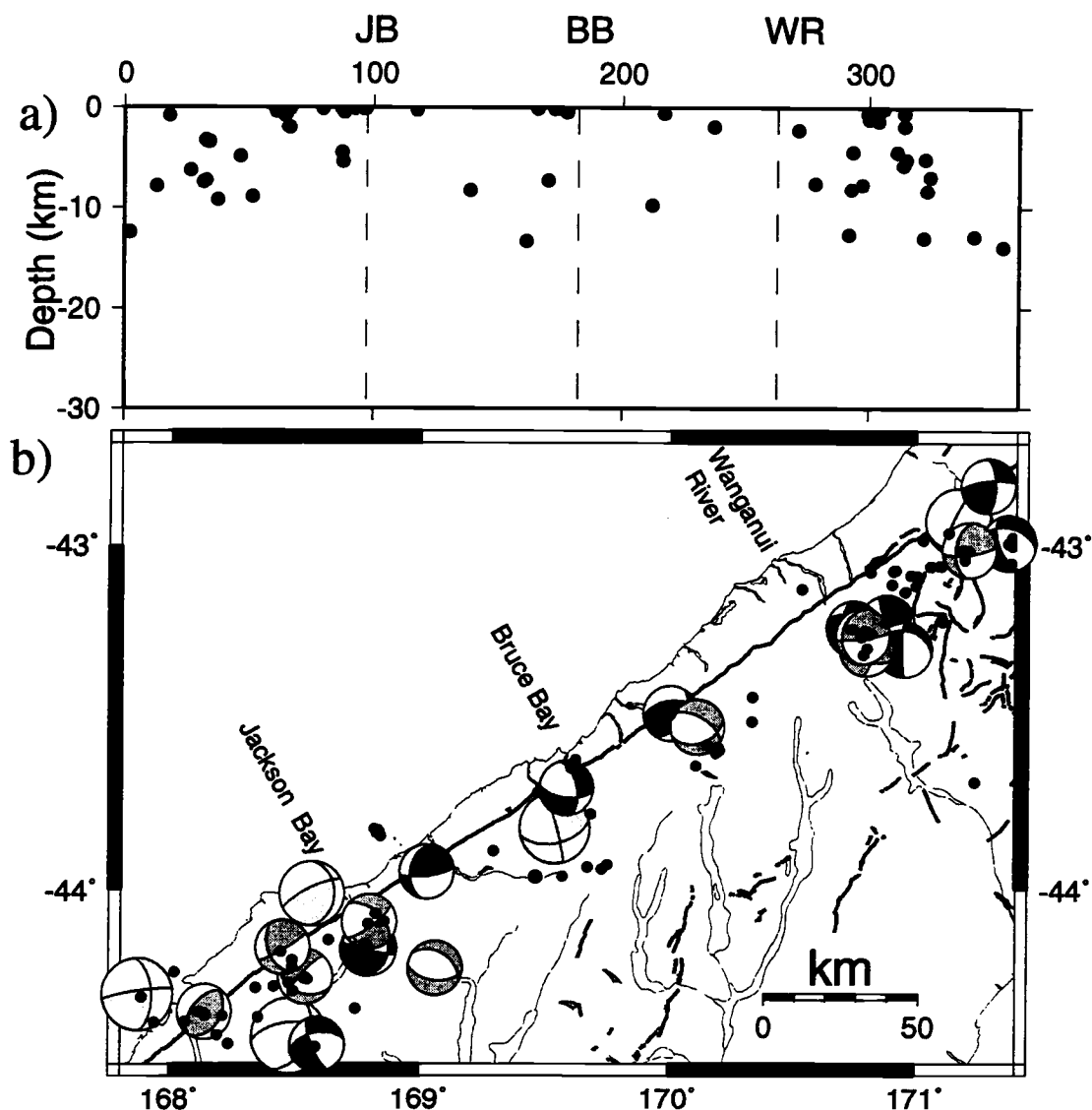


**Figure 3.14** Alpine fault seismicity and focal mechanisms. a) SAPSE earthquakes within 5 km to the left and 15 km to the right of the fault surface trace projected on a cross section parallel to the Alpine fault from Milford Sound to Arthur's Pass. JB Jackson Bay, BB Bruce Bay, WR Wanganui River. b) Mapview of SAPSE seismicity with lower hemisphere projections of A quality (compressional quadrant black) and C quality (compressional quadrant middle grey) focal mechanisms. Focal mechanisms with light grey compressional quadrants are lower hemisphere projections of the focal mechanisms for  $M_w > 5.5$  earthquakes derived by body waveform modeling [Harvard CMT catalogue; *Anderson et al.*, 1993].

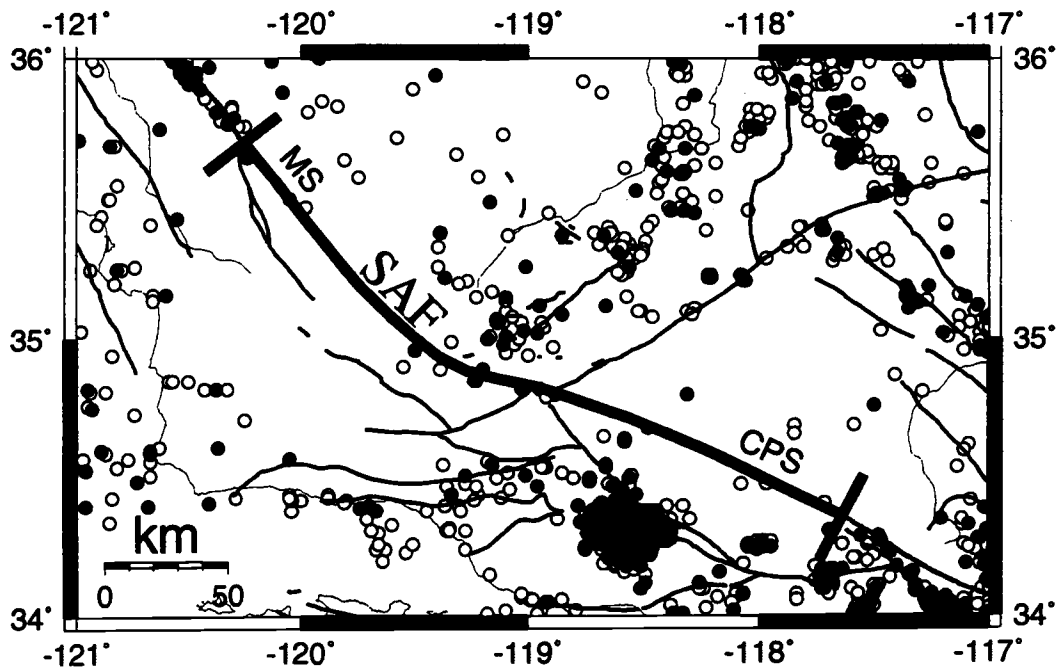


**Figure 3.15** Seismicity with  $M_b > 2.5$  in Southern California between 1990-1997. Open circles have  $M_b$  of 2.5-3.0; grey circles have  $M_b$  of 3.0 - 3.5 ; black circles have  $M_b$  of 3.5 and higher. The Carrizo plain and Mojave segments of the San Andreas fault has a low seismicity rate during this observation time, but has ruptured in 2 great earthquakes. The location of these earthquakes are not exactly known, but they ruptured the San Andreas fault between the two solid bars (data courtesy of SCEC at <http://www.scec.edu>). MS Mojave segment; CPS Carizo plain segment.

propagation [Harris *et al.*, 1994]. While this is usually considered for shallow depths, it may also apply to the Alpine fault at depth of 5-10 km.

A  $M_w$  5.4 earthquake south of Bruce Bay possibly occurred on the Alpine fault in September 1998. This earthquake caused minor damage, and was widely felt along the West Coast and throughout Central Otago. The Harvard CMT mechanism (Figure 3.14, latitude  $43.8^\circ$ ) is an oblique strike-slip earthquake with a  $20^\circ$  clockwise rotation of the strike to the Alpine fault. Small strike-slip segments of the Alpine fault do have similar strike but are possibly only a few km deep [Norris and Cooper, 1995]. The strike of the mechanism has an error of about  $10\text{-}20^\circ$ , which falls within the error of the method.

The seismogenic depth of the Alpine fault is about 10-12 km. This agrees with the GPS strain modeling results, which estimate a locking depth of 10-12 km at Haast (C.F. Pearson, personal communication, 1998). Our estimate of the maximum seismogenic depth of the Alpine fault near Franz Josef Glacier is 10 km and deeper than the 5-8 km estimate from GPS observations in this region [Beavan *et al.*, submitted].

### 3.7.3 Northern Transition Zone

Seismicity attributed to the Hope and Porters Pass fault zones appears to reach as far south as Mt Cook. The intersection of the Hope and Alpine faults must be a complex zone of deformation rather than an intersection of distinct faults. From the Hope fault intersection to the Wanganui River earthquake activity is high (Figure 3.12) and concentrated in the 20 km wide zone immediately adjacent to the Alpine fault, with only few earthquakes located directly on the fault (Figure 3.12). The earthquakes are distributed at all depths down to about 9 km, with the exception of one event at 12.8km depth. Strike-slip events near the Hope fault coincide with the strike of the Marlborough fault system and are steeply dipping to the west, if we select the fault plane that has right lateral slip (Figure 3.16). The Arthur's Pass, Cass and Wilburforce River earthquake sequences occurred in this zone where the Hope and Alpine fault systems intersect. We only have few earthquakes from SAPSE in the region, since we excluded the aftershocks of the Cass and Arthur's Pass earthquakes. North of Lake Pukaki, earthquake

**Figure 3.16** Seismicity and focal mechanisms from the Hope fault to Mt Cook. a) Lower hemisphere projections of A quality (compressional quadrant black) and C quality (compressional quadrant middle grey) focal mechanisms. Mechanism with light grey compressional quadrants are lower hemisphere projections of the focal mechanisms for  $M_w > 5.5$  earthquakes derived by body waveform modeling [Harvard CMT catalogue; *Anderson et al.*, 1993, *Doser and Webb*, submitted]. Arthur's Pass earthquake is marked with A. The Cass earthquake (marked with C) and 3 aftershock mechanisms were derived by broadband waveform modeling in this study and have dark grey compressional quadrants. W = Wilburforce River earthquake. Quality locations (see also Figure 3.12b) for earthquakes with  $M_L > 3$  recorded by the NZNSN (open circles) show the NNW-SSE trend of the Arthur's Pass and Cass earthquake aftershock zones. Only few SAPSE earthquakes were selected in this region. Dashed line in the north marks the boundary of the study region where seismicity is artificially truncated. PPFZ = Porters Pass fault zone. b) Lower hemisphere projections of A quality (compressional quadrant black) and B quality (compressional quadrant dark grey) focal mechanisms. Mechanism with light grey compressional quadrant is a lower hemisphere projection of the  $M_w$  6.2 Godley River [*Anderson et al.*, 1993] earthquake mechanism. Normal faulting mechanisms east of Mt Cook are composite solutions (marked with HC) and are possibly hydrologically triggered. Quality locations (see also Figure 3.12b) for earthquakes with  $M_L > 3$  recorded by the NZNSN (open circles), SAPSE (solid circles), and Pukaki (grey circles) are shown. Black star marks Mt Cook, white stars are shotpoints of the two transects T1 and T2. Note the region of decreased seismicity between the Alpine fault and the western margin of Lake Tekapo.

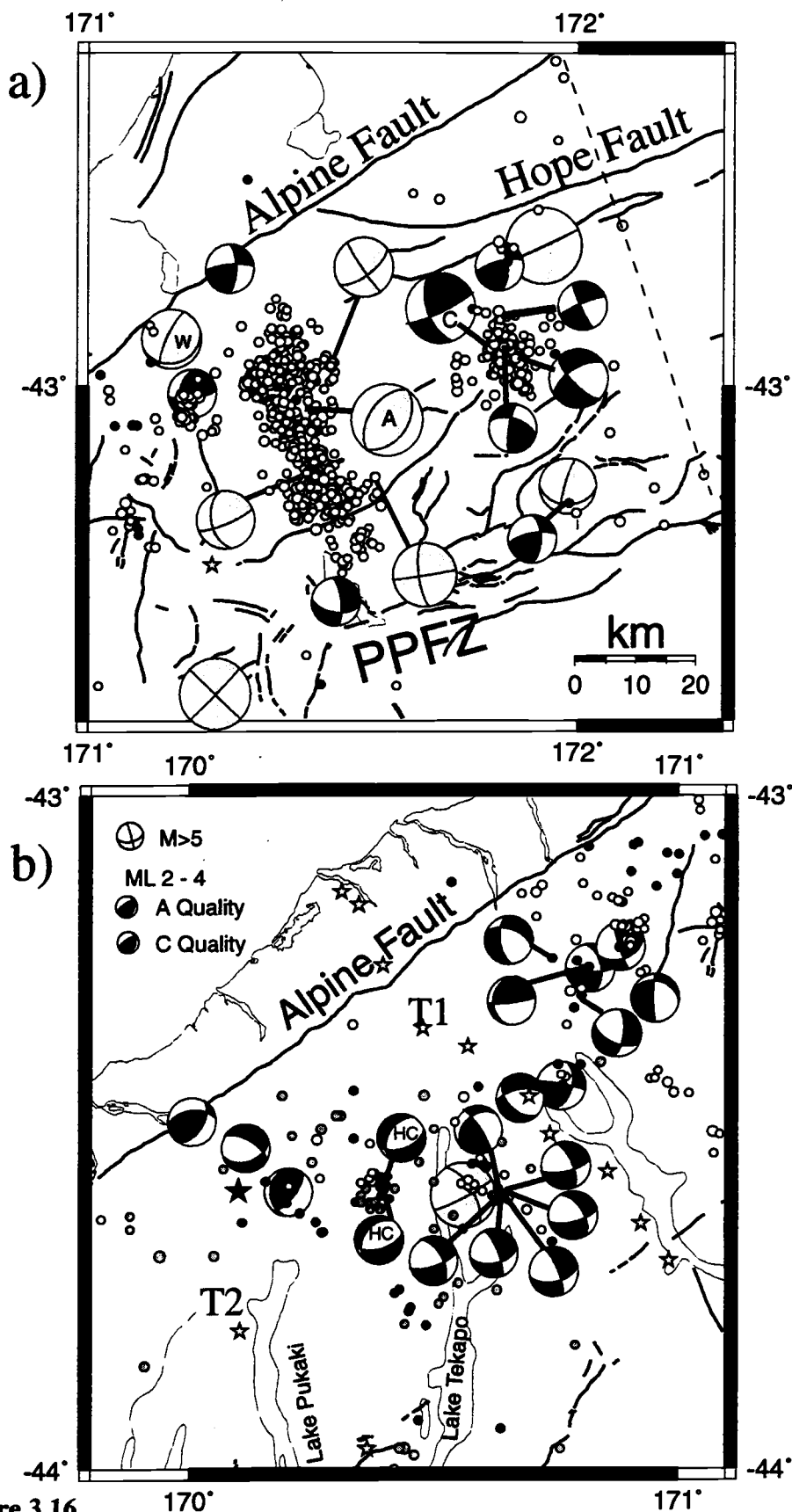


Figure 3.16

mechanisms vary considerably, but P axes are within the same range. The high seismic activity appears to be caused by the increased stresses at the oblique intersection of the dextral Hope and Alpine faults. The locus of seismic strain release is located east of the Alpine fault and focused near the Hope and Porters Pass fault zone.

Both the  $M_w$  6.7 1994 Arthur's Pass [Anderson *et al.*, 1993; Robinson and McGinty, submitted] and 1995  $M_w$  6.2 Cass earthquake [Gledhill *et al.*, submitted] have thrust components in a region where previously only strike-slip earthquakes have been observed. The Arthur's Pass earthquake was primarily a reverse faulting event with NE-SW strike. This fault direction is parallel to the strike of strike-slip faults in the region, but is not favourably oriented for reverse slip in this stress regime. Aftershocks follow a NNE-SSW trending zone, have varied mechanisms and respond to the regional stress field [Robinson and McGinty, submitted]. The Cass earthquake was probably triggered by the Arthur's Pass earthquake. It had an oblique strike-slip mechanism and, based on the  $330^\circ$  trending aftershocks, ruptured along a NNW-SSE trending westward dipping fault. The NNW-SSE trend of aftershocks of both earthquakes and the thrust component of their mechanisms suggest that they comprise part of the plate convergence normal to the Marlborough fault system [Robinson and McGinty, submitted]. It appears that earthquake slip in this region is partitioned into components fault parallel and normal to the plate margin [Gledhill *et al.*, submitted; Robinson and McGinty, submitted].

South of the Wanganui River the seismicity steps further away from the Alpine fault (Figure 3.5) until a west-east striking band of seismicity intersects the Alpine fault obliquely (Figure 3.12). This band of seismicity is especially pronounced when lower magnitude events are included. It includes the  $M_w$  6.2 Godley River earthquake [Anderson *et al.*, 1993]. The seismicity band appears to be the continuation of the Porters Pass fault zone and is either a direct expression of the fault zone or, as seen at the Hope fault intersection, connected with the increased stresses south of the intersection of the Porters Pass and Alpine fault zone. The Godley River earthquake occurred in a remote region with no mapped faults and had no observed surface rupture. Anderson *et al.* [1993] suggests that it occurred on the continuation of the Porters Pass fault zone, which is similar in strike to the NE-SW trending plane with right lateral strike-slip. Six

earthquakes located just to the southeast of the Godley River earthquake (Figure 3.16b) have very similar focal mechanisms and possibly occurred on the same fault.

Seismicity connected to the Porters Pass fault zone is not surprising since geological [Cowan *et al.*, 1996] and geodetic measurements [Beavan and Haines, in preparation; Pearson *et al.*, 1995] confirm its activity. The September 1997  $M_w$  5.0 earthquakes and aftershocks occurred in this region (Figure 3.16b) east of the Alpine fault in the adjacent crust. Two focal mechanisms from the aftershocks indicate thrust and oblique slip mechanisms consistent with uplift of the Southern Alps and small-scale strain partitioning as seen in the Arthur's Pass earthquake.

A 20-km wide region of nil seismicity lies just northwest of the Porters Pass fault zone. Thus the interaction of this incipient fault zone with the Alpine fault could be a significant factor in causing low seismicity. The present plate boundary appears to lie near the Hope and Porters Pass fault zone. The section of the Alpine fault immediately west of this zone is getting less active and could extend the northern part of the seismic inactive Alpine fault north of the Hope fault down to Mt Cook in the future. 3-D geodetic data support this hypothesis. There is a well resolved drop in the total shear strain rate in the low seismicity region (see Figure 4 in Beavan *et al.*, [submitted]) and a change in the vorticity near Mt. Cook (M. Henderson, personal communication, 1999). In this region it is not appropriate to develop a 2-D strain model.

East of Mt Cook two sequences of 8 and 4 earthquakes occurred on the 13th and 22<sup>nd</sup> December 22, 1995 (dashed line, Figure 3.16b). The earthquakes occurred in the same location, and were separated by a few hours and had magnitudes of about  $M_L$  2.5-3. The waveforms and polarities of all events are very similar, and show distinct P and S arrivals. Therefore rock avalanches and glacier breakup are unlikely sources. No man made activity occurs in this remote area of the Southern Alps. The composite solution for these events suggest normal faulting with NW-SE extensional axis (mechanism marked HC, Figure 3.16b). The occurrence within several hours of each other and during the early summer do suggest that they are possibly hydrologically triggered [Wolf *et al.*, 1997]. Their P axes have a large misfit to the regional stress tensor and were excluded from the stress inversion.

In contrast, the normal faulting mechanisms north of Mt Cook have P axis aligned to the regional stress field. We observe several normal faulting mechanisms with NNE-SSE extensional axes within 15-30 km distance east of the Alpine fault. They could indicate local extension due to gravitational collapse. Beavan et al.'s [submitted] observe negative strain in this region, which could explain the mechanisms.

#### 3.7.4 From Mt Cook to Haast

In the region from Mt Cook to Haast, the seismicity is comparatively lower and more broadly distributed, including bands of seismicity 30 and 80 km east of the Alpine fault (Figure 3.5). This region may be most compatible with models of Alpine fault deformation [Koons, 1990; Koons, 1994], since it lies south of the Marlborough fault system and north of the Puysegur subduction zone. Numerical modeling of the collision zone as a two sided orogen with erosion on the steep inboard wedge and a gentle sloping surface on the outboard wedge [Koons, 1990; Koons, 1994] predicts the highest strain rates (both contractional and rotational) adjacent to the plate boundary and a broad higher strain zone in the outboard region. At the main divide, there is little contractional strain, and extension occurs parallel to the plate boundary. The seismicity zone at 30 km distance from the Alpine fault is near the main divide and has oblique thrust and strike-slip mechanisms, which may be representative of the backthrust zone. The distributed zone 80-100 km from the Alpine fault is near the outboard toe, where oblique thrusting is expected. Focal mechanisms east of the Southern Alps, especially at the thrust front, have a high thrust component and tend to be aligned with the NNE strike of mapped faults (Figure 3.17). The moment release rate, calculated from NZNSN seismicity between 1990-1997 across the region, (Figure 3.17a) is highest at the Alpine fault, decreases towards the east and shows another small high at 75-95 km distance from the Alpine fault. The relative change of moment release across the Southern Alps is similar to the numerical calculated strain curve [Koons, 1994; Koons et al., 1998] and measured strain rates across the Alps (John Beavan, personal communications, 1999), but is 2-3 orders of

**Figure 3.17** Seismicity and focal mechanisms from Mt Cook to Jackson Bay. a) Moment release/per year calculated for rectangular regions 130 km long parallel to the Alpine fault (marked by solid bars perpendicular to the Alpine fault in Figure 3.17b) and 25 km width perpendicular to it. Included are quality locations for  $M_L > 3.0$  earthquakes recorded by the NZNSN during 1990-1997 (Figure 3.3a). b) Lower hemisphere projections of A and C quality (compressional quadrant black), and B and D quality (compressional quadrant dark grey) focal mechanisms. Mechanisms with light grey compressional quadrants are lower hemisphere projections of the focal mechanisms for the 1998  $M_w$  5.4 Alpine fault (Harvard CMT; Abercombie, personal communications, 1999) and the  $M_w$  6.2 Godley River [Anderson *et al.*, 1993] earthquakes. Quality locations (see also Figure 3.12b) for earthquakes with  $M_L > 3$  recorded by the NZNSN (open circles), SAPSE (solid circles), and Lake Pukaki (grey) networks show that seismicity clusters around some of the NNE-SSW striking faults. Black star marks Mt Cook, white stars are shotpoints along the two transects T1 and T2.

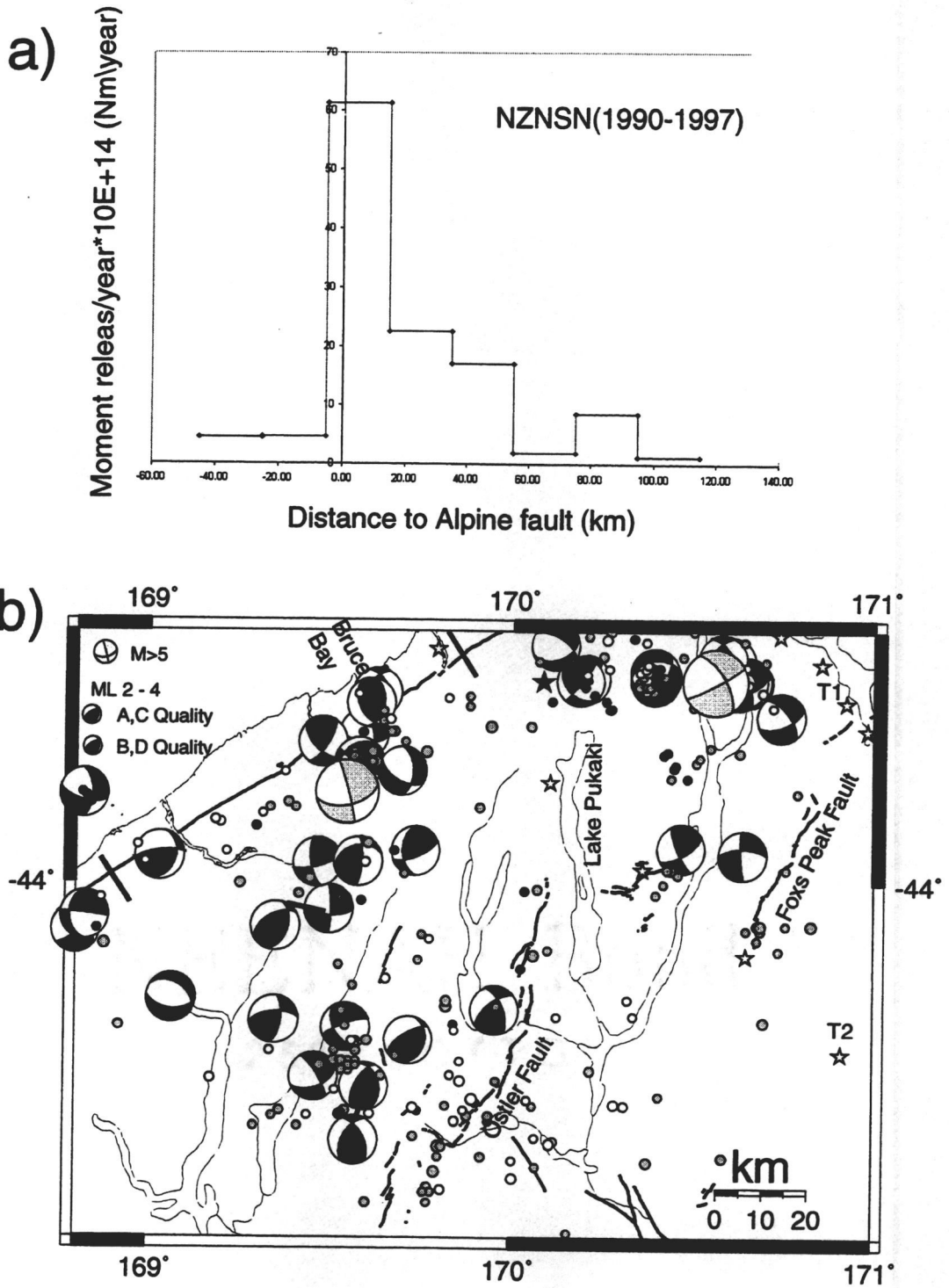


Figure 3.17

magnitudes smaller than the predicted strain accumulation from plate convergence and GPS observations.

The earthquake data over the last 150 years show that only a small percent of the strain accumulation across the Alpine fault has been released seismically. The Alpine fault appears to be locked and has the potential to rupture in big earthquakes in agreement with paleoseismic evidence for large earthquakes. The broad region of deformation east of the Alpine fault is marked by earthquakes (Figure 3.17a) and would be best modeled by small NNE trending reverse faults, scattered throughout the region. The distributed strain across the Southern Alps is observed by the GPS network as far as 80 km east from the fault. Beavan et al.'s [submitted] model the long wavelength displacement as distributed deformation beneath the Southern Alps or by localization of elastic strain on a NW dipping fault or shear zones slipping stably below 30 km depth. Our data suggests that the locking depth in this zone is shallower at about 12 km locking depth and that it should be modeled on discrete NNE trending faults.

### 3.7.5 Southern Transition Zone

South of Jackson Bay is the transitional region between the Alpine fault and the Puysegur subduction zone. At the southern part of the Alpine fault, where the dip-slip component disappears, seismicity is observed on both sides of the fault, indicating shortening normal to the Alpine fault (Figure 3.1 and 3.12).

With few exceptions the focal mechanisms (Figure 3.18) are not parallel in strike to the trend of local structures. They can be modeled by a uniform stress field. The deep earthquakes (Figure 3.5) represent the northern edge of the subducting Australian plate. There is a relatively high level of seismicity in the vicinity of this edge and the focal mechanisms vary widely, presumably due to small-scale complexities between the Australian and Pacific plates.

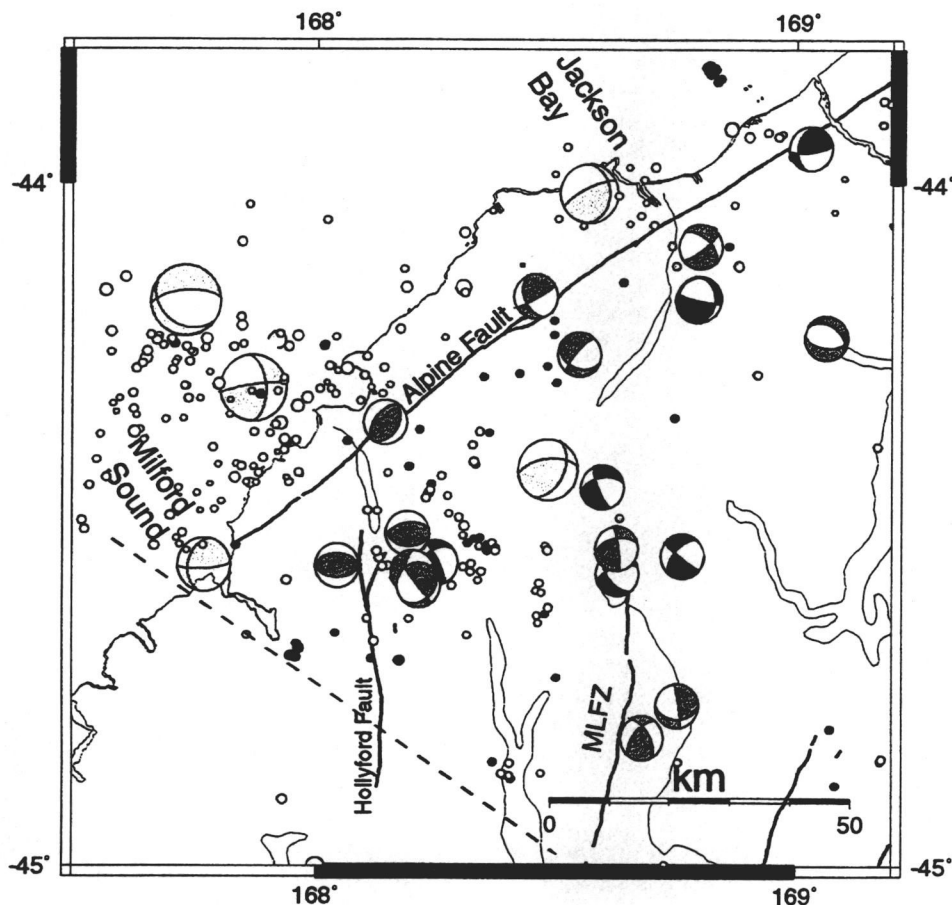


**Figure 3.18** Seismicity and focal mechanisms south of Jackson Bay. Lower hemisphere projections of A quality (compressional quadrant black) and C quality (compressional quadrant dark grey) focal mechanisms. Mechanisms with light grey compressional quadrants are lower hemisphere projections of focal mechanisms for  $M_w > 5.4$  earthquakes derived by body waveform modeling [Harvard CMT catalogue, *Anderson et al.*, 1993, *Doser and Webb*, submitted]. NZNSN earthquake locations of  $M_L > 3$  (open circles) are selected using the quality criteria described in the text (shown in Figure 3.3a) for the region east of the Alpine fault. Offshore, all recorded earthquakes with  $M_L > 3$  are plotted. Thus, location errors are relatively large, but the distribution shows that in this region seismicity occurs west of the Alpine fault. Earthquakes recorded by SAPSE are marked by solid circles. MLFZ = Moonlight fault zone. Dashed line in the south marks the end of the study region where seismicity is artificially truncated.

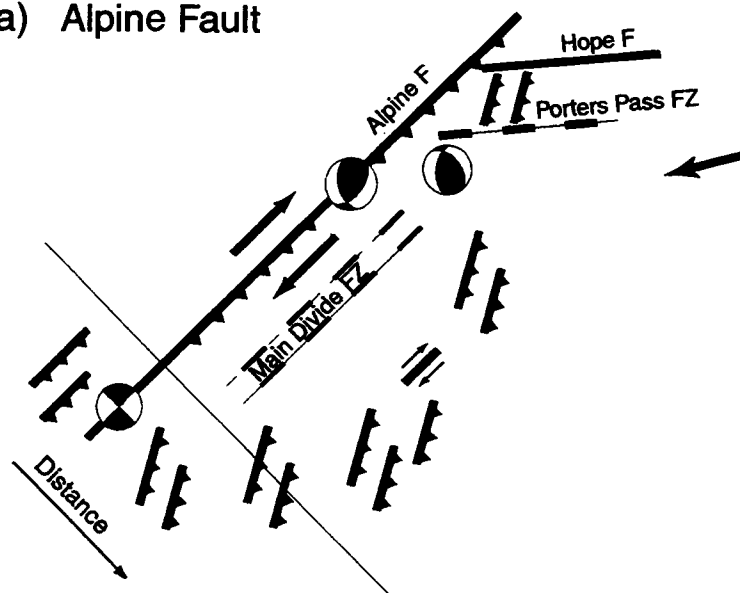
### 3.8 Conclusions

We calculated 130 focal mechanisms with a first motion and amplitude ratio method, 50 % had well constrained solutions (25 % of the data). The technique is fully exploited, since due to relative low magnitudes and average station distances of 50 km, both amplitude ratios and first motions are necessary to constrain the focal mechanisms. Comparison with moment tensor inversions, carried out for the three largest earthquakes, confirms the focal mechanisms and a 0.2-0.3 overestimation of NZNSN magnitudes. Reliable moment tensors were determined for earthquakes with  $M_w > 4$  and demonstrate the usefulness and magnitude threshold of this method in the New Zealand environment.

The Alpine fault's maximum seismogenic depth is about 10-12 km and slightly deeper near Milford Sound (15 km depth). The seismic data do not confirm high temperatures at the Alpine fault. The seismicity rate on the Alpine fault is comparable to locked sections of the San Andreas fault [Jones, 1988] with large earthquakes expected on the Alpine fault. East of the Alpine fault, near Mt Cook, the maximum seismogenic depth is 1-2 km shallower, which could suggest higher temperatures in a localised region east of the Alpine fault.

Low seismicity north of Bruce Bay coincides with high uplift rates and the intersection of the Alpine fault with the Marlborough fault system. The lack of seismicity at and near the Alpine fault north of Franz Josef Glacier is offset to the north from the region of highest uplift rate and therefore possibly not connected with elevated temperatures. It is intriguing that this zone coincides with a low velocity zone and high conductivity zone imaged in this region, suggested to be caused by the presence of fluids and elevated temperatures [Kleffman *et al.*, 1998b; Holbrook *et al.*, 1998; Bannister *et al.*, 1998]. The earthquakes in this study and a 3-D GPS survey [Beavan *et al.*, submitted, Beavan and Haines, in preparation] show that the present day plate boundary is reaching as far south as the Porter Pass fault zone. Therefore, the absence of earthquakes near the Alpine fault in the northern study region could indicate a shift of the plate boundary

## a) Alpine Fault



## b) San Andreas Fault

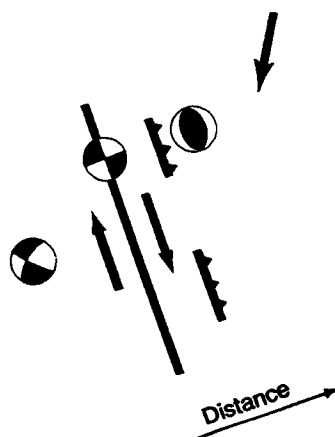


**Figure 3.19** a) Sketch map summarising the different tectonic regions in the study area. To the north is the transition zone to the Marlborough fault system. Earthquakes south of the Hope and the Porters Pass fault zone have a high thrust component and accommodate part of the dip-slip convergence of the plate motion. Distributed deformation is observed on NNW-SSE trending thrust faults east of the Alpine fault, by the strike-slip Godley River earthquake east of the Alpine fault and on thrust faults at the southwestern end of the Alpine fault. The Alpine fault accommodates both fault normal and fault parallel plate motion, with slightly higher normal convergence than expected by the plate motion [Beavan *et al.*, submitted]. b) Schematic overview of strain partitioning observed along the San Andreas fault in California. The strain is partitioned into dip slip motion on thrust faults and strike-slip motion on the San Andreas fault.

away from the Alpine fault to the Hope and Porters Pass fault zones. At both fault zones we observe strike-slip mechanisms along the trend of the fault zones and high crustal deformation in the adjacent crust with varied focal mechanisms which have a strong thrust component in fault normal direction.

Between Mt Cook and Haast, thrusting occurs on NNE trending faults or folds to a depth of up to 12 km. South of Haast, deformation is distributed between offshore and onshore regions (Figure 3.19a).

The stress field remains uniform throughout the study region, and therefore indicates that strain partitioning as observed at the San Andreas fault (Figure 19b, *Zoback et al.*, [1987]) is not present near the Alpine fault. The motion on the Alpine fault appears to absorb both dip-slip and strike-slip motion of the plate motion vector (Figure 19d), but most of this evidence comes from geologic [*Norris et al.*, 1990] and GPS observations. It remains uncertain if this will hold for large earthquake ruptures of the Alpine fault.

### 3.9 Acknowledgments

We thank the participants of the Southern Alps Passive Seismic Experiment and South Island Geophysical Transect. Special thanks to Tom McEvelly and Robert Uhrhammer for the organization of the SAPSE experiment. Mark Chadwick, Ken Gledhill, and Terry Webb provided data from the New Zealand Seismic Network and the Cass earthquake sequence. The manuscript benefited from discussions with Richard Norris, Peter Koons, Chris Pearson, Kelvin Berryman and John Beavan. Reviews from Martin Reyners, Russell Robinson, and Robert Yeats greatly improved this manuscript. Plots were created using GMT software [*Wessel and Smith*, 1995]. This research was supported by the New Zealand Foundation for Research Science and Technology. Institute of Geologic and Nuclear Sciences contribution ###.

### 3.10 References

- Abercombie, R.E., Near surface attenuation and site effects from comparison of surface and deep borehole recordings, *Bull. Seismol. Soc. Am.*, *87*, 731-744, 1997.
- Abercrombie, R.E., T.H. Webb, R. Robinson, P.J. McGinty, P.J. Mori, and J.R. Beavan, The enigma of the Arthur's Pass, New Zealand, earthquake 1: reconciling a variety of data for an unusual earthquake sequence, *J. Geophys. Res.*, submitted.
- Allis, R.G., and Y. Shi, New insights to temperature and pressure beneath the central Southern Alps, New Zealand, *N. Z. J. Geol. Geophys.*, *38*, 585-592, 1995.
- Anderson, H., T. Webb, and J. Jackson, Focal mechanisms of large earthquakes in the South Island of New Zealand; implications for the accommodation of Pacific-Australia plate motion, *Geophys. J. Int.*, *115* (3), 1032-1054, 1993.
- Anderson, H., and T. Webb, New Zealand seismicity, patterns revealed by the upgraded National Seismograph Network, *N. Z. J. Geol. Geophys.*, *37*, 477-493, 1994.
- Anderson, H., D.E. Phillips, T. McEvelly, F. Wu, and R. Uhrhammer, Southern Alps passive seismic experiment, Institute of Geological and Nuclear Sciences Report 97/21, 1997.
- Arnadottir, T., J. Beavan, and C. Pearson, Deformation associated with the 18 June 1994 Arthur's Pass earthquake, New Zealand, *N. Z. J. Geol. Geophys.*, *38*, 553-558, 1995.
- Bannister, S., D. Eberhart-Phillips, and B. Leitner, 3-D velocity structure, southern Alps region, from local earthquake and active-source SAPSE/Sight data, in *Geological Society of New Zealand and New Zealand Geophysical Society, Joint Annual Conference*, Geological Society of New Zealand, Christchurch, 1998.
- Batt, G., and J. Braun, The tectonic evolution of the Southern Alps, New Zealand; insights from fully thermally coupled dynamical modelling, *Geophys. J. Int.*, *136*, 403-420, 1999.

- Beavan, J., D. Darby, G. Blick, C. Pearson, T. Arnadottir, R.I. Walcott, B. Parsons, and P. England, GPS measurements at the transition between continental collision and subduction on the Pacific-Australian Plate boundary in New Zealand, in *EOS Trans. AGU*, 75(44), Fall Meet. Suppl., 669, 1994.
- Beavan, J., and J. Haines, Contemporary horizontal velocity and strain rate fields of the Pacific-Australian plate boundary zone through New Zealand, in prep.
- Beavan, J., M. Moore, C. Pearson, M. Henderson, B. Parson, S. Bourne, P. England, D. Walcott, G. Blick, D. Darby, and K. Hodgkinson, Crustal deformation during 1994-1998 due to oblique continental collision in the central Southern Alps, New Zealand, and implications for seismic potential of the Alpine fault, *J. Geophys. Res.*, submitted.
- Beavan, J., M. Moore, C. Pearson, M. Henderson, B. Pearsons, G. Blick, S. Bourne, P. England, D. Walcott, and K. Hodgkinson, 1994-1998 Crustal deformation due to oblique continental collision in the central southern Alps, New Zealand, and implications for seismic potential of the Alpine fault, in *Geological Society of New Zealand and New Zealand Geophysical Society, Joint Annual Conference*, pp. 260, Geological Society of New Zealand, Christchurch, 1998.
- Berryman, K.R., S. Beanland, A.F. Cooper, H.N. Cutten, R.J. Norris, and P.R. Wood, The Alpine Fault, New Zealand; variation in Quaternary structural style and geomorphic expression, in *Major active faults of the world; results of IGCP Project 206.*, edited by R.C. Buckman, and P.L. Hancock, pp. 126-163, Editrice Il Sedicesimo, Florence, Italy, 1992.
- Bourne, S.J., P.C. England, and B. Parson, The motion of crustal blocks driven by flow of the lower lithosphere and implications for slip rates of continental strike-slip faults, *Nature*, 391, 655-659, 1998.
- Braunmiller, J., J.L. Nabelek, B. Leitner, and A. Qamar, The 1993 Klamath Falls, Oregon, earthquakes sequence: source mechanisms from regional data, *Geophysical Research Letter*, 22, 105-108, 1995.
- Bull, W.B., and M.T. Brandon, Lichen dating of earthquake-generated regional rockfall events, Southern Alps, New Zealand, *Geol. Soc. Am. Bull.*, 110, 60-84, 1998.

- Carter, R.M., and L. Carter, The Motunau fault and other structures at the southern edge of the Australian Pacific plate boundary, offshore Marlborough, New Zealand, *Tectonophysics*, 88, 133-159, 1982.
- Cooper, A.F., and R.J. Norris, Estimates of the timing of the late coseismic displacement on the Alpine fault, northern Fiordland, New Zealand, *New Zealand Journal of Geophysics*, 33, 303-307, 1990.
- Cooper, A.F., and R.J. Norris, Anatomy, structural evolution, and slip rate of a plate-boundary thrust; the Alpine Fault at Gaunt Creek, Westland, New Zealand, *Geol. Soc. Am. Bull.*, 106 (5), 627-633, 1994.
- Cowan, H.A., A. Nicol, and P. Tonkin, A comparison of historical and paleoseismicity in a newly formed fault zone and a mature fault zone, North Canterbury, New Zealand, *J. Geophys. Res.*, 101, 6021-6036, 1996.
- Cox, S.C., and R.H. Findlay, The main divide fault zone and its role in formation of the Southern Alps, New Zealand, *N. Z. J. Geol. Geophys.*, 38, 489-499, 1995.
- Craw, D., Shallow-level metamorphic fluids in a high rate metamorphic belt; Alpine Schist, New Zealand, *J. Metam. Geol.*, 6, 1-16, 1988.
- Craw, D., M.S. Rattenbury, and R.D. Johnstone, Structure within Greenschist facies Alpine Schist, Central Southern Alps, *N. Z. J. Geol. Geophys.*, 37, 101-111, 1994.
- Crosson, R.S., Crustal structure modelling of earthquake data 1. Simultaneous least squares estimation of hypocentre and velocity parameters, *J. Geophys. Res.*, 81, 1191-1207, 1976.
- DeMets, C., Gordon, R.G., Argus, D.F., and S. Stein, The effect of recent revisions of the geomagnetic reversal time scale on estimates of current plate motions, *Geophys. Res. Lett.*, 21, 2191-2194, 1994.
- Doser, D.I., and T. Webb, Source parameters of large historic (1918-1962) earthquakes, South Island, New Zealand, *International J. Geophys. Res.*, submitted.

- Dreger, D.S., and D.V. Helmberger, Determination of source parameter at regional distances with three-component sparse network data, *Journal Geophysical Research*, 98, 8107-8125, 1993..
- Eberhart-Phillips, D., Examination of seismicity in the central Alpine Fault region, South Island, New Zealand, *N. Z. J. Geol. Geophys.*, 38, 571-578, 1995.
- Ellsworth, W.L., Three-dimensional structure of the crust and upper mantle beneath the island of Hawaii, PhD thesis, Massachusetts Institute of Technology, Massachusetts, 1977.
- Fan, G.W., and T.C. Wallace, The determination of source parameters for small earthquakes from a single, very broadband seismic station, *Geophys. Res. Lett.*, 18, 1385-1388, 1991.
- Funnell, R.H., and R.G. Allis, Heat flow variations in the South Island of New Zealand, submitted.
- Gledhill, K., R. Robinson, T. Webb, R. Abercombie, J. Beavan, J. Cousins, and D. Eberhart-Phillips, The Mw 6.2 Cass, New Zealand earthquake of 24 November, 1995: Reverse faulting in a strike-slip region, *N. Z. J. Geol. Geophys.*, submitted.
- Gledhill, K.R., and M. Chadwick, The EARSS digital seismograph: system description and field trials, *Bull. Seismol. Soc. Am.*, 81, 1380-1390, 1991.
- Haines, A.J., A local magnitude scale for New Zealand earthquakes, *Bull. Seismol. Soc. N. Z.*, 275-294, 1981.
- Haines, A.J., I.M. Cahaem, and D.E. Ware, *Crustal seismicity near Lake Pukaki, South Island*, 87-94 pp., 1979.
- Harris, R.A., S. Day, M. Steven, L. Yong-Gang, and V.J. E, Numerical simulations of an earthquake spontaneously propagating in fault gouge, *EOS, Trans. Am. Geophys. Union*, 75(44), Fall meeting Suppl., p 442, 1994.
- Herrmann, R.B., *Computer programs in seismology*, Saint Louis University, Saint Louis, 1991.

- Herzer, R.H., and J.D. Bradshaw, The Motunau fault and other structures at the southern edge of the Australian-Pacific plate boundary, offshore New Zealand. Discussion, *Tectonophysics*, 115, 161-164, 1985.
- Holbrook, W.S., D. Okaya, T. Stern, F. Davey, S. Henrys, and H. Van Avendonk, Deep seismic profiles across the Pacific-Australian plate boundary, South Island, New Zealand, *EOS, Trans. Am. Geophys. Un.* 79 (45), Fall meeting Suppl, 1998.
- Holm, D.K., R.J. Norris, and D. Craw, Brittle and ductile deformation in a zone of rapid uplift: central Southern Alps, New Zealand, *Tectonics*, 8, 153-168, 1989.
- Holt, W.E., and H.J. Haines, The kinematics of northern South Island, New Zealand, determined from geologic strain rates, *J. Geophys. Res.*, 100, 17991-18010, 1995.
- Hull, A.G., and K.R. Berryman, Holocene tectonism in the region of the Alpine Fault at Lake McKerrow, Fiordland, New Zealand, in *Recent crustal movements of the Pacific region.*, edited by W.I. Reilly, and B.E. Harford, pp. 317-331, The Royal Society of New Zealand, Wellington, New Zealand, 1986.
- Jenkins, G.R.T., D. Craw, and A.E. Fallick, Stable isotopic and fluid inclusion evidence for meteoric fluid penetration into an active mountain belt; Alpine Schist, New Zealand, *J. Metam. Geol.*, 12 (4), 429-444, 1994.
- Jones, L.M., Focal mechanisms and the state of stress on the San Andreas Fault in southern California, *J. Geophys. Res.*, 8869-8891, 1988.
- Julian, B.R., and G.R. Foulger, Earthquake mechanisms from linear-programming inversion of seismic-wave amplitude ratios, *Bull. Seismol. Soc. Am*, 86, 972-980, 1996.
- Kamp, P.J., and J.M. Tippet, Dynamics of Pacific Plate crust in the South Island (New Zealand) zone of oblique continent-continent convergence, *J. Geophys. Res.*, 98, 16105-16118, 1993.
- Kissling, E., W.L. Ellsworth, D.E. Phillips, and U. Kradolfer, Initial reference models in seismic tomography, *J. Geophys. Res.*, 99, 19635-19646, 1994.

- Kisslinger, C., Evaluation of S to P amplitude ratios for determining focal mechanisms from regional observations, *Bull. Seismol. Soc. Am.*, 70, 999-1014, 1980.
- Kleffman, S., F. Davey, A. Melhuish, D. Okaya, and T. Stern, Crustal structure in the central South Island from the Lake Pukaki seismic experiment, *N. Z. J. Geol. Geophys.*, 41, 39-49, 1998a.
- Kleffmann, S., T. Stern, S. Henrys, and S.w. group, Low seismic P-wave velocities at the plate boundary: implications for physical properties within the Alpine fault zone, in *Geological Society of New Zealand and New Zealand Geophysical Society Joint annual conference*, Geological Society, Christchurch, 1998b.
- Koons, P.O., Erosional controls on the mechanics of deforming wedges; an example from the Southern Alps, in *Geological Society of New Zealand annual conference; programme and abstracts.*, edited by R.E. Fordyce, pp. 69, Geological Society of New Zealand, Christchurch, New Zealand, 1987a.
- Koons, P.O., Some thermal and mechanical consequences of rapid uplift: an example from the Southern Alps, New Zealand, *Earth. Planet. Sci. Lett.*, 86, 307-319, 1987b.
- Koons, P.O., Two-sided orogen: Collision and erosion from the sandbox to the Southern Alps, New Zealand, *Geology*, 18, 679-682, 1990.
- Koons, P.O., Three-dimensional critical wedges: Tectonics and Topography in oblique collisional orogens, *J. Geophys. Res.*, 99, 12301-12315, 1994.
- Koons, P.O., R.J. Norris, A.F. Cooper, and D. Craw, Mechanic of a single structure accommodating oblique convergence; The development of the Alpine fault, in *New Zealand Geological Society and Geophysical Society of New Zealand joint annual conference*, Geological society of New Zealand, 1998.
- Krodolfer, U., Seismische Tomographie in der Schweiz mittels lokaler Erdbeben, Eidgenoessische Technische Hochschule, Zuerich, 1989.
- Lahr, J., Hypoellipse manual, 1992.

- Lamb, S., and H.M. Bibby, The last 25 Ma of rotational deformation in part of the New Zealand plate boundary, *J. Struct. Geol.*, *11*, 473-492, 1989.
- Michael, A.J., Stress rotation during the Coalinga aftershock sequence, *J. Geophys. Res.*, *92*, 7963-7979, 1987a.
- Michael, A.J., Use of focal mechanisms to determine stress: A control study, *J. Geophys. Res.*, *92*, 357-368, 1987b.
- Michael, A.J., Spatial variations in stress within the 1987 Whittier Narrows, California, Aftershock sequence: New technique and results, *J. Geophys. Res.*, *96*, 6303-6319, 1991.
- Michael, A.J., Determination of stress from slip data: faults and folds, *J. Geophys. Res.*, *89*, 11517-11526, 1984.
- Nabelek, J., and G. Xia, Moment tensor analysis using regional data: application to the 25 March, 1993, Scotts Mills, Oregon earthquake, *Geophys. Res. Lett.*, *22*, 13-16, 1995.
- Norris, R.J., and A.F. Cooper, Origin of small-scale segmentation and transpressional thrusting along the Alpine Fault, New Zealand, *Geol. Soc. Am. Bull.*, *107* (2), 231-240, 1995.
- Norris, R.J., and A.F. Cooper, Structure, Kinematics and Paleoseismicity of the central and southern sections of the Alpine fault, in *Geological Society of New Zealand and New Zealand Geophysical Society, Joint Annual conference*, pp. 260, Geological Society of New Zealand, Christchurch, 1998.
- Norris, R.J., P.O. Koons, and A.F. Cooper, The obliquely-convergent plate boundary in the South Island of New Zealand; implications for ancient collision zones, in *Australasian tectonics.*, edited by J.P. Platt, A.E. Grady, P.R. James, and A.J. Parker, pp. 715-725, Pergamon, Oxford-New York, International, 1990.
- Pearson, C.F., J. Beavan, D.J. Darby, G.H. Blick, and R.I. Walcott, Strain distribution across the Australian-Pacific plate boundary in the central South Island, New Zealand, from 1992 GPS and earlier terrestrial observations, *J. Geophys. Res.*, *100* (B11), 22071-22081, 1995.

- Rattenbury, M.S., Late low-angle thrusting and the Alpine Fault, central Westland, New Zealand, *N. Z. J. Geol. Geophys.*, 29, 437-446, 1986.
- Reyners, M., Subcrustal earthquakes in the central South Island, New Zealand, and the root of the Southern Alps, *Geology*, 15, 1168-1171, 1987.
- Reyners, M., Reservoir induced seismicity at Lake Pukaki, New Zealand, *Geophys. J. Int.*, 93, 127-135, 1988.
- Reyners, M., New Zealand seismicity 1964-87: an interpretation, *N. Z. J. Geol. Geophys.*, 32, 307-315, 1989.
- Reyners, M., and H. Cowan, The transition from subduction to continental collision: crustal structure in the North Canterbury region, New Zealand, *Geophys. J. Int.*, 115, 1124-1136, 1993.
- Reyners, M., C.E. Ingham, and B.G. Ferris, Microseismicity of the upper Clutha Valley, South Island, New Zealand, *N. Z. J. Geol. Geophys.*, 26 (1), 1-6, 1983.
- Reyners, M., and P. McGinty, Shallow subduction tectonics in the Raunakura Peninsula, New Zealand, as illuminated by earthquake focal mechanisms, *N. Z. J. Geol. Geophys.*, 1999.
- Reyners, M., R. Robinson, and P. McGinty, Plate coupling in the northern South Island and southernmost North Island, New Zealand, as illuminated by earthquake focal mechanisms, *J. Geophys. Res.*, 102, 15197-15210, 1997.
- Ritsema, J., and T. Lay, Rapid source mechanism determination of large ( $M_w > 5$ ) earthquakes in the western United States, *Geophys. Res. Lett.*, 20, 1611-1614, 1993.
- Robinson, R., and P. McGinty, The engima of the Arthur's Pass, New Zealand, earthquake 2: the aftershock distribution and its relation to the regional induced stress field, *J. Geophys. Res.*, submitted.
- Robinson, R., and T. Webb, "Amprat" and "Mechtool": programs for determining focal mechanism of local earthquakes, *Institute of Geological and Nuclear Science report*, 7, 1996.

- Robinson, R., M. Reyners, T. Webb, T. Anadottir, J. Beavan, J. Cousins, R.V. Dissen, and C. Pearson, The Mw 6.7 Arthur's Pass earthquake in the Southern Alps, New Zealand, June 18, 1994, *Seismol. Res. Lett.*, 66, 11-12, 1994.
- Roecker, S.W., Seismicity and tectonics of the Pamir-Hindu Kush region of central Asia, PhD thesis, Massachusetts Institute of Technology, Massachusetts, 1981.
- Rognavaldson, S., and R. Slunga, Routine fault plane solutions for local networks: a test with synthetic data, *Bull. Seismol. Soc. Am.*, 83, 1232-1247, 1993.
- Rynn, J.M.W., and C.H. Scholz, Seismotectonics of the Arthurs Pass region, South Island, New Zealand, *Geol. Soc. Am.*, 89, 1373-1388, 1978.
- Scholz, C.H., *The mechanics of earthquakes and faulting*, Cambridge University Press, Cambridge, 1990.
- Scholz, C.H., J.M.W. Rynn, R. Weed, and C. Frohlich, Detailed seismicity of the Alpine Fault Zone and Fiordland, South Island, New Zealand, in *Geophysics of the Earth and the Oceans, Part III.*, pp. 199-200, Elsevier, Amsterdam, Netherlands, 1974.
- Schwartz, S.Y., Source parameters of aftershocks of the 1991 Costa Rica and 1992 Cape Mendocino, California, earthquakes from inversion of local amplitude ratios and broadband waveforms, *Bull. Seismol. Soc. Am.*, 85, 1560-1575, 1995.
- Shi, Y., R. Allis, and F. Davey, Thermal Modeling of the Southern Alps New Zealand, *PAGEOPH*, 146, 469-501, 1996.
- Simpson, G.D.H., A.F. Cooper, and R.J. Norris, Quaternary-Holocene evolution of the Alpine fault zone at Paringa, South Westland, New Zealand, in *Geological Society of New Zealand 1993 annual conference; programme and abstracts.*, edited by P. Froggatt, pp. 134, Geological Society of New Zealand, Christchurch, New Zealand, 1993.
- Simpson, G.D.H., A.F. Cooper, and R.J. Norris, Late Quaternary evolution of the Alpine fault zone at Paringa, South Westland, New Zealand, *N. Z. J. Geol. Geophys.*, 37, 49-58, 1994.

- Smith, E.G.C., and F.J. Davey, Joint hypocentre determination of intermediate depth earthquakes in Fiordland, New Zealand, *Tectonophysics*, 104, 127-144, 1984.
- Snoke, J.A., J.W. Munsey, A.G. Teague, and G.A. Bollinger, A program for focal mechanism determination by combined use of polarity and SV-P amplitude ratio, *Earthquake Notes*, 55, 15, 1984.
- Stein, R.S., and R.S. Yeats, Hidden earthquakes, *Scientific America*, 6, 48-57, 1989.
- Stern, T.A., P.E. Wannamaker, D. Eberhart-Phillips, D. Okaya, F.J. Davey, and a.S.I.P.W. Group, Mountain Building and active deformation studied in New Zealand, *EOS*, 78, 329,335, 1997.
- Sutherland, R., and R.J. Norris, Late Quaternary displacement rate, paleoseismicity, and geomorphic evolution of the Alpine fault: evidence from Hokuri Creek, South Westland, New Zealand, *N. Z. J. Geol. Geophys.*, 38, 419-430, 1995.
- Tippett, J.M., and P.J.J. Kamp, Fission track analysis of the late Cenozoic vertical kinematics of continental Pacific crust, South Island, New Zealand, *J. Geophys. Res.*, 98, 16,119-16,148, 1993.
- Van Dissen, R., and R.S. Yeats, Hope Fault, Jordan Thrust, and uplift of the Seaward Kaikoura Range, New Zealand, *Geology*, 19 (4), 393-396, 1991.
- Walcott, R.I., Present tectonics and Late Cenozoic evolution of New Zealand, *Geophys. J. Roy. Astronom. Soc.*, 52, 137-164, 1978.
- Walcott, R.I., Modes of oblique compression: Late Cenozoic tectonics of the South Island of New Zealand, *Rev. Geophys.*, 36, 1-26, 1998.
- Wellman, H.W., An uplift map of the South Island of New Zealand, and a model for uplift of the Southern Alps, 13-20 pp., The Royal Society of New Zealand bulletin, 1979.
- Wessel, P., and W. H. F. Smith, New version of the generic mapping tools released, *Eos Trans. AGU*, 76, 329, 1995.

- Wolf, L.W., C.A. Rowe, and R.B. Horner, Periodic seismicity near Mt. Ogden on the Alaska-British Columbia border: A case for hydrologically triggered earthquakes?, *Bull. Seismol. Soc. Am.*, 87, 1473-1483, 1997.
- Wright, C., R.J. Norris, and A.F. Cooper, Paleoseismic history of the central Alpine fault, in *Geological Society of New Zealand and New Zealand Geophysical Society, Joint Annual conference*, pp. 260, Geological Society of New Zealand, Christchurch, 1998.
- Yeats, R., K. Sieh, and C. R. Allen, *Earthquake geology*, Oxford University press, p. 568, 1997.
- Yeats, R.S., Tectonic map of central Otago based on satellite imagery, *N. Z. J. Geol. Geophys.*, 30, 261-271, 1987.
- Yeats, R.S., and K.R. Berryman, South Island, New Zealand, and Transverse Ranges, California; a seismotectonic comparison, *Tectonics*, 6, 363-376, 1987.
- Yetton, M.D., and A. Wells, Paleoseismic history of the central and northern Alpine fault, in *Geological Society of New Zealand and New Zealand Geophysical Society, Joint Annual conference*, pp. 260, Geological Society of New Zealand, Christchurch, 1998.
- Zoback, M.D., M.L. Zoback, S. Van Mount, J. Suppe, J.P. Eaton, J.H. Healy, D. Oppenheimer, P. Reasenber, L. Jones, C.B. Raleigh, I.G. Wong, O. Scotti, and C. Wentworth, New evidence on the State of Stress of the San Andreas fault system, *Science*, 238, 1105-1111, 1987.

#### 4. Summary

Two case studies of Pacific plate boundary deformation are presented. Both studies utilise data that form part of a large-scale geophysical experiment. The interpretation is integrated with geophysical and geological observations of past and ongoing studies.

In the first study the crustal structure of the Vizcaino block is derived through hybrid modeling of gravity and seismic data. Bathymetry and reflection seismic data constrain the upper crust, whereas information from large aperture data constrain velocities in the lower crust. Gravity modeling provides a powerful tool, when constrained by all other methods, and is able to reveal the unusual Moho configuration in the northwestern Vizcaino block. Compression appears to have reactivated preexisting crustal faults, thickened the crust of the Oconostota ridge, and formed a kink in the Moho beneath the northwestern margin of the Vizcaino block. It also tilted and uplifted the Vizcaino block at its northern margin, forming the Gorda Escarpment and adjacent basement ridge. A similar steep Moho dip has been imaged in localised regions along the south and central paleoaccretionary margin in California. In this study, we see the Moho kink along strike and can deduce its origin. Relative plate motion changes applied to the Vizcaino block show 2 possible phases of compression. The main phase of compression was between 6-3.4 Ma, between the Pacific and Juan de Fuca plates; a second minor phase occurred between 18-12.5 Ma when the Vizcaino block was considerably younger and weaker than the adjoining Juan de Fuca plate. Deformation within the Vizcaino block appears to have ceased and shifted to the Gorda plate sometime prior to 3 Ma. We suggest that the spatial and temporal shifts of the primary locus of deformation resulted from changes in relative motions across the Pacific, Juan de Fuca/Gorda and North America plate boundaries combined with changes in lithospheric age and age contrast across these boundaries.

In the second study we utilize the regional background seismicity in the Alpine fault region, New Zealand, to study the seismotectonics at this continent/continent oblique collision zone. Seismicity is in general smaller than  $M_w$  4 and SAPSE's dense deployment is necessary to resolve both precise locations and focal mechanisms. We calculate precise locations for 195 earthquakes by simultaneous inversion for the hypocenter parameters, a 1-D velocity model, and station corrections. Focal mechanisms

are calculated with a first motion and amplitude ratio method. The technique is fully exploited, since both amplitude ratios and first motions are necessary to constrain the mechanisms. Both, evidence for seismic strain release along the Alpine fault and the low but comparable seismicity rate with locked sections of the San Andreas fault which ruptured in large earthquakes, suggest that we can expect large earthquakes on the Alpine fault.

Changes of the depth of the seismogenic zone, generally uniform at about 10-12 km, occur only at scales less than 30 km, suggesting that thermal perturbations must be of similar scale. This implies that the thermal effects of the uplift of the Southern Alps do not change the seismogenic depth significantly and are not in accordance with most of the present thermal models. The abrupt decrease of seismicity north of Bruce Bay and a triangular region of no seismicity between the intersections of the Hope and Porters Pass fault zone is interesting. It coincides with low velocity and high conductivity zones observed by transect data and 3-D seismic, suggested to be caused by high fluids and/or elevated temperatures. To correlate this anomalous region with high temperatures would be intuitive, but it is offset to the north of the region with highest uplift rates and consequently higher temperatures. The earthquakes in this study and a 3-D GPS survey [Beavan *et al.*, submitted, Beavan and Haines, in preparation] show that the present day plate boundary is reaching as far south as the Porter Pass fault zone. Therefore the absence of earthquakes near the northern part of the Alpine fault could indicate a shift of the plate boundary away from the Alpine fault to the Hope and Porters Pass fault zones. At both strike-slip fault zones we observe strike-slip earthquakes along the trend of the fault zones and high crustal deformation in the adjacent crust to the south with varied focal mechanisms which have a strong thrust component.

The seismic data reveal that most of the study region is affected by transitional tectonics to the subduction zones in the north and south. The region between Haast and Mt Cook, representative of the continent/continent collision zone, is dominated by NNE-SSW trending thrust and oblique strike slip mechanisms. Seismic strain is released at the Alpine fault itself and over a 60-100 km wide zone all along the plate boundary.

Both studies reflect a complicated pattern of plate boundary deformation. As we are capable of studying smaller and smaller scales of deformation with increasing accuracy,

we realize that our tectonic models are still oversimplified. Plate tectonics occurs on a truly broad scale, yet is affected by spatially and temporally small scale crustal changes as shown in both of our study regions.

## Bibliography

- Abercrombie, R.E., Near surface attenuation and site effects from comparison of surface and deep borehole recordings, *Bull. Seismol. Soc. Am.*, 87, 731-744, 1997.
- Abercrombie, R.E., T.H. Webb, R. Robinson, P.J. McGinty, P.J. Mori, and J.R. Beavan, The engima of the Arthur's Pass, New Zealand, earthquake 1: reconciling a variety of data for an unusual earthquake sequence, *J. Geophys. Res.*, submitted.
- Allis, R.G., and Y. Shi, New insights to temperature and pressure beneath the central Southern Alps, New Zealand, *N. Z. J. Geol. Geophys.*, 38, 585-592, 1995.
- Anderson, H., T. Webb, and J. Jackson, Focal mechanisms of large earthquakes in the South Island of New Zealand; implications for the accommodation of Pacific-Australia plate motion, *Geophys. J. Int.*, 115 (3), 1032-1054, 1993.
- Anderson, H., and T. Webb, New Zealand seismicity, patterns revealed by the upgraded National Seismograph Network, *N. Z. J. Geol. Geophys.*, 37, 477-493, 1994.
- Anderson, H., D.E. Phillips, T. McEvelly, F. Wu, and R. Uhrhammer, Southern Alps passive seismic experiment, Institute of Geological and Nuclear Sciences Report 97/21, 1997.
- Arnadottir, T., J. Beavan, and C. Pearson, Deformation associated with the 18 June 1994 Arthur's Pass earthquake, New Zealand, *N. Z. J. Geol. Geophys.*, 38, 553-558, 1995.
- Atwater, T., Implications of plate tectonics for the Cenozoic tectonic evolution of western North America, *Geol. Soc. Am. Bull.*, 81, 3513-3536, 1970.
- Atwater, T., Plate tectonic history of the northeast Pacific and western North America, in *The Geology of North America*, vol. N, *The Eastern Pacific Ocean and Hawaii*, edited by E. L. Winterer, D. M. Hussong, and R. W. Decker, pp. 21-72, Geol. Soc. of Am., Boulder, Colo., 1989.

- Atwater, T., and J. Severinghaus, Tectonic maps of the northeast Pacific, in *The Geology of North America*, vol. N, *The Eastern Pacific Ocean and Hawaii*, edited by E. L. Winterer, D. M. Hussong, and R. W. Decker, pp. 15-20, Geol. Soc. of Am., Boulder, Colo., 1989.
- Bannister, S., D. Eberhart-Phillips, and B. Leitner, 3-D velocity structure, southern Alps region, from local earthquake and active-source SAPSE/Sight data, in *Geological Society of New Zealand and New Zealand Geophysical Society, Joint Annual Conference*, Geological Society of New Zealand, Christchurch, 1998.
- Batt, G., and J. Braun, The tectonic evolution of the Southern Alps, New Zealand; insights from fully thermally coupled dynamical modelling, *Geophys. J. Int.*, 136, 403-420, 1999.
- Beavan, J., D. Darby, G. Blick, C. Pearson, T. Arnadóttir, R.I. Walcott, B. Parsons, and P. England, GPS measurements at the transition between continental collision and subduction on the Pacific-Australian Plate boundary in New Zealand, in *EOS Trans. AGU*, 75(44), Fall Meet. Suppl., 669, 1994.
- Beavan, J., and J. Haines, Contemporary horizontal velocity and strain rate fields of the Pacific-Australian plate boundary zone through New Zealand, in prep.
- Beavan, J., M. Moore, C. Pearson, M. Henderson, B. Parson, S. Bourne, P. England, D. Walcott, G. Blick, D. Darby, and K. Hodgkinson, Crustal deformation during 1994-1998 due to oblique continental collision in the central Southern Alps, New Zealand, and implications for seismic potential of the Alpine fault, *J. Geophys. Res.*, submitted.
- Beavan, J., M. Moore, C. Pearson, M. Henderson, B. Pearsons, G. Blick, S. Bourne, P. England, D. Walcott, and K. Hodgkinson, 1994-1998 Crustal deformation due to oblique continental collision in the central southern Alps, New Zealand, and implications for seismic potential of the Alpine fault, in *Geological Society of New Zealand and New Zealand Geophysical Society, Joint Annual Conference*, pp. 260, Geological Society of New Zealand, Christchurch, 1998.
- Berryman, K.R., S. Beanland, A.F. Cooper, H.N. Cutten, R.J. Norris, and P.R. Wood, The Alpine Fault, New Zealand; variation in Quaternary structural style and geomorphic expression, in *Major active faults of the world; results of IGCP Project 206.*, edited by R.C. Buckman, and P.L. Hancock, pp. 126-163, Editrice Il Sedicesimo, Florence, Italy, 1992.

- Blake, M. C., Jr., and D. L. Jones, The Franciscan assemblage and related rocks in northern California: A reinterpretation, *The Geotectonic Development of California*, edited by W. G. Ernst, pp. 307-328, Prentice-Hall, Englewood Cliffs, N.J., 1981.
- Bohannon, R. G., and T. Parsons, Tectonic implications of post-30 Ma Pacific and North American relative plate motions, *Geol. Soc. Am. Bull.*, 107, 937-959, 1995.
- Bonatti, E., Vertical tectonism in oceanic fracture zones, *Earth Planet. Sci. Lett.*, 37, 369-379, 1978.
- Bourne, S.J., P.C. England, and B. Parson, The motion of crustal blocks driven by flow of the lower lithosphere and implications for slip rates of continental strike-slip faults, *Nature*, 391, 655-659, 1998.
- Braunmiller, J., J.L. Nabelek, B. Leitner, and A. Qamar, The 1993 Klamath Falls, Oregon, earthquakes sequence: source mechanisms from regional data, *Geophysical Research Letter*, 22, 105-108, 1995.
- Braunmiller, J., B. Leitner, J. Nábelek, and A. M. Tréhu, Location and source parameters of the 19 June 1994 ( $M_w=5.0$ ) offshore Petrolia, California, earthquake, *Bull. Seismol. Soc. Am.*, 87, 272-276, 1997.
- Bull, W.B., and M.T. Brandon, Lichen dating of earthquake-generated regional rockfall events, Southern Alps, New Zealand, *Geol. Soc. Am. Bull.*, 110, 60-84, 1998.
- Carter, R.M., and L. Carter, The Motunau fault and other structures at the southern edge of the Australian Pacific plate boundary, offshore Marlborough, New Zealand, *Tectonophysics*, 88, 133-159, 1982.
- Castillo, D. A., and W. L. Ellsworth, Seismotectonics of the San Andreas fault system between Point Arena and Cape Mendocino in northern California: Implications for the development and evolution of a young transform, *J. Geophys. Res.*, 98, 6543-6560, 1993.
- Christensen, N. I., and W. D. Mooney, Seismic velocity structure and composition of the continental crust: A global view, *J. Geophys. Res.*, 100, 9761-9788, 1995.

- Christensen, N. I., and M. H. Salisbury, Structure and constitution of the lower oceanic crust, *Rev. Geophys.*, *13*, 57-86, 1975.
- Christeson, G. L., Y. Nakamura, K. D. McIntosh, and P. Stoffa, Effect of shot interval on ocean bottom seismograph and hydrophone data, *Geophys. Res. Lett.*, *23*, 3783-3786, 1996.
- Cooper, A.F., and R.J. Norris, Estimates of the timing of the late coseismic displacement on the Alpine fault, northern Fiordland, New Zealand, *New Zealand Journal of Geophysics*, *33*, 303-307, 1990.
- Cooper, A.F., and R.J. Norris, Anatomy, structural evolution, and slip rate of a plate-boundary thrust; the Alpine Fault at Gaunt Creek, Westland, New Zealand, *Geol. Soc. Am. Bull.*, *106* (5), 627-633, 1994.
- Cowan, H.A., A. Nicol, and P. Tonkin, A comparison of historical and paleoseismicity in a newly formed fault zone and a mature fault zone, North Canterbury, New Zealand, *J. Geophys. Res.*, *101*, 6021-6036, 1996.
- Cox, A., and D. Engebretson, Change in motion of Pacific plate at 5 Myr BP, *Nature*, *313*, 472-474, 1985.
- Cox, S.C., and R.H. Findlay, The main divide fault zone and its role in formation of the Southern Alps, New Zealand, *N. Z. J. Geol. Geophys.*, *38*, 489-499, 1995.
- Craw, D., Shallow-level metamorphic fluids in a high rate metamorphic belt; Alpine Schist, New Zealand, *J. Metam. Geol.*, *6*, 1-16, 1988.
- Craw, D., M.S. Rattenbury, and R.D. Johnstone, Structure within Greenschist facies Alpine Schist, Central Southern Alps, *N. Z. J. Geol. Geophys.*, *37*, 101-111, 1994.
- Crosson, R.S., Crustal structure modelling of earthquake data 1. Simultaneous least squares estimation of hypocentre and velocity parameters, *J. Geophys. Res.*, *81*, 1191-1207, 1976.

- DeMets, C., Gordon, R.G., Argus, D.F., and S. Stein, The effect of recent revisions of the geomagnetic reversal time scale on estimates of current plate motions, *Geophys. Res. Lett.*, 21, 2191-2194, 1994.
- Denlinger, R. P., A model for large-scale plastic yield of the Gorda deformation zone, *J. Geophys. Res.*, 97, 15415-15423, 1992.
- Dickinson, W. R., and W. S. Snyder, Geometry of triple junctions related to San Andreas transform, *J. Geophys. Res.*, 84, 561-572, 1979.
- Diebold, J., *R/V Ewing leg EW9412*, Lamont-Doherty Earth Obs., Columbia Univ., Palisades, N.Y., 1995.
- Doser, D.I., and T. Webb, Source parameters of large historic (1918-1962) earthquakes, South Island, New Zealand, *International J. Geophys. Res.*, submitted.
- Drake, D. E., D. A. Cacchione, J. V. Gardner, D. S. McCulloch and D. Masson, Morphology and growth history of Delgada fan: Implications for the Neogene evolution of Point Arena basin and the Mendocino triple junction, *J. Geophys. Res.*, 94, 3139-3158, 1989.
- Dreger, D.S., and D.V. Helmberger, Determination of source parameter at regional distances with three-component sparse network data, *Journal Geophysical Research*, 98, 8107-8125, 1993.
- Duncan, R. A., and D. A. Clague, Pacific plate motion recorded by linear volcanic chains, in *The Ocean Basins and Margins*, vol. 7A, edited by A. E. M. Nairn, F. G. Stehli, and S. Uyeda, pp. 89-121, New York, Plenum, 1985.
- Duncan, R. A., M. R. Fisk, A. G. Carey Jr., D. Lund, L. Douglas, D. S. Wilson, D. Krause, R. Stewart, and C. G. Fox, Origin and emergence of Mendocino Ridge (abstract), *Eos Trans. AGU*, 75 (44), Fall Meet. Suppl., 475, 1994.
- Eberhart-Phillips, D., Examination of seismicity in the central Alpine Fault region, South Island, New Zealand, *N. Z. J. Geol. Geophys.*, 38, 571-578, 1995.

- EEZ-SCAN 84 Scientific Staff, Atlas of the exclusive economic zone, western conterminous United States, *U.S. Geol. Surv. Misc. Invest., I-1792*, 152 pp., 1986.
- Ellsworth, W.L., Three-dimensional structure of the crust and upper mantle beneath the island of Hawaii, PhD thesis, Massachusetts Institute of Technology, Massachusetts, 1977.
- Engebretson, D. C., Cox, and R. G. Gordon, Relative motions between oceanic and continental plates in the Pacific Basin, *Geol. Soc. Am. Spec. Pap.*, 206, 59 pp., 1985.
- Fan, G.W., and T.C. Wallace, The determination of source parameters for small earthquakes from a single, very broadband seismic station, *Geophys. Res. Lett.*, 18, 1385-1388, 1991.
- Fernandez, L. S., and R. N. Hey, Late Tertiary tectonic evolution of the seafloor spreading system off the coast of California between the Mendocino and Murray fracture zones, *J. Geophys. Res.*, 96, 17955-17979, 1991.
- Fisk, M. R., R. A. Duncan, C. G. Fox, and J. B. Witter, Emergence and petrology of the Mendocino Ridge, *Mar. Geophys. Res.*, 15, 283-296, 1993.
- Flueh, E., M. Fisher, D. Scholl, T. Parsons, U. ten Brink, D. Klaeschen, N. Kukowski, A. Tréhu, J. Childs, J. Bialas, and N. Vidal, Scientific teams analyze earthquake hazards of the Cascadia subduction zone, *Eos Trans. AGU*, 78, 153-157, 1997.
- Fowler, C. M. R., *The solid earth*, An introduction to global geophysics, 472 pp., Cambridge University Press, 1990.
- Funnell, R.H., and R.G. Allis, Heat flow variations in the South Island of New Zealand, submitted.
- Gledhill, K., R. Robinson, T. Webb, R. Abercombie, J. Beavan, J. Cousins, and D. Eberhart-Phillips, The Mw 6.2 Cass, New Zealand earthquake of 24 November, 1995: Reverse faulting in a strike-slip region, *N. Z. J. Geol. Geophys.*, submitted.

- Gledhill, K.R., and M. Chadwick, The EARSS digital seismograph: system description and field trials, *Bull. Seismol. Soc. Am.*, 81, 1380-1390, 1991.
- Godfrey, N. J., Crustal structure of northern California, Ph.D. thesis, Stanford University press, Stanford, 177 pp., 1997.
- Godfrey, N. J., A. S. Meltzer, S. L. Klemperer, A. M. Tréhu, B. Leitner, S. H. Clarke Jr. and A. Ondrus, Evolution of the Gorda Escarpment, San Andreas fault, and Mendocino triple junction from multichannel seismic data collected across the northern Vizcaino block, offshore northern California, *J. Geophys. Res.*, 103, 23795-23812, 1998.
- Goldfinger, C., L. D. Kulm, R. S. Yeats, B. Appelgate, M. E. MacKay, and G. F. Moore, Transverse structural trends along the Oregon convergent margin; Implications for Cascadia earthquake potential and crustal rotations, *Geology*, 10, 141-144, 1992.
- Graham, S. A., and W. Dickinson, Evidence for 115 kilometers of right slip on the San Gregori-Hosgri fault trend, *Science*, 199, 179-181, 1978.
- Griscom, A., and R. C. Jachens, Tectonic history of the north portion of the San Andreas fault system, California, inferred from gravity and magnetic anomalies, *J. Geophys. Res.*, 94, 3089-3099, 1989.
- Haines, A.J., A local magnitude scale for New Zealand earthquakes, *Bull. Seismol. Soc. N. Z.*, 275-294, 1981.
- Haines, A.J., I.M. Cahaem, and D.E. Ware, *Crustal seismicity near Lake Pukaki, South Island*, 87-94 pp., 1979.
- Harbert, W., and A. Cox, Late Neogene motion of the Pacific plate, *J. Geophys. Res.*, 94, 3052-3064, 1989.
- Harris, R.A., S. Day, M. Steven, L. Yong-Gang, and V.J. E, Numerical simulations of an earthquake spontaneously propagating in fault gouge, *EOS, Trans. Am. Geophys. Union*, 75(44), Fall meeting Suppl., p 442, 1994.

- Henstock, T. J., A. Levander, and the Mendocino Working Group, Images of the Mendocino and San Andreas transforms in the Mendocino triple junction region: Continuous seismic profiling across the continental margin (abstract), *Eos Trans. AGU*, 77 (46), Fall Meet. Suppl., F741, 1996.
- Henstock, T. J., A. Levander, and J. A. Hole, Deformation in the lower crust of the San Andreas fault system in northern California, *Science*, 278, 650-653, 1997.
- Herrmann, R.B., *Computer programs in seismology*, Saint Louis University, Saint Louis, 1991.
- Herzer, R.H., and J.D. Bradshaw, The Motunau fault and other structures at the southern edge of the Australian-Pacific plate boundary, offshore New Zealand. Discussion, *Tectonophysics*, 115, 161-164, 1985.
- Holbrook, W. S., T. M. Brocher, U. S. ten Brink, and J. A. Hole, Crustal structure of a transform plate boundary: San Francisco Bay and the central California continental margin, *J. Geophys. Res.*, 101, 22311-22334, 1996.
- Holbrook, W.S., D. Okaya, T. Stern, F. Davey, S. Henrys, and H. Van Avendonk, Deep seismic profiles across the Pacific-Australian plate boundary, South Island, New Zealand, *EOS, Trans. Am. Geophys. Un.* 79 (45), Fall meeting Suppl, 1998.
- Holm, D.K., R.J. Norris, and D. Craw, Brittle and ductile deformation in a zone of rapid uplift: central Southern Alps, New Zealand, *Tectonics*, 8, 153-168, 1989.
- Holt, W.E., and H.J. Haines, The kinematics of northern South Island, New Zealand, determined from geologic strain rates, *J. Geophys. Res.*, 100, 17991-18010, 1995.
- Hoskins, E. G., and J. R. Griffiths, Hydrocarbon potential of northern and central California offshore, *Future Petroleum Provinces of the United States, Marine Geology and Potential*, edited by I. H. Cram, *AAPG Mem.*, 15, 212-228, 1971.
- Howie J. M., K. C. Miller, and W. U. Savage, Integrated crustal structure across the south central California margin: Santa Lucia escarpment to the San Andreas fault, *J. Geophys. Res.*, 98, 8173-8196, 1993.

- Hull, A.G., and K.R. Berryman, Holocene tectonism in the region of the Alpine Fault at Lake McKerrow, Fiordland, New Zealand, in *Recent crustal movements of the Pacific region.*, edited by W.I. Reilly, and B.E. Harford, pp. 317-331, The Royal Society of New Zealand, Wellington, New Zealand, 1986.
- Jachens, R. C., and A. Griscom, Geometry of the Gorda plate beneath northern California, *J. Geophys. Res.*, 88, 9375-9392, 1983.
- Jenkins, G.R.T., D. Craw, and A.E. Fallick, Stable isotopic and fluid inclusion evidence for meteoric fluid penetration into an active mountain belt; Alpine Schist, New Zealand, *J. Metam. Geol.*, 12 (4), 429-444, 1994.
- Jones, L.M., Focal mechanisms and the state of stress on the San Andreas Fault in southern California, *J. Geophys. Res.*, 8869-8891, 1988.
- Julian, B.R., and G.R. Foulger, Earthquake mechanisms from linear-programming inversion of seismic-wave amplitude ratios, *Bull. Seismol. Soc. Am.*, 86, 972-980, 1996.
- Kamp, P.J., and J.M. Tippet, Dynamics of Pacific Plate crust in the South Island (New Zealand) zone of oblique continent-continent convergence, *J. Geophys. Res.*, 98, 16105-16118, 1993.
- Kissling, E., W.L. Ellsworth, D.E. Phillips, and U. Kradolfer, Initial reference models in seismic tomography, *J. Geophys. Res.*, 99, 19635-19646, 1994.
- Kisslinger, C., Evaluation of S to P amplitude ratios for determining focal mechanisms from regional observations, *Bull. Seismol. Soc. Am.*, 70, 999-1014, 1980.
- Kleffman, S., F. Davey, A. Melhuish, D. Okaya, and T. Stern, Crustal structure in the central South Island from the Lake Pukaki seismic experiment, *N. Z. J. Geol. Geophys.*, 41, 39-49, 1998a.
- Kleffmann, S., T. Stern, S. Henrys, and S.w. group, Low seismic P-wave velocities at the plate boundary: implications for physical properties within the Alpine fault zone, in *Geological Society of New Zealand and New Zealand Geophysical Society Joint annual conference*, Geological Society, Christchurch, 1998b.

- Koons, P.O., Erosional controls on the mechanics of deforming wedges; an example from the Southern Alps, in *Geological Society of New Zealand annual conference; programme and abstracts.*, edited by R.E. Fordyce, pp. 69, Geological Society of New Zealand, Christchurch, New Zealand, 1987a.
- Koons, P.O., Some thermal and mechanical consequences of rapid uplift: an example from the Southern Alps, New Zealand, *Earth. Planet. Sci. Lett.*, 86, 307-319, 1987b.
- Koons, P.O., Two-sided orogen: Collision and erosion from the sandbox to the Southern Alps, New Zealand, *Geology*, 18, 679-682, 1990.
- Koons, P.O., Three-dimensional critical wedges: Tectonics and Topography in oblique collisional orogens, *J. Geophys. Res.*, 99, 12301-12315, 1994.
- Koons, P.O., R.J. Norris, A.F. Cooper, and D. Craw, Mechanic of a single structure accommodating oblique convergence; The development of the Alpine fault, in *New Zealand Geological Society and Geophysical Society of New Zealand joint annual conference*, Geological society of New Zealand, 1998.
- Krause, D. C., H. W. Menard, and S. M. Smith, Topography and lithology of the Mendocino Ridge, *J. Mar. Res.*, 22, 236-249, 1964.
- Krodolfer, U., Seismische Tomographie in der Schweiz mittels lokaler Erdbeben, Eidgenoessische Technische Hochschule, Zuerich, 1989.
- Kulm, L. V. D., R. von Huene, J. R. Duncan, J. C. J. Ingle, S. A. Kling, L. F. Musich, D. J. W. Piper, R. M. Pratt, H. Scradler, O. E. Weser, and S. W. J. Wise, Site 173, *Initial Rep. Deep Sea Drill. Proj.*, 18, 31-62, 1973.
- Lahr, J., Hypoellipse manual, 1992.
- Lamb, S., and H.M. Bibby, The last 25 Ma of rotational deformation in part of the New Zealand plate boundary, *J. Struct. Geol.*, 11, 473-492, 1989.
- Lendl, C., Finite difference wavefield modeling of large-aperture data from the 1993 Mendocino Triple Junction Seismic Experiment, master thesis, 163 pp., Oreg. State Univ., Corvallis, 1996.

- Lendl, C., A. M Tréhu, J. A. Goff, A. R. Levander, and B. C. Beaudoin. Synthetic seismograms through synthetic Franciscan: Insights into factors affecting large-aperture seismic data. *Geophys. Res. Lett.*, 24, 3317-3320, 1997.
- Lonsdale, P., Structural patterns of the Pacific floor offshore of Peninsular California, in *Gulf and Peninsular Provinces of the Californias*, edited by P. Dauphin, J. Ness and B. Simoneit, *AAPG Mem.*, 47, 87-125, 1991.
- Lyle, M., I. Koizumi, C. Richter, and the Shipboard Scientific Party, *Proceedings of the Ocean Drilling Program: Initial Reports, V. 167*, Ocean Drill. Program, College Station, Tex., 1997.
- Mattinson, J. M., Age, origin, and thermal histories of some plutonic rocks from the Salinian block of California, *Contrib. Mineral. Petrol.*, 67, 233-245, 1978.
- McCrary, P. A., D.S. Wilson, J.C. Ingle Jr., and R.G. Stanley, Neogene geohistory analysis of Santa Maria Basin, California, and its relationship to transfer of central California to the Pacific plate, *U.S. Geol. Surv. Bull.*, J, 1-38, 1995.
- McCulloch, D. S., The Vizcaino block south of the Mendocino triple junction, northern California, *Tectonics, Sedimentation and Evolution of the Eel River and Associated Basins of northern California, Proceedings of a Symposium*, edited by H. Schymiczek and R. Suchland, pp. 129-137, San Joaquin Geol. Soc. Misc. Publ., Bakersfield, Cal., 1987a.
- McCulloch, D. S., Regional geology and hydrocarbon potential of offshore central California, in *Geology and Resource Potential of the Continental Margin of Western North America and Adjacent Ocean Basins - Beaufort Sea to Baja California*, *Earth Sci. Ser.*, vol. 6, edited by D. W. Scholl, A. Grantz and J. G. Vedder, pp. 353-401, Circum-Pac. Counc. for Energy and Miner. Resour., Houston, Tex., 1987b.
- McCulloch, D. S., Evolution of the offshore central California margin, in *The Geology of North America*, vol. N, *The Eastern Pacific Ocean and Hawaii*, edited by E. L. Winterer, D. M. Hussong, and R. W. Decker, pp. 439-470, Geol. Soc. of Am., Boulder, Colo., 1989.
- McLaughlin R. J., S. A. Kling, R. Z. Poore, K. McDougall, and E. C. Beutner, Post-middle Miocene accretion of Franciscan rocks, northwestern California, *Geol. Soc. Am. Bull.*, 93, 595-605, 1982.

- McLaughlin, R. J., W.V. Sliter, N. O. Frederiksen, W. P. Harbert, and D. S. McCulloch, Plate motions recorded in Tectonostratigraphic terranes of the Franciscan complex and evolution of the Mendocino triple junction, northwestern California, *U.S. Geol. Surv. Bull.*, 1997, 60 pp., 1994.
- McLaughlin, R. J., W.V. Sliter, D.H. Sorg, P.C. Russell, and A.M. Sarna-Wojcicki, Large-scale right-slip displacement on the East San Francisco Bay region faults system, California: Implications for location of late Miocene to Pliocene Pacific plate boundary, *Tectonics*, 15, 1-18, 1996.
- Meltzer, A.S., and A. R. Levander, Deep crustal reflection profiling offshore southern central California margin, *J. Geophys. Res.*, 96, 6475-6491, 1991.
- Michael, A.J., Stress rotation during the Coalinga aftershock sequence, *J. Geophys. Res.*, 92, 7963-7979, 1987a.
- Michael, A.J., Use of focal mechanisms to determine stress: A control study, *J. Geophys. Res.*, 92, 357-368, 1987b.
- Michael, A.J., Spatial variations in stress within the 1987 Whittier Narrows, California, Aftershock sequence: New technique and results, *J. Geophys. Res.*, 96, 6303-6319, 1991.
- Michael, A.J., Determination of stress from slip data: faults and folds, *J. Geophys. Res.*, 89, 11517-11526, 1984.
- Miller, K.C., J. M. Howie, and S. D. Ruppert, Shortening within underplated oceanic crust beneath the central California margin, *J. Geophys. Res.*, 97, 19961-19980, 1992.
- Miller, K. C., M. Dober, F. Hua, and R. G. Bohannon, Crustal gravity models along seismic reflection profiles, California Continental Borderland (abstract), *Eos Trans. AGU*, 77 (46), Fall Meet. Suppl., F737, 1996.
- Nabelek, J., and G. Xia, Moment tensor analysis using regional data: application to the 25 March, 1993, Scotts Mills, Oregon earthquake, *Geophys. Res. Lett.*, 22, 13-16, 1995.

- Nafe, J. E., and C. L. Drake, Variation with depth in shallow and deep marine sediments of porosity, density and the velocities of compressional and shear waves, *Geophysics*, 22, 523-552, 1957.
- Nicholson, C., C. Sorlien, T. Atwater, J. Crowell, and B. Luyendyk, Microplate capture, rotation of the western Transverse Ranges, and initiation of the San Andreas transform as a low-angle fault system, *Geology*, 22, 491-495, 1994.
- Norris, R.J., and A.F. Cooper, Origin of small-scale segmentation and transpressional thrusting along the Alpine Fault, New Zealand, *Geol. Soc. Am. Bull.*, 107 (2), 231-240, 1995.
- Norris, R.J., and A.F. Cooper, Structure, Kinematics and Paleoseismicity of the central and southern sections of the Alpine fault, in *Geological Society of New Zealand and New Zealand Geophysical Society, Joint Annual conference*, pp. 260, Geological Society of New Zealand, Christchurch, 1998.
- Norris, R.J., P.O. Koons, and A.F. Cooper, The obliquely-convergent plate boundary in the South Island of New Zealand; implications for ancient collision zones, in *Australasian tectonics.*, edited by J.P. Platt, A.E. Grady, P.R. James, and A.J. Parker, pp. 715-725, Pergamon, Oxford-New York, International, 1990.
- Ondrus, A., Deformation of the Point Arena basin and the location of the San Andreas Fault Zone, offshore northern California, M.S. thesis, 46 pp., Lehigh Univ., Bethlehem, Pa., 1997.
- Parsons, T., A. M. Tréhu, J. H. Luetgert, F. Kilbride, K. Miller, R. E. Wells, M. A. Fisher, N. I. Christensen, U. S. ten Brink, E. Flueh, and W. D. Mooney, A new view into the Cascadia subduction zone and volcanic arc: Implications for earthquake hazards along the Washington margin, *Geology*, 26, 199-292, 1998.
- Pearson, C.F., J. Beavan, D.J. Darby, G.H. Blick, and R.I. Walcott, Strain distribution across the Australian-Pacific plate boundary in the central South Island, New Zealand, from 1992 GPS and earlier terrestrial observations, *J. Geophys. Res.*, 100 (B11), 22071-22081, 1995.
- Pratson, L. F., and W. F. Haxby, What is the slope of the U. S. continental slope?, *Geology*, 24, 3-6, 1996.

- Rattenbury, M.S., Late low-angle thrusting and the Alpine Fault, central Westland, New Zealand, *N. Z. J. Geol. Geophys.*, 29, 437-446, 1986.
- Reyners, M., Subcrustal earthquakes in the central South Island, New Zealand, and the root of the Southern Alps, *Geology*, 15, 1168-1171, 1987.
- Reyners, M., Reservoir induced seismicity at Lake Pukaki, New Zealand, *Geophys. J. Int.*, 93, 127-135, 1988.
- Reyners, M., New Zealand seismicity 1964-87: an interpretation, *N. Z. J. Geol. Geophys.*, 32, 307-315, 1989.
- Reyners, M., and H. Cowan, The transition from subduction to continental collision: crustal structure in the North Canterbury region, New Zealand, *Geophys. J. Int.*, 115, 1124-1136, 1993.
- Reyners, M., C.E. Ingham, and B.G. Ferris, Microseismicity of the upper Clutha Valley, South Island, New Zealand, *N. Z. J. Geol. Geophys.*, 26 (1), 1-6, 1983.
- Reyners, M., and P. McGinty, Shallow subduction tectonics in the Raunakura Peninsula, New Zealand, as illuminated by earthquake focal mechanisms, *N. Z. J. Geol. Geophys.*, 1999.
- Reyners, M., R. Robinson, and P. McGinty, Plate coupling in the northern South Island and southernmost North Island, New Zealand, as illuminated by earthquake focal mechanisms, *J. Geophys. Res.*, 102, 15197-15210, 1997.
- Riddihough, R. P., Gorda plate motions from magnetic anomaly analysis, *Earth Planet. Sci. Lett.*, 51, 163-170, 1980.
- Riddihough, R. P., Recent movements of the Juan de Fuca plate system, *J. Geophys. Res.*, 89, 6980-6994, 1984.
- Ritsema, J., and T. Lay, Rapid source mechanism determination of large ( $M_w > 5$ ) earthquakes in the western United States, *Geophys. Res. Lett.*, 20, 1611-1614, 1993.

- Robinson, R., and P. McGinty, The engima of the Arthur's Pass, New Zealand, earthquake 2: the aftershock distribution and its relation to the regional induced stress field, *J. Geophys. Res.*, submitted.
- Robinson, R., and T. Webb, "Amprat" and "Mechtool": programs for determining focal mechanism of local earthquakes, *Institute of Geological and Nuclear Science report*, 7, 1996.
- Robinson, R., M. Reyners, T. Webb, T. Anadottir, J. Beavan, J. Cousins, R.V. Dissen, and C. Pearson, The Mw 6.7 Arthur's Pass earthquake in the Southern Alps, New Zealand, June 18, 1994, *Seismol. Res. Lett.*, 66, 11-12, 1994.
- Rodrigues, D. and P. Mora, Analysis of a finite difference solution to the three-dimensional elastic wave equation, paper presented at 67nd. Annual International Meeting, Soc. for Explor. Geophys., 1992
- Roecker, S.W., Seismicity and tectonics of the Pamir-Hindu Kush region of central Asia, PhD thesis, Massachusetts Institute of Technology, Massachusetts, 1981.
- Rognvaldson, S., and R. Slunga, Routine fault plane solutions for local networks: a test with synthetic data, *Bull. Seismol. Soc. Am.*, 83, 1232-1247, 1993.
- Rynn, J.M.W., and C.H. Scholz, Seismotectonics of the Arthurs Pass region, South Island, New Zealand, *Geol. Soc. Am.*, 89, 1373-1388, 1978.
- Sandwell, D. T., and W. H. F. Smith, Marine gravity anomaly from Geosat and ERS 1 satellite altimetry, *J. Geophys. Res.*, 102, 10039-10054, 1997.
- Scholz, C.H., *The mechanics of earthquakes and faulting*, Cambridge University Press, Cambridge, 1990.
- Scholz, C.H., J.M.W. Rynn, R. Weed, and C. Frohlich, Detailed seismicity of the Alpine Fault Zone and Fiordland, South Island, New Zealand, in *Geophysics of the Earth and the Oceans, Part III.*, pp. 199-200, Elsevier, Amsterdam, Netherlands, 1974.

- Schwartz, S.Y., Source parameters of aftershocks of the 1991 Costa Rica and 1992 Cape Mendocino, California, earthquakes from inversion of local amplitude ratios and broadband waveforms, *Bull. Seismol. Soc. Am.*, 85, 1560-1575, 1995.
- Sedlock, R. L., and D. H. Hamilton, Late Cenozoic tectonic evolution of southwestern California, *J. Geophys. Res.*, 96, 2325-2351, 1991.
- Severinghaus, J., and T. Atwater, Cenozoic geometry and thermal state of the subducting slabs beneath western North America, in B. P. Wernicke, *Basin and Range Extensional Tectonics Near the Latitude of Las Vegas, Nevada*, edited by Geol. Soc. of Am. Mem., 176, 1-22, 1990.
- Shi, Y., R. Allis, and F. Davey, Thermal Modeling of the Southern Alps New Zealand, *PAGEOPH*, 146, 469-501, 1996.
- Silver, E. A., Tectonics of the Mendocino triple junction, *Geol. Soc. Am. Bull.*, 82, 2965-2978, 1971.
- Simpson, G.D.H., A.F. Cooper, and R.J. Norris, Quaternary-Holocene evolution of the Alpine fault zone at Paringa, South Westland, New Zealand, in *Geological Society of New Zealand 1993 annual conference; programme and abstracts.*, edited by P. Froggatt, pp. 134, Geological Society of New Zealand, Christchurch, New Zealand, 1993.
- Simpson, G.D.H., A.F. Cooper, and R.J. Norris, Late Quaternary evolution of the Alpine fault zone at Paringa, South Westland, New Zealand, *N. Z. J. Geol. Geophys.*, 37, 49-58, 1994.
- Smith, E.G.C., and F.J. Davey, Joint hypocentre determination of intermediate depth earthquakes in Fiordland, New Zealand, *Tectonophysics*, 104, 127-144, 1984.
- Smith, S. W., J. S. Knapp, and R. C. McPherson, Seismicity of the Gorda plate, structure of the continental margin, and an eastward jump of the Mendocino triple junction, *J. Geophys. Res.*, 98, 8153-8171, 1993.
- Snoke, J.A., J.W. Munsey, A.G. Teague, and G.A. Bollinger, A program for focal mechanism determination by combined use of polarity and SV-P amplitude ratio, *Earthquake Notes*, 55, 15, 1984.

- Stein, R.S., and R.S. Yeats, Hidden earthquakes, *Scientific America*, 6, 48-57, 1989.
- Stern, T.A., P.E. Wannamaker, D. Eberhart-Phillips, D. Okaya, F.J. Davey, and a.S.I.P.W. Group, Mountain Building and active deformation studied in New Zealand, *EOS*, 78, 329,335, 1997.
- Stewart, R., and L. Peselnick, Compressional velocities in dry Franciscan rocks to 8 kbar and 300°C, *J. Geophys. Res.*, 83, 2027-2039, 1977.
- Stoddard, P. R., A kinematic model for the evolution of the Gorda plate, *J. Geophys. Res.*, 92, 11524-11532, 1987.
- Sutherland, R., and R.J. Norris, Late Quaternary displacement rate, paleoseismicity, and geomorphic evolution of the Alpine fault: evidence from Hokuri Creek, South Westland, New Zealand, *N. Z. J. Geol. Geophys.*, 38, 419-430, 1995.
- Talwani, M., J. L. Worzel, and M. Landisman, Rapid gravity computations for two-dimensional bodies with application to the Mendocino submarine fracture zone, *J. Geophys. Res.*, 64, 49-59, 1959.
- Tippett, J.M., and P.J.J. Kamp, Fission track analysis of the late Cenozoic vertical kinematics of continental Pacific crust, South Island, New Zealand, *J. Geophys. Res.*, 98, 16,119-16,148, 1993.
- Tréhu, A. M., Tracing the subducted oceanic crust beneath the central California continental margin: Results from ocean bottom seismometers deployed during the 1986 Pacific Gas and Electric EDGE Experiment, *J. Geophys. Res.*, 96, 6493-6506, 1991.
- Tréhu, A. M., I. Asudeh, T. M. Brocher, J. H. Luetgert, W. D. Mooney, and J. L. Nábelek, Crustal architecture of the Cascadia forearc, *Science*, 266, 237-242, 1994.
- Tréhu, A. M., and the Mendocino Working Group, Pulling the rug out from under California: Seismic images of the Mendocino triple junction region, *Eos Trans. AGU*, 76, 369, 380-381, 1995.

- Van Dissen, R., and R.S. Yeats, Hope Fault, Jordan Thrust, and uplift of the Seaward Kaikoura Range, New Zealand, *Geology*, 19 (4), 393-396, 1991.
- Walcott, R.I., Present tectonics and Late Cenozoic evolution of New Zealand, *Geophys. J. Roy. Astronom. Soc.*, 52, 137-164, 1978.
- Walcott, R.I., Modes of oblique compression: Late Cenozoic tectonics of the South Island of New Zealand, *Rev. Geophys.*, 36, 1-26, 1998.
- Walter, A. W., and W. D. Mooney, Crustal structure of the Diablo and Gabilan Ranges, central California: A reinterpretation of existing data, *Bull. Seismol. Soc. Am.*, 72, 1567-1590, 1982.
- Wellman, H.W., An uplift map of the South Island of New Zealand, and a model for uplift of the Southern Alps, 13-20 pp., The Royal Society of New Zealand bulletin, 1979.
- Wessel, P., and W. H. F. Smith, New version of the generic mapping tools released, *Eos Trans. AGU*, 76, 329, 1995.
- Wilson, D. S., A kinematic model for the Gorda deformation zone as a diffuse southern boundary of the Juan de Fuca plate, *J. Geophys. Res.*, 91, 10259-10269, 1986.
- Wilson, D. S., Tectonic history of the Juan de Fuca ridge over the last 40 million years, *J. Geophys. Res.*, 93, 11863-11876, 1988.
- Wilson, D. S., Deformation of the so-called Gorda plate, *J. Geophys. Res.*, 94, 3065-3075, 1989.
- Wilson, D. S., Confidence intervals for motion and deformation of the Juan de Fuca plate, *J. Geophys. Res.*, 98, 16053-16071, 1993.
- Wilson, D. S., R. N. Hey, and C. Nishimura, Propagation as a mechanism of orientation of the Juan de Fuca Ridge, *J. Geophys. Res.*, 89, 9215-9225, 1984.
- Wilson, J. T., Static or mobile earth. The current scientific revolution. In Gondwanaland revisited: New evidence for continental drift. *Proc. Am. Phil. Soc.* 112, 309-320, 1968.

- Wolf, L.W., C.A. Rowe, and R.B. Horner, Periodic seismicity near Mt. Ogden on the Alaska-British Columbia border: A case for hydrologically triggered earthquakes?, *Bull. Seismol. Soc. Am.*, 87, 1473-1483, 1997.
- Wright, C., R.J. Norris, and A.F. Cooper, Paleoseismic history of the central Alpine fault, in *Geological Society of New Zealand and New Zealand Geophysical Society, Joint Annual conference*, pp. 260, Geological Society of New Zealand, Christchurch, 1998.
- Yeats, R., K. Sieh, and C. R. Allen, *Earthquake geology*, Oxford University press, p. 568, 1997. Yeats, R.S., Tectonic map of central Otago based on satellite imagery, *N. Z. J. Geol. Geophys.*, 30, 261-271, 1987.
- Yeats, R.S., and K.R. Berryman, South Island, New Zealand, and Transverse Ranges, California; a seismotectonic comparison, *Tectonics*, 6, 363-376, 1987.
- Yetton, M.D., and A. Wells, Paleoseismic history of the central and northern Alpine fault, in *Geological Society of New Zealand and New Zealand Geophysical Society, Joint Annual conference*, pp. 260, Geological Society of New Zealand, Christchurch, 1998.
- Zelt, C. A., and R. B. Smith, Seismic traveltime inversion for 2-D crustal velocity structure, *Geophys. J. Int.*, 108, 16-34, 1992
- Zoback, M.D., M.L. Zoback, S. Van Mount, J. Suppe, J.P. Eaton, J.H. Healy, D. Oppenheimer, P. Reasenber, L. Jones, C.B. Raleigh, I.G. Wong, O. Scotti, and C. Wentworth, New evidence on the State of Stress of the San Andreas fault system, *Science*, 238, 1105-1111, 1987.